Ozone in the Lower Atmosphere and its Contribution to High Ozone Concentrations at Ground-Level in the Southern San Joaquin Valley

Final Report

Contract No. 14-308

Prepared for the California Air Resources Board and the California Environmental Protection Agency

Dr. Ash Lashgari
Cal/EPA California Air Resources Board
Research Division
1001 I Street
5th Floor
Sacramento, CA 95814
(916) 323-1506

Principal Investigator
Ian Faloona
Department of Land, Air, and Water Resources
University of California Davis
One Shields Ave.
Davis, CA 95616-8521
Phone: (530) 752-2044
Fax: (530) 752-1552
E-mail: icfaloona@ucdavis.edu

Contributing Researchers
Daniella Caputi, UC Davis
Stephen Conley, UC Davis (now at Scientific Aviation, Inc.)
Justin Trousdell, UC Davis
Elizabeth Asher, UC Davis (now at NCAR)

May 1, 2015 – May 14, 2018

DISCLAIMER

The statements and conclusions in this Report are those of the contractor and not necessarily those of the California Air Resources Board. The mention of commercial products, their source, or their use in connection with material reported herein is not to be construed as actual or implied endorsement of such products.

ACKNOWLEDGEMENT

Because of the overlap of the majority of this project's field deployment with the California Baseline Ozone Transport Study sponsored by CARB, there were a lot of cross-fertilization benefits from that project. Specifically, we would like to thank the program managers Jin Xu, as well as Eileen McCauley, Ash Lashgari, and Leon Dolislager, for their assistance in coordinating and executing this project. Furthermore, the study benefitted tremendously from additional EPA funding in support of the CABOTS project. The funds from the EPA were channeled through the Bay Area Air Quality Management District via contract #2016-129, "Airborne Measurements of Horizontal Advection and Vertical Mixing during CABOTS." We thank Scott Bohning of the EPA and Saffet Tanrikulu of the BAAQMD for making this important component of the study possible.

This Report was submitted in fulfillment of ARB contract number 14-308, "Ozone in the Lower Atmosphere and its Contribution to High Ozone Concentrations at Ground-Level in the Southern San Joaquin Valley" by the University of California, Davis under the sponsorship of the California Air Resources Board. Work was completed as of May 2018.

CONTENTS

LIST OF FIGURES

LIST OF TABLES

ABSTRACT

We collected an unprecedented airborne data set by extensively sampling the lower 1500 m (~5,000 ft.) of the atmosphere in the Southern San Joaquin Valley (SSJV) in order to characterize conditions aloft to help improve the state's ability to model/predict surface ozone concentrations. Sampling occurred nearly all the way to the surface at four local airports and throughout the entire day/night cycle. Data were collected spanning five different, continuous 2-6 day periods during the summer when ozone air pollution is at its worst. The project utilized a well-instrumented scientific research aircraft operated by Scientific Aviation, Inc. to measure winds, temperature, humidity, ozone (O_3), nitric oxide (NO), nitrogen dioxide (NO_2), and methane (CH_4).

The experimental design further provided for an empirical estimation of the overnight vertical mixing strength between the layer aloft and the shallow nocturnal boundary layer. Similarly, midday entrainment rates of air aloft mixing into the valley boundary layer were quantified, which is a critical parameter in controlling ventilation of surface air in the valley. Regional emission rates of methane and NO_x were estimated to be substantially larger than current inventories suggest. Finally, the midday photochemical production rate of ozone was estimated and seen to correlate with day-to-day variations in the observed NO_x concentrations indicating that the southern San Joaquin Valley is predominantly NO_x-limited with respect to local ozone production. Preliminary analyses of these airborne and surface wind profiler data at Visalia indicate that overnight mixing is strongly influenced by the strength of the nocturnal jet (the up-valley wind associated with the so-called 'Fresno Eddy') and that a stronger jet results in more nighttime ozone loss at the surface, which impacts the following afternoon's peak ozone levels. Finally, the net chemical loss of ozone overnight from the production of nitrate is not well understood and further study of the fate of the nitrate radical is needed to better quantify this important loss in air quality models.

EXECUTIVE SUMMARY

Background

The San Joaquin Valley (SJV) has become the locus of one of the more vexing air quality challenges in the nation, and consequently is classified as an extreme ozone nonattainment area for the 8-hour ozone National Ambient Air Quality Standard (NAAQS.) One of the difficulties in fully understanding the causes of degraded air quality of the SJV is its long and deep geography, running approximately 400 km to the southeast (from Stockton to Arvin), spanning an average of nearly 100 km across, and bordered by a rim that rises to over 3 km on its northeastern flank (the Southern Sierra Nevada), ~1 km to its southwest (along the Diablo and Temblor Ranges of the Pacific Coast Range), and ~2 km at its terminus (in the San Emigdio and Tehachapi Mountains). Because of the topographic isolation of the SJV, air quality along the valley floor is strongly dependent, not only on local emissions, but also on the exact nature of the mixing aloft. Horizontal near surface airflow naturally feeds into the valley through gaps and cols in the Pacific Coast Range, predominately in the San Francisco Bay Area, and stagnates as it approaches the cul-de-sac of the Southern SJV (SSJV) at the Tehachapi Mountains. Improving air quality in the SSJV thus requires an accurate understanding of the meteorological conditions that influence the vertical mixing at the top of the atmospheric boundary layer (ABL) – the layer of air that is in rapid contact with the surface and typically extends to about 600 to 900 m (2,000 to 3,000 ft.) above the ground in the middle of a summer day in the SJV. Moreover, because this layer does not extend above the surrounding mountains, and is mixing with a partially polluted layer aloft, it is also important to understand the time scale of stagnation and recirculation of the air layer above the ABL. In general, surface ozone concentrations in the SSJV are dependent on three main factors: first, the horizontal transport of NO_x and VOC precursors (from upwind sources), second, the vertical mixing of pollutants between air above and within the boundary layer, and third, local in-situ chemical processes (e.g., photochemical production, titration, and dry deposition). The research outlined herein represents an experimental approach to quantitatively apportion ozone levels in the SJV to those various terms.

Objectives & Methods

This research contract generated an unprecedented airborne data set by extensively sampling the lower ~2.0 km of the atmosphere in the SSJV, all the way to the surface, throughout the diurnal cycle spanning five different 2-6 day periods during the summer ozone season in order to characterize the physical and chemical conditions that give rise to ozone non-attainment, with the aim of improving ARB's modeling of ozone concentrations in this challenging domain. By flying concerted sorties to the same area repeatedly, budgets are applied to the data set in order to precisely track the chemical evolution of ozone levels throughout the diurnal cycle. A total of 5 sorties were completed in the SSJV during which time high ozone concentrations (afternoon flight averages ranging from 69 – 91 ppbv) were observed in the region. These we define as Deployment 1: 10-12 September 2015, Deployment 2: 2-4 June 2016, Deployment 3: 28-29 June 2016, Deployment 4: 24-26 July 2016, and Deployment 5: 12-18 August 2016. By measuring the principal terms of the ozone budget equation (horizontal advection, entrainment mixing, and its temporal trend), estimates were made of both the photochemical production during the daytime and the vertical mixing at night, two processes that are not commonly observed, but are critical to

understanding the dynamics of ozone exceedance episodes. The measurement data and its analysis afforded by this project will thus enable a more comprehensive evaluation of model performance by investigating specific physical mechanisms that are critical to accurate SIP modeling and to developing more efficacious air quality regulatory strategies.

Results

Aside from providing a unique data set to CARB for modeling validation, the experimental design of the project provided for an explicit empirical estimation of several parameters central to the modeling of ozone episodes in the SSJV. First, the vertical mixing of ozone between the residual layer (RL) aloft and the shallow nocturnal boundary layer (NBL) during 12 overnight periods was quantified revealing eddy diffusivity values that ranged from 0.6 – 2.8 m^2/s. The eddy diffusivity parameter is used in air quality modeling to simulate vertical mixing and it is notoriously difficult to predict in the stable nocturnal boundary layer. Second, the midday entrainment of the lower atmosphere into the SJV atmospheric boundary layer was determined to occur at rates ranging from 1.1 – 8.0 cm/s. This entrainment mixing rate is a crucial parameter in all near surface air quality modeling because it usually has a diluting effect that works to keep pollutants from building up during the daytime. We find that in the SSJV the entrainment rates are heavily influenced by relatively small changes in the winds at the top of the ABL. Additionally, the airborne data allowed us to estimate regional average emission rates for methane and NO_x (360 ± 130 Gg CH_4 yr^{-1} and 190 ± 30 tons NO_x/day, respectively.) Such a result from the airborne data provides an opportunity to verify emissions inventories for regional SIP and Greenhouse Gas modeling. Furthermore, this project provides estimates of the midday photochemical production rate of ozone which ranged from 1.4 – 13.6 ppb/hr. The inferred rates were observed to correlate fairly well with in-situ NO_x concentrations (r^2 = 0.40) indicating that the southern San Joaquin Valley is predominantly NO_x–limited with respect to local ozone production. Confirming this photochemical condition has profound implications for strategies to achieve further ozone reduction in the SSJV. And finally, by interrogating runs of the Weather Research and Forecasting (WRF) model for the times of the flights we are able to calculate the residence time of the air above the boundary layer in the SSJV to be about one week. So the build-up of ozone in the residual layer occurs at that periodicity because it tends to stagnate for ~7 days in which time it can mix down the following day to jump start ozone production. The potency of the residual layer source, however, appears to be modified by the strength of the nocturnal jet, the prominent branch of the Fresno Eddy which was observed to vary in strength from 4 – 12 m/s on the midnight flights. Overnight mixing, fostered by the jet, brings residual layer ozone towards the surface where it is more susceptible to surface uptake, and in this manner the atmospheric dynamics have a direct impact on the next day's photochemistry.

Conclusions

The project succeeded in measuring the most important mixing rates of air in the Southern SJV that are vital to determining the periodic build-up and maintenance of ozone and its precursors in one of the most obdurate air quality air basins in the nation. The unique data set will provide ample opportunity to validate and improve ozone SIP modeling efforts across the entire diurnal ozone cycle in California's Central Valley. The work further puts forward a generalized three-layer atmospheric conceptual model to help frame the relative

importance of inflow and dilution, downward mixing to the surface at night, and regional photochemical production during the day. The data supports the fact that the Southern SJV O_3 is NO_x-limited, and that O_3 exceedance days may be ameliorated by the presence of a strong nocturnal jet.

INTRODUCTION

Air quality in the San Joaquin Valley (SJV) has become one of the most vexing air pollution challenges in the nation, and the region is classified as an extreme ozone nonattainment area for the 8-hour ozone NAAQS. One of the difficulties of fully understanding the causes of degraded air quality of the SJV its long and deep geography, running approximately 400 km (Stockton to Bakersfield) to the southeast, spanning an average of nearly 100 km across, and bordered by a rim that rises to over 3 km on its northeastern flank (the Southern Sierra Nevada), ~1 km to its southwest (the Diablo and Temblor Ranges), and ~2 km at its terminus (the San Emigdio and Tehachapi Mountains). Unlike other smaller basins, the precursor emissions that lead to elevated ozone concentrations come from several conurbations that are strung out along the primary surface inflow path from the San Francisco Bay Area through the Sacramento-San Joaquin Delta and then from Stockton down the valley axis to Bakersfield. Because of the topographic isolation of the SJV, air quality at its surface is strongly dependent on the exact nature of the mixing aloft, as the air that naturally feeds into it through gaps and cols in the Pacific Coast Range (predominately around the San Francisco Bay Area) eventually stagnates as it approaches the cul-de-sac of the Southern SJV (SSJV) at the Tehachapi Mountains. Accurate SIP modeling in the service of attaining air quality standards in the SSJV is therefore particularly sensitive to an accurate representation of the vertical mixing at the top of the valley boundary layer, its principal source of ventilation.

In general, surface ozone concentrations in the SSJV are dependent on three main factors:

1) horizontal transport of pollutants (from upwind sources along the low-level inflow path from the Sacramento-San Joaquin Delta),
2) vertical mixing of pollutants between air in the lower free troposphere (FT) and the atmospheric boundary layer (ABL), and
3) local in-situ chemical and physical processes (e.g., net photochemical production, titration, and dry deposition).

In upwind regions of the SJV (e.g., San Francisco Bay Area, Sacramento Valley) there are many sources of ozone precursors (VOCs and NO_x) and, under the condition of up-valley daytime wind flow (from the NNW toward the SSE) that is prevalent during summer days, these precursors generate ozone concentrations that typically increase as the air mass moves southward, often reaching its maximum in the southern end of the valley near Bakersfield [*Cox*, 2013]. However, the horizontal distribution of ozone is not always so straightforward and different 'background' meteorological conditions can distort this general pattern [*Jin et al.*, 2011].

Traditional atmospheric chemistry studies tend to focus on the third factor above, measuring as many different components of the oxidation chemical mechanism as possible, but are perennially hobbled by the first factor, horizontal advection, because it requires simultaneous measurements in many upwind locations to carefully constrain. Airborne

studies are uniquely suited to measure advection directly by flying up/downwind while observing the trace gas gradients and wind; however, most often they do not remain in one area long enough to make use of this capability. A past airborne study that did quantify this process in the SSJV showed that the average rate of afternoon ozone advection near Bakersfield (-2.0 ppb/h) was a leading term in the budget, as large as the observed increase, $\partial[O_3]/\partial t$, and the entrainment dilution rate [*Trousdell et al.*, 2016]. Entrainment, the second factor listed above, is another process that is difficult to monitor in traditional ground-based air pollution studies because it requires a knowledge of the gradients and dynamics at the top of the atmospheric boundary layer (ABL); yet this too can be estimated using judicious application of an airborne platform. One of the main objectives of this study was to deploy the aircraft measurements in such a way that the contributions of all three of the factors controlling ground level O_3 could be quantified. Knowing the absolute magnitudes of each of these terms in the ozone budget thereby opens up the possibility to more thoroughly investigate the fidelity of each process in air quality models.

Entrainment, the process whereby turbulent motions in the ABL incorporate air from above the capping inversion into the boundary layer, varies considerably over the course of the day. Because ABL turbulence over the continents is powerfully enhanced by solar heating of the surface entrainment tends to peak near midday. During the late afternoon and overnight periods radiative cooling of the surface generates a stably stratified layer, the nocturnal boundary layer (NBL), which decouples from the flow above leaving a residual layer (RL) stranded aloft that has the chemical makeup of the previous afternoon's ABL. However, within the Southern San Joaquin Valley a prominent low level jet is generated at the top of the stable NBL due to the frictional decoupling of the northwesterly (up-valley) wind from the surface late in the day with peak wind speeds of 5-20 m/s around midnight [*Bao et al.*, 2008; *Y L Lin and Jao*, 1995]. Several past observational studies have shown that such low level jets (LLJ) can have an important impact on ground level ozone levels during the night [*Salmond and McKendry*, 2002] and into the following day [*Aneja et al.*, 2000; *Hu et al.*, 2013; *Neu et al.*, 1994].

At night, because near surface ozone can be lost due to dry deposition and vertical mixing is quelled, the vertical gradient becomes large and positive. This sequestration of ozone aloft is plainly evident in the mean aircraft profiles from the 14 midnight flights shown in Figure 1. The layer between ~300 m (the average NBL height) and ~700 m (the average daytime ABL height) is the residual layer (RL) marked by elevated moisture (molar mixing ratio, per mil ≡ mmol H_2O (g)/mol air), ozone (O_3), and methane (CH_4, shown in Fig. 3) delivered there by vertical mixing from the day before. However, it is also apparent that there is a layer above the daytime ABL, up to about 2000 m, that is similarly influenced by surface emissions with enhanced water, methane, O_3, and NO_x. Such layers, that are some mix of both free tropospheric and boundary layer air, are sometimes referred to as "buffer layers" [*Russell et al.*, 1998] or "cloud layers" [*Augstein et al.*, 1974]. They are found most commonly over the oceans in the trade wind regime where intermittent cumulus convection lofts marine boundary layer air into a region that is moderately statically stable and only erratically turbulent below an elevated trade wind capping inversion. In the case of the SJV, the idea is similar but the lofting is caused by anabatic slope winds during the day up the valley's sidewalls and is redirected horizontally leading to recirculations below peak

height that lead to what may be called an "injection layer" in complex terrain [*Leukauf et al.*, 2016; *Reuten et al.*, 2007].

Then as the morning solar heating develops, rapid mixing down of ozone aloft in the RL gives rise to an abrupt increase observed at surface monitoring sites sometimes referred to as "fumigation" [*Stull*, 1988]. However, once the ABL grows to its usual midday height entrainment is assimilating air from the "buffer layer" (or "injection layer"), which itself is influenced by boundary layer air venting up the sidewalls. This differs appreciably from the usual conceptualization wherein ABL entrainment over flat terrain is diluted by free tropospheric air that is representative of the 'background' atmosphere. Because the buffer layer is laden with O_3 produced from previous days, entrainment dilution is significantly reduced and therefore does not slow the photochemical buildup in the ABL as effectively as in situations of flat terrain. This lofted reservoir is central to the air quality problems in the Central Valley, and thus greater study of its behavior (e.g., circulation patterns and flushing time) is warranted.

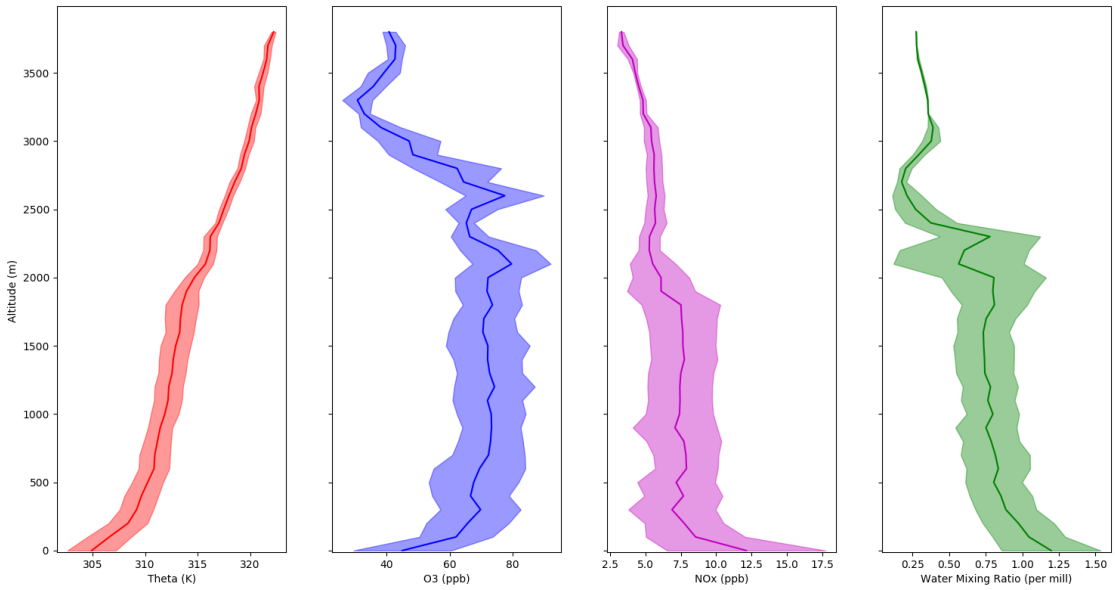

Figure 1. Mean vertical profiles measured during all 14 midnight flights between Fresno and Bakersfield. Colored patches represent +/- 1 standard deviation of all observations.

Figure 2 shows the average time derivative of ozone measured at five air quality monitoring stations spanning a transect from upwind at Fresno to downwind across Bakersfield, CA during June- September of 2012. These data indicate that the large burst of ozone that appears in the mid- morning during the rapid growth of the convective boundary layer up through the approximately neutrally stratified residual layer has made the majority of its contributions to surface ozone by about 09:00 Pacific Standard Time (PST). Two factors combine to promote a rapid increase in ground-level ozone during the morning hours. First, the reservoir of ozone in the RL that is sequestered overnight above the NBL, and thus away from dry deposition to the surface, gets mixed down after sunrise and rapidly increases ozone levels [*McKendry et al.*, 1997; *Neu et al.*, 1994]. Second, because radical production rates depend on the photolysis of O_3 and other oxidation products like HONO

(i.e., the non-linearity of ozone photochemistry), the mixing of fresh ozone and precursors from the sequestered layer can kick-start an even more rapid generation of ozone than simply from an additive initial condition. Thus the eventual afternoon maximum O_3 levels can be significantly influenced by the conditions established in the early morning by the character of the incorporated RL air, but separating these two factors is not simple due the non-linear chemistry. Nevertheless, some authors have attempted to empirically estimate the contribution of RL O_3 to the following day's peak and find it to be responsible for about half [*C-H Lin*, 2008; *Neu et al.*, 1994].

All four sites show the greatest rise in ozone occurring at 07:00 PST with a shoulder that typically extends out to about 09:00 or 10:00 PST. It is important to note that different sites experience very different rates of ozone injection from aloft. Part of this is due to the fact that some sites (e.g., Shafter & Bakersfield) have lower overnight O_3 lows (presumably due to greater NO titration). But this fact also points towards geographical variations in the contributions of O_3 aloft to daytime concentrations of O_3 at the surface.

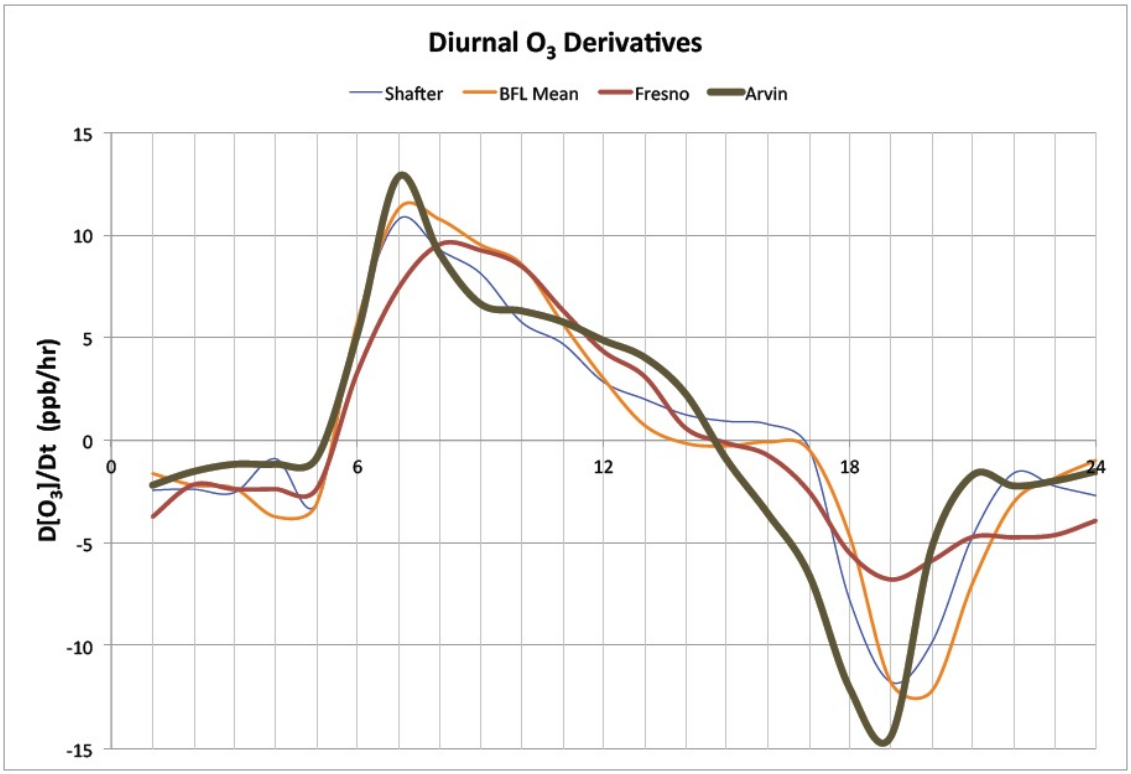

Figure 2. Average time derivative of surface ozone concentrations from June-September, 2012 from five sites in the CARB air quality monitoring network in the SSJV. 'BFL mean' is the average of California Ave. and Municipal Airport sites in Bakersfield.

While the importance of the morning RL down-mixing mechanism has been noted by many authors [*Aneja et al.*, 2000; *McKendry et al.*, 1997; *Morris et al.*, 2010; *Neu et al.*, 1994; *Zaveri et al.*, 2010], there is no straight-forward way to address it because the residual layer can be modified by differential advection, shear-induced turbulent mixing produced by low level nocturnal jets [*Hu et al.*, 2013; *Zaveri et al.*, 2010], and nitrate radical production [*Brown et al.*, 2003]. A recent study of residual layer O_3 in Houston

conducted using ozonesondes [*Morris et al.*, 2010] found a good relationship between yesterday afternoon's maximum O_3 levels and the peak in the residual layer, but the profiles were complex and the authors could not explain the strong variability in the residual layer aside from possible differential advection from a variety of hypothetical areas throughout the chemically variegated region. *Hu et al.* [2012] studied this problem in a field experiment in Maryland and concluded that models such as WRF-Chem required improved numerical algorithms to properly account for nocturnal vertical mixing.

The studies of Zhong et al. [2004], Bao et al. [2008], and Bianco et al. [2011] present evidence of a strong and persistent low level wind maximum (jet) in the southern San Joaquin Valley that appears to peak in the late evening (~23:00 PST). This was confirmed in all of our midnight flights, wherein we measured northwesterly wind peaks of between 4-12 m/s typically between 200-300 m above the valley floor. Figure 3 reproduces the average profile data from the 14 midnight flights from this project (similar to Figure 1), but here includes methane, wind speed, and an estimate of the turbulent kinetic energy (TKE) based on the observed variance in the horizontal winds. Such a pronounced nocturnal jet is likely to enhance horizontal advection (differentially with height, of course) as well as shear-induced vertical mixing. It is not a coincidence that the jet height is at the top of the NBL, because the latter is defined by interaction (trace gases and momentum) with the surface [*Blackadar*, 1957]. Our data indicate that there is a strong concentration of turbulent energy in the nocturnal boundary layer and it is probably forced by the low-level jet (LLJ). Further, we propose that variations in the LLJ's strength can influence the evolution of regional residual layer ozone. In a WRF study conducted by *Bao et al.* [2008] this low-level wind feature of the SSJV was over predicted by the model with a 2-3 m/s bias, and a 4 m/s root-mean-square error (see their Figure 10). Another unique strength of the data set generated by this research contract is the direct measurement of these nocturnal flows, which can be used to validate model processes that can be difficult to simulate *ab initio*.

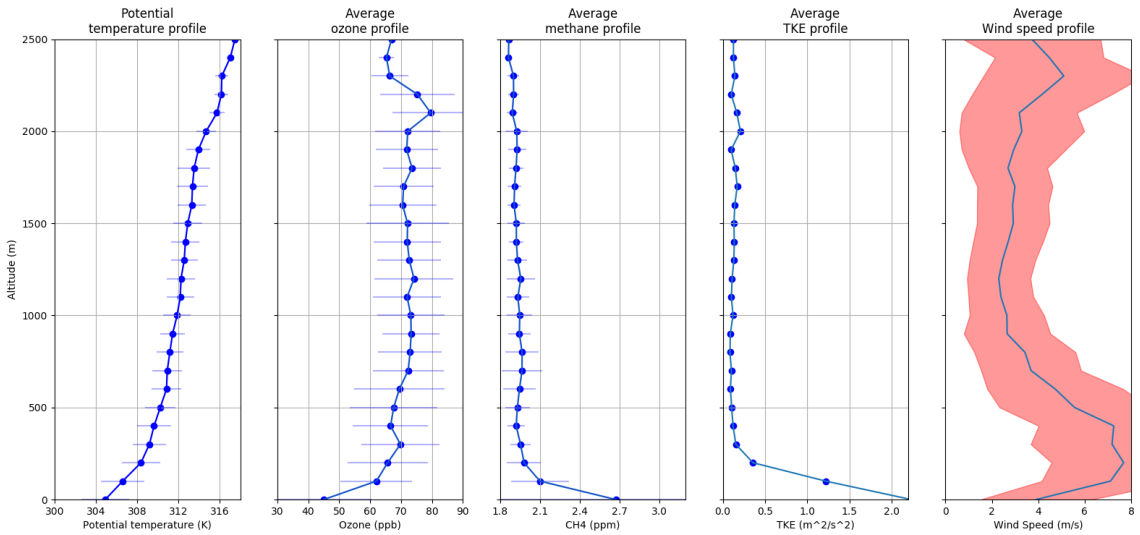

Figure 3. Average profiles from all 14 midnight flights (similar to Figure 1 but including methane, TKE, and wind speed.)

Identifying the advection of ozone within the residual layer over the SSJV region is a crucial component of this study and one that is very difficult to achieve without an airborne platform. Most previous studies of residual layer O_3, whether by tethersondes [*C-H Lin*, 2008; *Neu et al.*, 1994] or lidar [*Kuang et al.*, 2011; *Langford et al.*, 2012], have had to rely on back trajectories or mesoscale models to investigate the chemical origins and evolution of the RL. These methods are particularly dubious in the complex terrain of the Central Valley, and the advection process can be very significant in magnitude. By measuring the horizontal O_3 and NO_2 gradients and the in-situ winds, this data set can be used to directly quantify the importance of advection in determining the composition of the following morning's residual layer, and by so doing can provide powerful checks on the requisite accuracy of low level, nocturnal winds in air quality models.

Two concurrent projects that our group was executing under the aegis of the SJVAPCD and the EPA have direct bearing on the proposed work, and will serve as value-added support to the research. The first is a mountaintop monitoring of O_3 and NO_x at Chews Ridge during the duration of the CAlifornia Baseline Ozone Transport Study (CABOTS: https://www.esrl.noaa.gov/csd/projects/cabots/.) The second project was an extension of CABOTS made possible by the US EPA (in conjunction with the Bay Area Air Quality Management District) to more thoroughly probe the ozone budget during 6 additional afternoons upwind of Visalia where the NOAA group had deployed their aerosol and ozone lidar profiler in support of CABOTS. These data sets have been submitted to the CABOTS data archive, and some of their analysis may be presented in this report because they are so closely related to this project.

MATERIALS AND METHODS

Airborne Measurements

The airborne data was collected in partnership with Scientific Aviation, Inc. of Auburn, California. The Mooney Ovation was instrumented with a Picarro 2301F greenhouse gas analyzer (10 Hz measurements of $CH_4/CO_2/H_2O$), a 2B Technologies (model 205) ozone analyzer, an EcoPhysics NO chemiluminescence instrument with an Air Quality Design, Inc. photolytic converter to measure NO_x, temperature and relative humidity (Vaisala, HMP60), and a differential GPS wind detection system that was built in-house and is capable of measuring horizontal winds to within ~0.25 m/s in less than 1 minute [*Conley et al.*, 2014].

A total of 5 deployments were completed (10-12 September 2015, 2-4 June 2016, 28-29 June 2016, 24-26 July 2016, 12-18 August 2016). Each deployment consisted of stationing the airplane at Fresno Yosemite International Airport (KFAT). Profiles of the full boundary layer and above were taken at Fresno and Bakersfield. Along the Fresno-Bakersfield transect, altitude legs between 500, 1000, and 1500 m AGL were flown in a randomized order. Low passes were also flown over the Tulare (KTLR) airport, but in 2016 this was changed to the Visalia (KVIS) airport to coincide with the NOAA LIDAR deployment. A fourth profile to within 10 m of the ground was accomplished by a low pass over the airport at Delano, CA (KDLO). All of these airports are within a few hundred meters of California Highway 99, or in the case of Fresno and Bakersfield within urban centers. If time was remaining on any given flight, we typically utilized it by either completing an extra profile at Visalia, or flying west toward Hanson to better sample the nocturnal LLJ on the midnight flights. Overall, air traffic controllers were extremely cooperative in allowing us to complete the mission, and were flexible with any quick changes that were requested.

Table 1. A compilation of all flights flown for the Residual Layer O_3 (RLO) and CABOTS (EPA/BAAQMD) projects, with flight numbers and dates and approximate times for each.

Approximate	**Deployment 1 (RLO_1.txt)**						**Deployment 2 (RLO_2.txt)**						**Deployment 3 (RLO_3.txt)**					
Start Hour (PST)	9-Sep-15	10-Sep-15	11-Sep-15	12-Sep-15	13-Sep-15		2-Jun-16	3-Jun-16	4-Jun-16	5-Jun-16			28-Jun-16	29-Jun-16	30-Jun-16			
700		2	6	10	14		Transit	18	22	Transit				28	Transit			
1300		3	7	11			15	19	23				25	overheated				
1800	1	4	8	12			16	20	24				26	cabin door open in flight				
2300		5	9	13			17	21	alternator out				27					
Approximate	**Deployment 4 (RLO_4.txt)**				EPA/BAAQMD Flights		(EPA/BAAQMD Flights		**(EPA_ALL.txt) Deployment 5 (RLO_5.txt)**									
Start Hour (PST)	23-Jul-16	24-Jul-16	25-Jul-16	26-Jul-16	27/16-7/29/16		8/4/16-8/6/16		11-Aug-16	12-Aug-16	13-Aug-16	14-Aug-16	15-Aug-16	16-Aug-16	17-Aug-16	18-Aug-16		
700		30	34	38					42	43	47	49	53	57	61	65		
1300		31	35	39					Chews Ridge	44	48	50	54	58	62	66		
1800	29	32	36	40					profile	45	alternator	51	55	59	63	67		
2300		33	37	41						46	breaker prob	52	56	60	64			
	Misc_All.txt																	
	30-Jul-16	3-Aug-16	7-Aug-16															
	Post-EPA tran	Pre-EPA trans	Post-EPA transit															
Filename Convention:	**RLO_Deployment#.txt** ; **EPA_ALL.txt** for the EPA/BAAQMD daytime flights; **Misc_All.txt** for the extended transit flights.																	
Color Key:	**NOx Quality flags:**																	
Transit Flight	0	Highest confidence																
RLO Normal Flight	1	Lower confidence (moderate uncertainty)																
No Data Flight	2	Least confidence (discard data and consider missing)																
	3	Moderate uncertainty due to photolysis chamber interference																

The final dataset that has been provided to the ARB includes a numbering scheme for all of the flights, which is listed in Table 1.

Figure 4 illustrates the entire study region of the CABOTS project including the climatological winds at the surface flowing into the SJV (orange arrow) as well as the flow

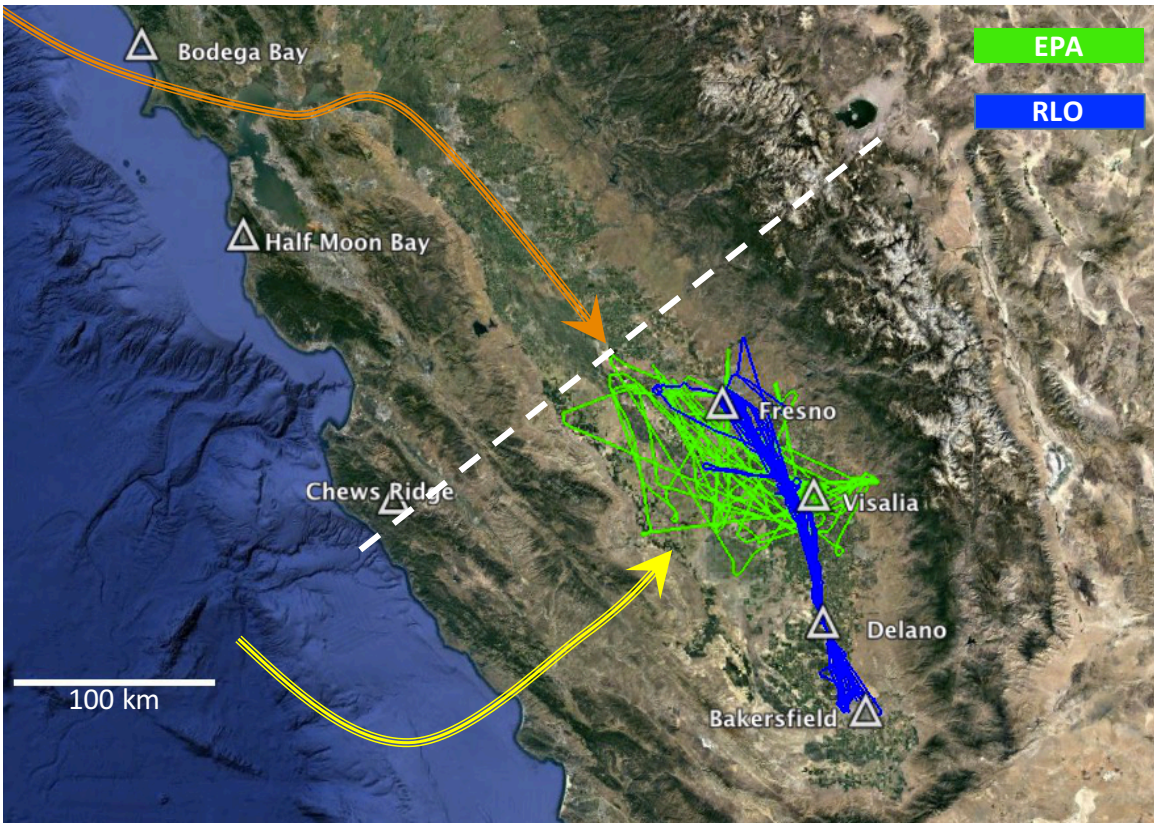

Figure 4. The average airflow into (near surface, orange arrow) and over (~700 hPa level, yellow arrow) the San Joaquin Valley of California. The white dashed line represents the diagonal path of the cross-section illustrated in Figure 18.

aloft at 700 hPa (yellow arrow) and the general flight area of the EPA flights between Fresno and Visalia, and RLO flights between the Fresno and Bakersfield airports.

Analysis of Historical Ozone Exceedances

Using 10 years of air quality data from the California Air Resources Board network (http://www.arb.ca.gov/adam/trends/trends1.php), we calculated the probability that the current 8-hour MDA standard (70 ppbv) would be exceeded in each week of the ozone season for four sites in the SSJV (Figure 5). This was used as a very crude first pass at forecasting the exceedance dates for flight scheduling. Although the probabilities seem to get higher farther south (smaller in Fresno – greater in Arvin), and rise steadily throughout the summer, there also seems to be a trimodal distribution with peaks in early May, mid-late June, and the beginning of September. At all sites there seems to be a lull in the ozone exceedances in early August, but this is especially prominent upwind of the southern end of the SJV (Fresno/Visalia.) *Pusede & Cohen* [2012] draw attention to the fact that temperature also seems to influence the reactive VOC emissions in the region and thus they found two different ozone production curves for high temperature vs. moderate temperature days. Nevertheless, their results indicate that the trend in ozone exceedance days, at least over the past dozen years or so, is due to a transition to NO_x–limited

photochemistry and ongoing NO_x reduction strategies in the Southern San Joaquin Valley, and our results discussed later corroborate their view.

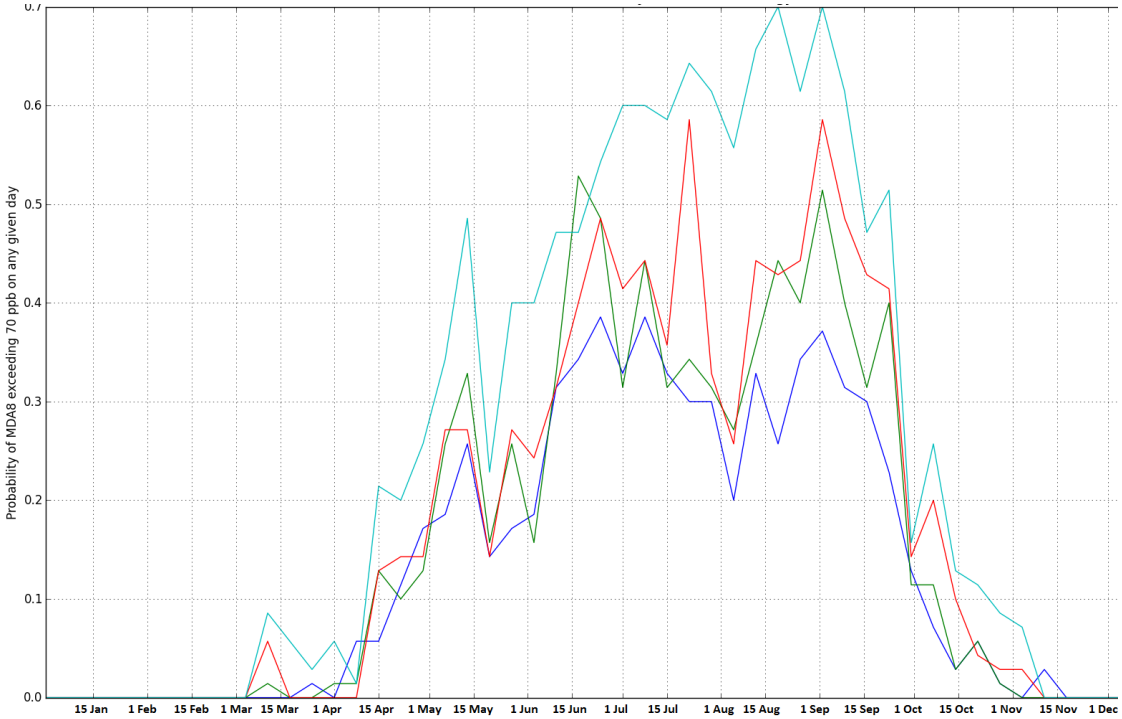

Figure 5. Probability of exceedance of the current (>70 ppb) MDA8 ozone standard for each week of the ozone season calculated from 10 years of surface data from four sites across the SSJV (blue - Fresno, green - Visalia, red - Bakersfield, cyan - Arvin.)

The second most direct forecast element in predicting O_3 exceedances was the forecast temperature. To get a sense of how good of a predictor this is we looked at the relationship between the daily maximum temperature and the MDA8 value for four continuous ozone seasons (2012-2015). Figure 6 shows that this meteorological variable explains

approximately 40% of the variance in the MDA8 ozone values in Fresno (r^2 value in Bakersfield was 0.29, not shown.)

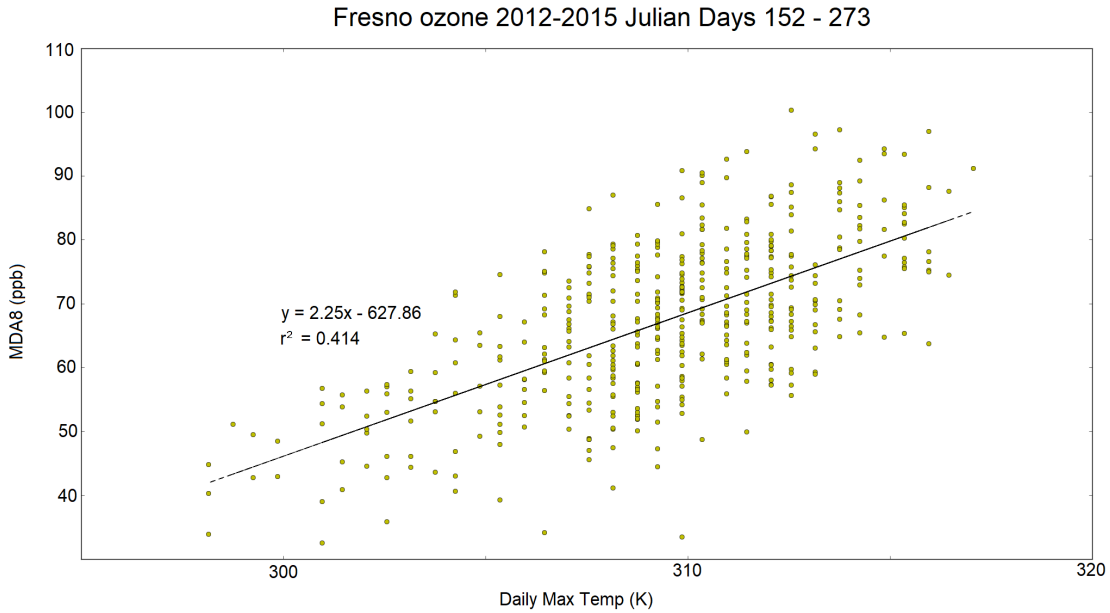

Figure 6. Correlation between max daily temperature and MDA8 ozone concentration in Fresno over four consecutive summers from 2012-2015.

Ozone Mass Balance

The chemical budget of ozone in the atmospheric boundary layer is affected primarily by four processes: dry deposition to the surface, (vertical) turbulent mixing, (horizontal) transport by the mean wind, and in-situ photochemical net production. Thus, in a very direct sense, the chemical reactivity *and* the dynamics of the atmosphere are similarly important in determining the daytime evolution of ozone concentrations. The details of the aircraft budgeting methodology can be found in previous work performed by our group on the NSF C-130 aircraft over the Pacific Ocean [*Conley et al.*, 2011; *Faloona et al.*, 2009], and with the Scientific Aviation Mooney in the SSJV [*Trousdell et al.*, 2016]. The mean budget equation for a vertically averaged scalar (S, in this case is the ozone concentration, but this applies just as well to NO_x or CH_4 or CO_2) in a turbulent medium can be described as in Equation 1.

$$\frac{\partial S}{\partial t} = \frac{\langle w's' \rangle_0 - \langle w's' \rangle_{z_i}}{z_i} - U\frac{\partial S}{\partial x} + P \qquad (1)$$

where S is the vertically averaged concentration throughout the ABL, $\langle w's' \rangle$ represents a turbulent flux at the surface, 0, or top, z_i, of the ABL, U is the mean wind (x aligned in the direction of the mean surface wind), and P is the net photochemical production of species S. In words, the afternoon ozone buildup can be attributed to four processes: 1) dry deposition to the surface, 2) mixing from above the boundary layer by turbulent motion, 3)

delivery from other parts of the valley by the wind, and 4) in-situ photochemical production. The most common parameterization used for the entrainment flux is to relate it to the product of the jump in a scalar across the inversion, ΔS, and the entrainment velocity, w_e (to be discussed in greater detail below): $\langle w's' \rangle_{z_i} = -w_e \Delta S$.

Remaining in the same airspace during the flight sorties provides an opportunity to directly measure the (Eulerian) time rate of change (left hand side), while flying upwind during the transects provides the advection term (2nd term on right hand side). Here we use a simple parameterization of the entrainment rate (or mixing across the top of the ABL), based on the measured jump in ozone across the ABL top, and a dry deposition velocity to estimate the two fluxes of the 1st term on the right-hand side. This permits solving for the net photochemical production of ozone (3rd term) during the afternoon in the study domain.

Boundary Layer Dynamics: Entrainment Velocity

One aspect of this work that partially relies on numerical modeling is estimating the entrainment velocity – that all important parameter which quantifies the turbulent mixing rate between the convective summertime boundary layer and the overlying layer. Because we cannot yet measure fluxes directly by eddy covariance in the Mooney aircraft, we have to resort to a budget of the boundary layer height in order to quantify the entrainment rate. Quite often the growth rate of the boundary layer is interpreted as equivalent to the entrainment velocity or volume flux of FT air into the ABL [*Stull*, 1988], assuming that there is no large scale mean vertical wind. However, in most situations the ABL growth ($\frac{dz_i}{dt}$) is actually determined by the difference of two distinct processes: the entrainment, which is considered to be driven by micrometeorological factors (viz. surface buoyancy flux, inversion strength, and possibly wind shear across the inversion), and the larger scale subsidence (W_{z_i}) working in the lower atmosphere just above the ABL typically forced by the large-scale, synoptic flow

$$w_e = \frac{dz_i}{dt} - W_{z_i} \tag{2}$$

To be even more precise, given that our sorties are within fixed regions (Eulerian in a sense) we expand the total derivative of the ABL height (z_i) into the Eulerian derivative and an advection term. The resultant z_i budget equation leads to a relationship between the entrainment velocity, the observed local ABL growth rate, the mean advection of ABL depth, and the mean vertical velocity at the inversion height:

$$w_e = \frac{\partial z_i}{\partial t} + U\frac{\partial z_i}{\partial x} - W_{z_i} \tag{3}$$

The first two terms on the right hand side of Equation 3 are, in principle, easily observed by aircraft, while the last term has evaded careful measurement by aircraft or any other means [*Angevine*, 1997; *Lenschow et al.*, 1999; *Lenschow et al.*, 2007]. In past work focusing on the region south of Bakersfield [*Trousdell et al.*, 2016] we estimated the large-scale vertical mean wind, *W*, using that derived from the NCEP/NARR pressure velocity

omega ($\omega = \frac{dp}{dt}$), and the surface pressure tendency neglecting horizontal pressure advection and assuming hydrostatic balance:

$$W = \frac{1}{\rho g} * \left(\omega - \frac{\partial p}{\partial t}\right) \quad (4)$$

The pressure level from which to select the omega value was chosen using the hypsometric equation $\left(p_2 = p_1 * \exp\left(-\frac{z_i * g}{R_d * \bar{T}}\right)\right)$ using an average observed ABL height, z_i, an average ABL temperature, $\bar{T}$, for the flight duration, R_d is the dry air gas constant, and an estimated average surface pressure, p_1, of 1010.5 mb for June-Sept. Because of the mesoscale variability across the SSJV, in this study we use the mean vertical velocities generated by WRF, which was run in forecast mode throughout the study period by Professor Shuhua Chen of UC Davis. It is this budgeting of the ABL height using Equation 3 that allows us to estimate the entrainment flux of any scalar and thereby solve for any term in Equation 1 that is not directly measured.

NO_x Budgeting

The form of the budget equation (Eq. 1) for ABL-averaged nitrogen oxides concentration, [NO_x], can be written as

$$\frac{\partial [NO_x]}{\partial t} = \frac{F_0 + w_e \Delta [NO_x]}{z_i} - \frac{[NO_x]}{\tau_{NOx}} - U \frac{\partial [NO_x]}{\partial x} \quad (5)$$

where the terms are (left to right): the observed time rate of change (sometimes referred to as 'storage'), net vertical mixing across the ABL boundaries (the difference between the surface flux, F_0, and the entrainment flux at z_i, the top of the ABL, which is parameterized as $-w_e \Delta [NO_x]$), photochemical loss (due to oxidation of NO_2 to nitric acid by OH, represented here as a chemical loss time scale, τ_{NOx}), and advection by the horizontal wind (the influence of the mean wind on the large scale horizontal gradient, here the *x*–direction is rotated such that there is no mean crosswind component).

The data used for the budgets of NO_x were collected between about 11:15 to 15:00 PST during six flights (27-29 July and 4-6 August, 2016) between Fresno and Visalia when the ABL was growing progressively after its initial rapid growth phase through the RL in the mid-morning. The flights were sponsored by the US EPA in an effort to aid the objectives of the California Baseline Ozone Transport Study (CABOTS) under the auspices of the California Air Resources Board (CARB). ABL growth is diagnosed by periodic vertical profiles of the aircraft's scalar measurements, i.e. water vapor, potential temperature, and methane, where a sharp transition in the scalar's magnitude is observed. Data within the growing ABL boundary layer is then selected from the total data set via a linear fit to the boundary layer heights in time, and all gradient terms from the equation above are assessed by a linear fit to this time-corrected data set. The average NO_x concentration and mean wind are averaged over the same domain within the ABL.

The oxidation rate of NO_x is considered to be controlled in the daytime by reaction with OH. A first order equivalent reaction rate was calculated from the Jet Propulsion Laboratory (JPL) Chemical Kinetics compendium [*Burkholder*, 2015], but only considered for the afternoon hours of each flight, with an average temperature and pressure measured from the flight data used to calculate the rate constant, k_{NO2+OH}. The median midday peak OH was observed in a different study to be approximately 6–8x10^6 molec cm^{-3} in the San Joaquin Valley [*Brune et al.*, 2016], with a flight time average of about 6 x10^6, which yields an average afternoon NO_x photochemical lifetime, τ_{NO_x}, of ~4.6 (±0.08) hours for the six flights. For a description of how the errors where generated for the budget terms refer to the error analysis section of *Trousdell et al.* [2016].

Due to the Soberanes wildfire that began on 22 July, 2016 some 200 km to the west of the study domain, occasionally the airborne measurements were subject to rapid spikes of NO_x (or an interfering species associated with the biomass burning plume). The wildfire effluent plumes were present mostly in the air above the boundary layer, but as the ABL grew in the afternoon these plumes would occasionally mix down into the ABL. This led to spikes occurring in the data set preferentially in the afternoon which biased our estimates of the temporal trend in NO_x. In four cases, simply removing the spikes from the ABL data set permitted a reasonable estimate, but on two flights we had to resort to using data from the CARB monitoring network (https://www.arb.ca.gov/adam/hourly/hourly1.php). The trend established was the average of three station trends (from 11:00-16:00 PST) throughout the region (Fresno-Garland, Visalia-N. Church St., and Hanford-S. Irwin St.). The estimates from the surface network and aircraft were very comparable for the other four flights in which both were measured (averages of -0.38 vs. -0.34 ppb/hr, respectively.) The photochemical lifetime of NO_x during midday (~5 hr) is much shorter than the advection time (~10 hr) of the fire plume even if the winds were blowing directly toward the study domain. Relative to the obvious impacts on CO and PM2.5, the surface network's NO_x measurements did not show signs of influence by the Soberanes fire (data not shown.) Nevertheless, even though there was likely some influence of the fire on the regional NO_x levels, the contribution entered the ABL through entrainment, which in principle is accounted for in the budgeting method by changes in the average jump across the ABL top ($\Delta[NO_x]$).

Chronological detail of project and accomplishments

Quarters 1-3

Due to some contracting delays the project was officially started on 15 May 2015 instead of January 1. Because of changes in specifications of the NO_2 instrument, it was necessary to use an EcoPhysics CLD 88 chemiluminescence NO detector with a photolytic converter (made by Air Quality Design, Inc.) for detection of NO_x. On 21 July 2015 an audit took place by ARB's Quality Assurance Section of the Monitoring and Laboratory Division using their mobile auditing system at the Lincoln regional hangar where Scientific Aviation keeps the aircraft. The ozone, NO, and temperature measurements successfully passed the audit, however due to complications with the photolytic converter, the NO_2 measurement was not correctly set up, and thus failed the audit. After making the appropriate changes to

the NO_x system, the mobile lab returned on 6 August 2015 and completed a successful audit of the NO_2 measurements. See the Appendix for a detailed account of the calibration history and data corrections used in finalizing the NO_x data set.

According to the US EPA (http://www.epa.gov/airdata), Kern County CA saw its lowest ever number of days in exceedance of the 8-hr O_3 NAAQS in 2015: just 36 in total (2005-2014 decadal average is 84). The absence of severe air quality episodes during July and August, 2015 prevented our first deployment from taking place until 10–12 September, 2015. The dates of the first deployment were finalized about 4 days in advance and were selected based on high confidence of a ridge setting up over the west coast, with forecasted high temperatures exceeding 38ºC for each day. Additionally, wind patterns at the 850 hPa level appeared to be favorable for air to stagnate and pool against the southernmost mountains of the valley. While temperatures were several degrees lower than forecast, high ozone was still present (decreasing from 90 to 80 to 70 ppbv across the three afternoons of the flight deployment.) A strong ridge was present over the west coast of the United States, causing the southern SJV to experience high temperatures around 35°C each day. Winds were light and resembled typical summer patterns. Excessive fire smoke was present north of 36N, especially on the afternoon of 12 September, so we present profiles averaged north and south of that latitude line to acknowledge the distinct air masses (see Figure 10). Afternoon ozone concentrations at the surface (as measured by the aircraft) averaged around 80 ppb with local maxima around 135 ppb. The highest ozone observed was on 10 September, 2015 around Fresno with mixed layer concentrations topping off at ~125 ppbv. This exceedance value was likely due to unexpected fire smoke. It was decided that future deployments would attempt to avoid this potentially confounding factor, however that proved impossible in 2016, and is likely to become a constant feature of the SJV air quality problems. A statistical feature that was revealed during pre-deployment analysis of past air quality data from Fresno was that the most likely times for ozone exceedances occur in the first and last weeks of July and September (Figure 5).

Deployment 1 (September 9-13) Profiles

Nocturnal Elevated Mixed Layer

One interesting feature noted in the pre-project data analysis was the presence of unstable layers overnight in the Visalia radio acoustic sounding system (RASS). Confirmed during the late evening flights of the first deployment, aircraft temperature profiles showed the presence of unstable layers of air at night around 500 m AGL, extending through about 100 meters in depth. These unstable layers were especially prominent near Bakersfield. Light turbulence was almost universally observed aboard the aircraft while flying through these layers, which suggests that they are actually present in the atmosphere as opposed to a measurement artifact.

As further evidence of this elevated mixed layer, climatological Bulk Richardson Numbers (BRN) for the month of September were computed from the Visalia 915 MHz sounder data. The BRN is a commonly used non-dimensional number that strives to estimate the relative strength of the competing forces of stable stratification in an atmospheric layer and wind shear across it which tries to generate turbulence mechanically. This data showed a

clear signal of relatively low BRNs in the early morning hours around 500 meters above ground level, with a depth of about 100 meters. It should be noted that there are some potential weaknesses with the methodology of computing BRN from sounder data, mainly that the potential errors for both temperature and wind are large, and since BRN depends on vertical gradients of both temperature and wind, there may be large errors in the calculations. Additionally, it should be noted that some researchers have suggested that BRN is not a good predictor for turbulence in very stable, nighttime conditions [*Mahrt*, 2010].

Ozone

For the most part, the ozone profiles were fairly consistent with conventional well-mixed boundary layer theory. For both the Bakersfield and Fresno areas, the boundary layer ozone concentrations peaked during the afternoon. One feature worth noting is that beginning on the afternoon of day two, 11-Sep-15, and continuing for the remainder of the mission, ozone was particularly enhanced near Fresno above 1300 meters MSL (by 20-40 ppbv over boundary layer concentrations.) These layers were observed on September 11, 2015 and the day before afternoon ground level concentrations reached 125 ppbv. These enhanced layers aloft are likely evidence of the storage of the previous day's ozone (probably enhanced by the fire smoke that was pervading the region) above the residual layer in the 'buffer layer' of the valley atmosphere.

NO_x

NO was found to be a fairly well-mixed species, with concentrations throughout the sampled profiles averaging between 0 and 2 ppbv. The sunrise profiles showed a maximum of NO in the lowest 100 meters, with peaks around 6 to 9 ppbv. One other interesting feature is a local maximum of NO noted near Fresno during the afternoon and sunset flights on 12-Sep-15, around 200 meters AGL. This is also perhaps linked with the fire smoke in the vicinity. NO_2 patterns revealed a similar pattern of mixing, with surface spikes occurring during sunrise flights. The surface spikes were around 30 to 50 ppb in magnitude. While NO_2 was fairly well-mixed with height otherwise during each flight, variations occurred throughout each day. NO_2 was highest in the morning and lowest at night, with similar amounts being measured during the afternoon and evening. The most overall NO_2 was observed on the sunrise flight of the first day, consistent with this day having experienced the greatest influence of fire smoke and consequent ozone production.

Visalia sounder comparison

During the first deployment, two attempts were made to collect data in order to compare winds measured by the Visalia wind profiler and the aircraft. To perform this analysis, flight winds and Visalia winds were averaged into 100m vertical bins. Both the flight and sounder winds were deconstructed into U and V components for ease of comparison. Some limitations are encountered with the sounder data averaging over a 1 hour period, and spending only about 20 minutes of flight time total in the vicinity of Visalia. On the late-night flight of 11-Sep-15, the overall shape of the wind profile (when broken into U and V components) of the flight data matched the shape of the wind profile from the sounder.

Both methods recorded a wind maximum around 300 meters AGL. However, the flight data indicated a greater magnitude of wind. This is perhaps due to the flight path being west of the sounder, and thus farther away from the mountains. On the afternoon flight of 12-Sep-15, a more thorough comparison was performed, with the flight path entering the traffic pattern of KVIS, where the sounder is situated (Figure 7). In this case, a better match between the sounder and flight data was observed. Below 600 meters AGL, both profiles indicated U and V component velocities within 1 m/s of each other. Above 600 meters, some small discrepancies arise, namely, the winds from the flight appear to be somewhat lower than measured from the sounder. This could possibly be due to larger errors from sounder data at higher altitudes.

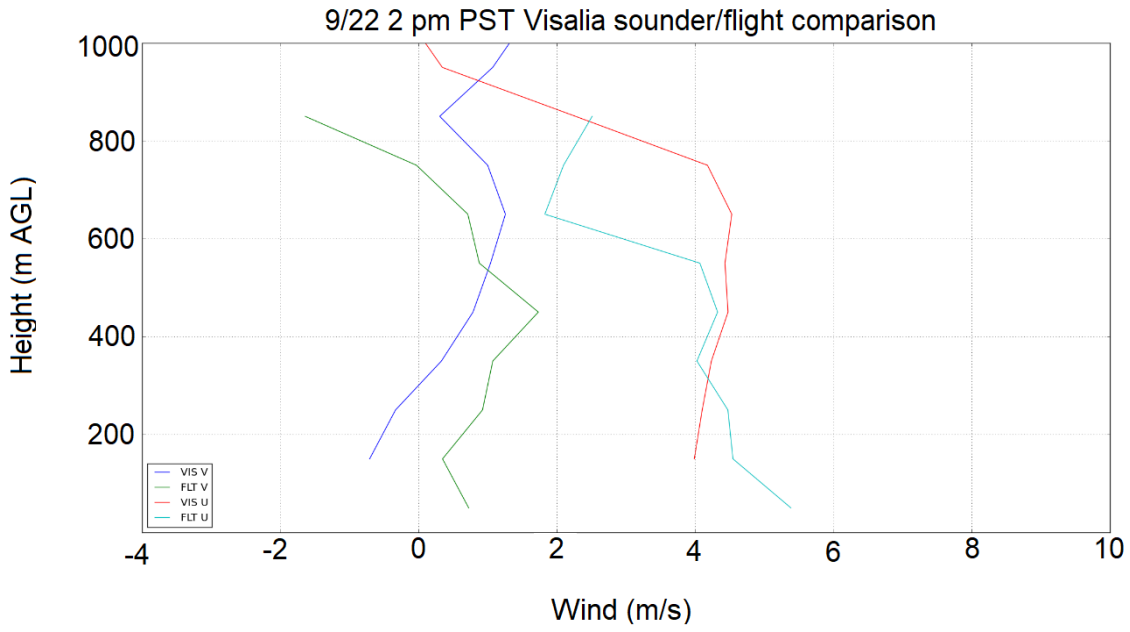

Figure 7. Wind comparison from 12-Sep-2015 between aircraft (FLT) and the Visalia sounder (VIS).

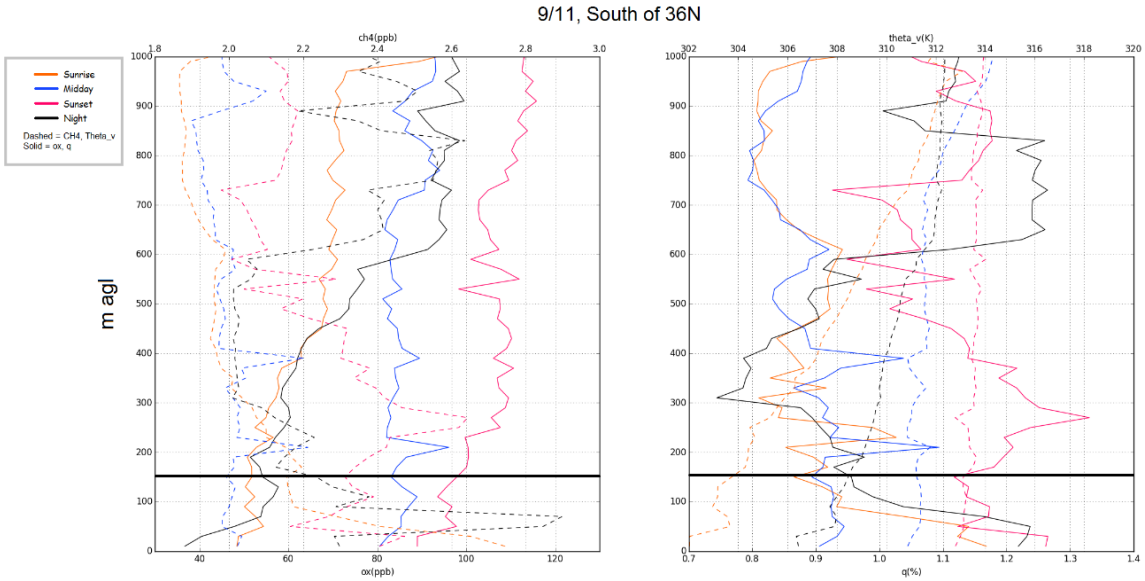

Figure 8. Near surface profiles south of 36N of (left) O_x (solid lines) and CH_4 (dashed lines), and (right) virtual potential temperature (dashed) and water vapor (solid) for the four flights on 11-Sep-15.

Quarter 4

During the winter season between the 2015 and 2016 deployments, we customized the NO_x instrument with a pre-reaction chamber to better account for chemical artifacts in the chemiluminescence instrumental technique. The pre-reaction chamber subsystem is toggled by an externally controlled valve so that we can tailor the intervals of pre-reaction measurement to the needs of our airborne sampling, just as we can the lamp cycling frequency between NO_x and NO measurements.

Completed Upgrades to NO_x Instrument

Extensive work was done on calibrating the EcoPhysics chemiluminescence instrument that measures NO_x. Results show that subtracting a pre-reaction background improves the effects of chemical interferences in the measurement. As the pre-reaction system was absent from the first deployment, the NO and NO_2 measurements were revised to account for a small (~2 ppbv) offset in the NO_2 measurements.

The custom-built system is toggled by an external 3-way valve externally controlled by the aircraft software, and thus much like the photolysis lamp cycling, can be adjusted for the environment and sampling strategy of our deployments. We have also procured a chemical zero (Purafil, http://www.purafil.com/products/chemical-filtration/chemical-media/), and were able to achieve absolute zero NO_x concentrations from any air source. A laboratory calibration (Figure 9) shows excellent performance with the pre-reaction chamber.

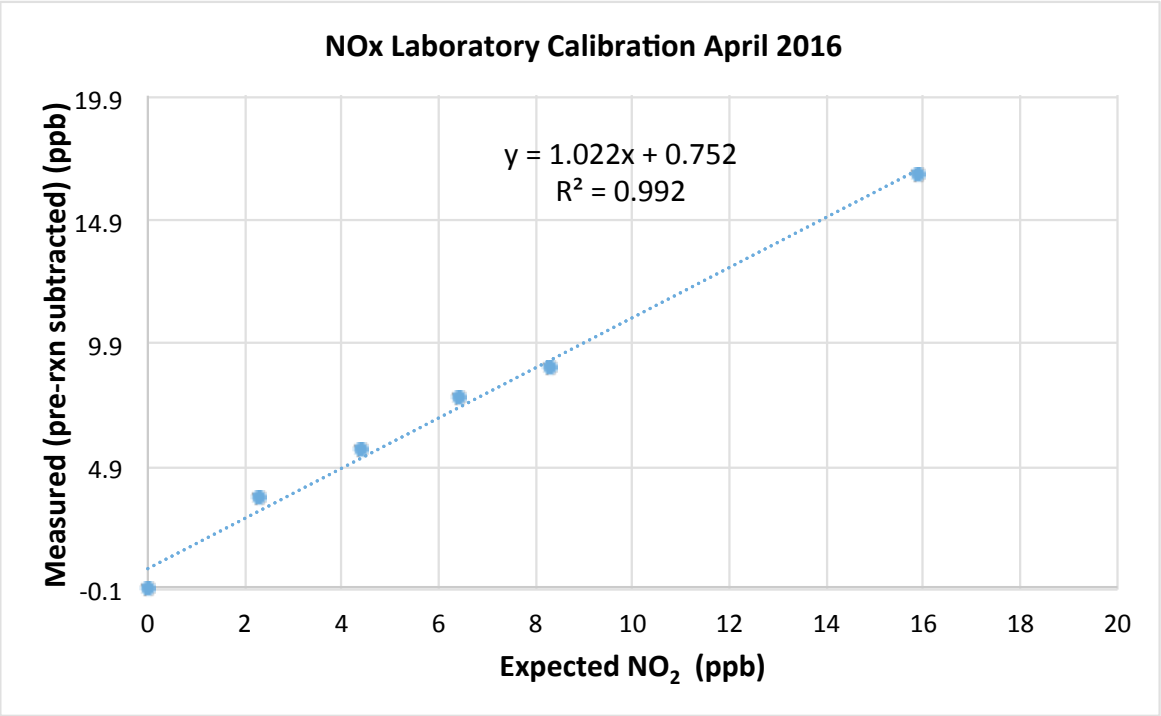

Figure 9. Laboratory calibration of the NO_x chemiluminescence instrument using Purafil air source and O_3 titration of cylinder NO with pre-reaction chamber subtraction performed in between the first and second deployments.

Tenaya fire smoke influence of the Northern domain

Previously, a rough cutoff of 36 degrees North latitude was used to differentiate areas that were and were not influenced by the smoke (with smoke to the north of the cutoff) during the first deployment. The Tenaya fire, which burned a total of 415 acres in Yosemite National Park from September 7-11, 2015, was active during the deployment and was situated along the north rim of Yosemite Valley. The axis of the SJV was approximated with the geometrical line y=-1.4345x in Cartesian coordinates, with +x pointing east and +y pointing north, centered at the base station (KFAT). Then, measurements of ozone, NO_x, and methane from all afternoon flights were projected onto this line in 10 km bins. Separate analyses were performed for all heights combined and measurements below 800 meters MSL (the average afternoon boundary layer height). While no signal gradient was detected from NO_x (not shown), the ozone and methane patterns show unambiguous interference within 40 km along-valley of KFAT, with some interference out to 100 km (Figure 10). Therefore, this 100 km valley-component threshold was treated as a cutoff for splitting the areas that were and were not influenced by fire smoke from the Tenaya Fire during the first deployment.

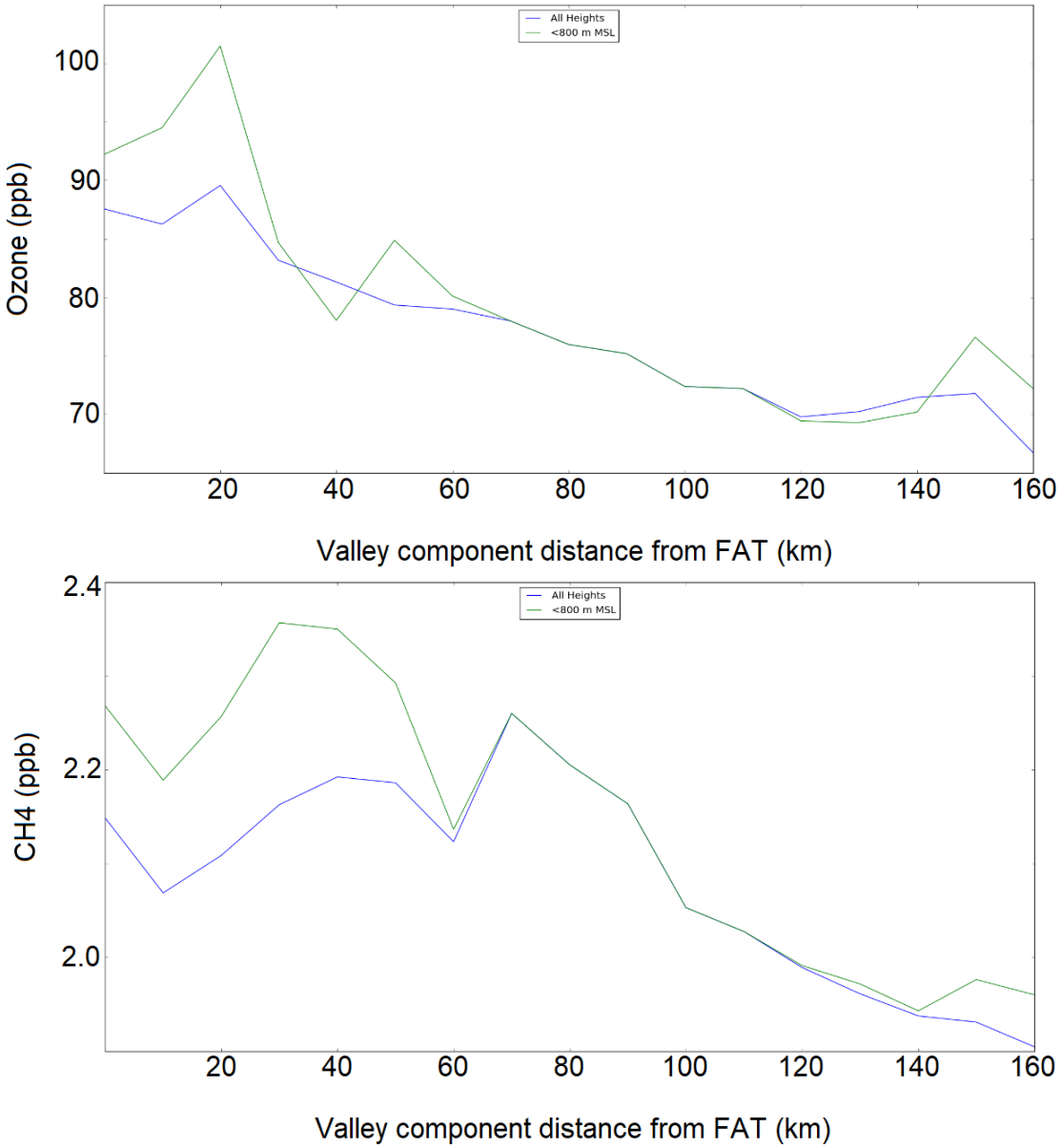

Figure 10. Along valley gradients of O_3 and CH_4 observed during the all three afternoon flights of the first deployment influenced by the Tenaya wildfire effluent.

Morning and Afternoon Ozone Relationship

In past work with the San Joaquin Valley Air Pollution Control District to study the ozone problem in Arvin, CA our group conducted 11 flight deployments over the southern SJV between 2013 June and 2014 June [*Trousdell et al.*, 2016] and discovered a very strong correlation between 8 am PST ozone and Maximum Daily 8-hour Average (MDA8) ozone in Arvin, CA, at a surface-based monitoring location (Di Giorgio Elementary School). For the 11 flight days, the r^2 value obtained was 0.95. A full analysis was performed to determine whether or not this correlation was specific to the 11 days, and if not, to

investigate if the correlation was specific to the southern part of the valley. This would be a critical piece in understanding the role of nocturnal mixing in high ozone events in the southern SJV, which heavily ties in to the mission of this project. Additionally, all flights on this project passed within 10 km of Arvin, so this site is within the field range of the present study.

Variables analyzed included 8 am ozone, MDA8, Daily Maximum Temperature, Daily Minimum Temperature, Daily Average Ozone, and Daily Maximum Ozone. When including data points for the full 2013-2014 years for Arvin, the correlation between surface measured 8 am Ozone and MDA8 was still present, but somewhat weaker (compared to the flight days), with an r^2 value of 0.72. However, when including data from the meteorological summer only (1 June through 30 September), the r^2 value drops to 0.46 (Figure 11). This correlation is comparable to those reported by *Aneja et al.* [2000] between overnight RL [O_3] at 430 m and the following afternoon's hourly maximum surface [O_3] during summer months in Auburn, NC.

Ozone and temperature data were obtained for Fresno and Bakersfield (temperatures from FAT and BFL, ozone from Parlier and L45, respectively), for 2012 through 2015 (4 years). A determination coefficient for year-round 8am ozone and MDA8 of 0.67 is obtained in Fresno, and 0.68 for Bakersfield. Like Arvin, the relationship held only for year round data, with the determination coefficient dropping to 0.34 for Fresno and 0.30 for Bakersfield when only days from summer (the ozone season) are included. The 8:00 a.m. ozone values were better at predicting the daily average ozone, with determination coefficients of 0.82 and 0.78 for Fresno and Bakersfield, respectively. Additionally, the daily maximum temperature was a fairly good predictor of MDA8, with an r^2 value (year-round data included) of 0.77 and 0.73 for Fresno and Bakersfield, respectively.

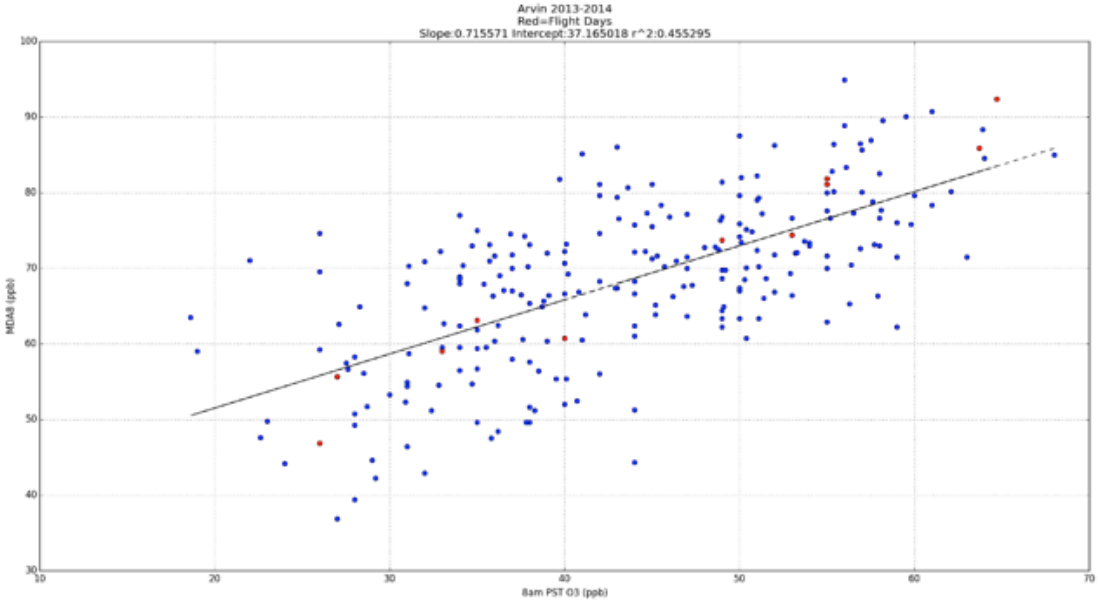

Figure 11. Correlation of 8 a.m. ozone concentration and the MDA8 for the same day at Arvin for two summers (2013-2014). Red points are from the days of the aircraft experiments, which by chance show a much stronger correlation.

Quarter 5

During the fifth quarter of the project, we made two deployment attempts. The first (second of the entire project) occurred between 2-5 June, 2016 to take advantage of ridging synoptic conditions, and the first deployment of the NOAA TOPAZ Lidar for the CABOTS project. The timing of this deployment was delayed by one flight because of technical difficulties encountered before the transit to Fresno. Instead of the usual departure the evening before the first full day of flying, we departed early in the a.m. the day of the first flight sequence and started the experiment with the ~13:00 flight on 2 June 2016. After the late afternoon flight on 4 June, a problem with the airplane's alternator was discovered. Consequently, the aircraft needed to fly directly to the mechanical shop, and we therefore only completed 10 out of the usual 12 flights during that deployment. Then, during a second deployment beginning on 28 June 2016, after three successful flights, the baggage door came open shortly after takeoff. Although the pilot was able to land safely, the fuselage had suffered damage and the remaining flights for this deployment had to be cancelled. Following this incident, safety protocol for our aircraft operations were enhanced, and each member of the group who were allowed to fly as a flight scientist had to go through a training program and pass an exam that represents a substantial subset of the FAA private ground pilot knowledge test.

Further characterization of the NO_x Instrument

Further work was performed to characterize the NO_x instrument, building on what was done from the previous quarter. The small ~2 ppbv offset in the NO_2 measurements was confirmed by an intercomparison with the surface NO_x network during the September 2015 deployment. We further characterized the altitude dependence of the chemiluminescence sensitivity, which we believe occurs due to decreased oxygen and thus O_3 production by the ozonator. A reference cylinder of NIST certified NO at 107 ppb blended by Scott-Marrin was fed to the instrument on a deep profile up to 4.5 km (MSL). The drop in sensitivity amounted to ~2.5%/km (**Error! Reference source not found.**), and was used to correct the data supplied to ARB. It should be noted that above approximately 4 km (MSL) the NO_x instrument loses most of its sensitivity and results above this altitude are likely meaningless. This is believed to occur in an unpressurized aircraft because of an insufficient supply of oxygen to the ozonator. These findings have been accounted for in the final data set provided to the ARB, for both NO_x measurements and their quality flags (Table 1).

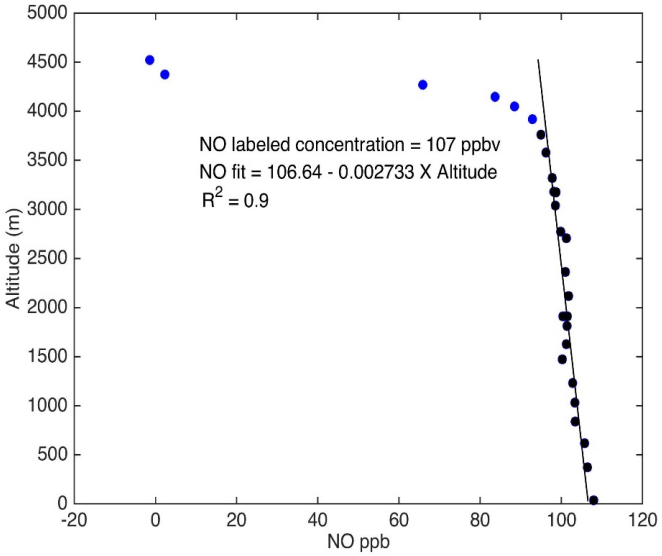

Figure 12. An airborne test of the sensitivity of the NO chemiluminescence instrument as a function of aircraft altitude.

Second Deployment (2-4 June, 2016)

We deployed in early June to take advantage of a developing ridge over the San Joaquin Valley. Because of some delays in integrating the payload on short notice (during the end of the academic Spring quarter), we did not depart Lincoln for the transit until the early morning of the first day (2-Jun-16), delaying the flight sequence by one flight. Even at this early stage of the summer season there was a significant wildfire in the Sierras, 50 km to the northeast of Bakersfield. The Chimney Fire (http://inciweb.nwcg.gov/incident/4757/) started on June 1 and burned 1,300 acres, but did not apparently influence the valley very strongly. Figure 13 displays the IR satellite image with the 500 hPa heights showing the ridge building across the region, as well as the mid-level cloud that crept into the region associated with that shortwave trough on the upwind side of the ridge. The cloud cover was limited to the north side of the domain during the first day, was mostly clear the second, but became prevalent throughout most of the Southern SJV on the third day (4-Jun-16).

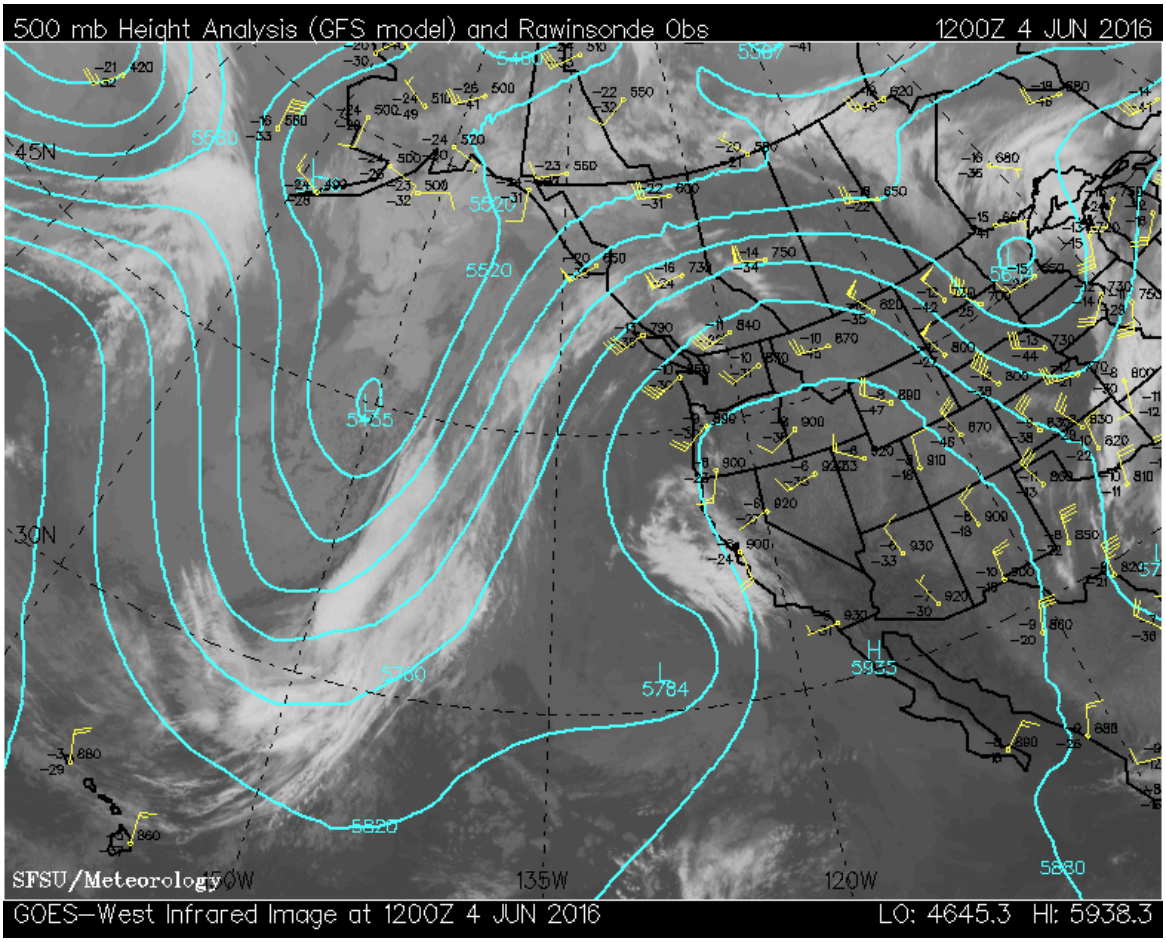

Figure 13. GOES IR satellite image from the early morning of the first deployment of 2016. Image from San Francisco State University's Meteorology California Regional Weather Server (http://virga.sfsu.edu/crws/press.html).

Third Deployment 28-29 June, 2016

Another deployment was attempted at the end of June around temperatures of 105°F, on June 28. After 3 local science flights, in the middle of the day on June 29, the aircraft was unable to be stored in a hangar between the morning and midday flights. Consequently, the instruments overheated on the tarmac in the blistering sun. To combat the extreme heat encountered in this environment, when hangar space was not made available by the local FBO, we have since procured custom heat shields for the aircraft to prevent overheating.

After the instruments were sufficiently cooled with ice and fans, during takeoff of the evening flight, the baggage compartment door opened in flight causing some damage to the fuselage and forcing us to abort the deployment. Since then, we have instituted a comprehensive safety and pilot training for all students and postdocs (and professors) working on or around the aircraft.

Quarter 6

During this period, we completed two deployments (numbered 4 and 5 in the final dataset). The fourth deployment occurred between 23-26 July, 2016 to take advantage of ridging synoptic conditions, and the second deployment of the NOAA TOPAZ Lidar for the CABOTS project. The timing of this deployment was completed as planned with a transit flight on the late afternoon of July 23, and 3 consecutive flight days around the clock from 24-26 July. The aircraft stayed on afterwards in Fresno for 3 additional daytime flights for the EPA/BAAQMD sponsored CABOTS flights. The transit back to Sacramento took place on 30 July. The fifth and final deployment began with an extended transit flight crossing Chews Ridge (and the Soberanes Fire) on 11 Aug, 2016, and wound up being double the duration. Due to the perception that the ozone season was waning, the project team decided to extend the stay and operate continuously from 12-18 Aug. There were some aircraft system difficulties with the alternator breaker on the evening of 13 August, but these were resolved while creating only a 2 flight gap in the sampling, so the flights continued through the middle of the day 18 August, 2016, with the transit that same afternoon.

Continued measurements at Chews Ridge

The Soberanes Fire (https://inciweb.nwcg.gov/incident/4888/) started on July 22 and scorched 132,000 acres, sending fire smoke throughout the region, and burning right up to the edge of the Chews Ridge observatory. Figure 14 shows two different satellite images of the fire: on the left is a MODIS true color image from late July showing the smoke spreading across the region and advecting over the San Joaquin Valley; and on the right is a Landsat IR satellite image from mid-September showing the extensive burn scar from the fire after 2 of the 3 months it blazed. The fire smoke was a persistent feature of the airborne deployments 4 and 5 of the project, with many large spikes in NO_x observed in thin layers over the SJV. Measurements of O_3 and NO_x continued at the Chews Ridge site uninterrupted during the fire despite the imminent threat to the site. Figure 15 shows a picture taken from the Chews Ridge observatory showing the heavy smoke cover obscuring the sun and reducing actinic fluxes in the middle of the day.

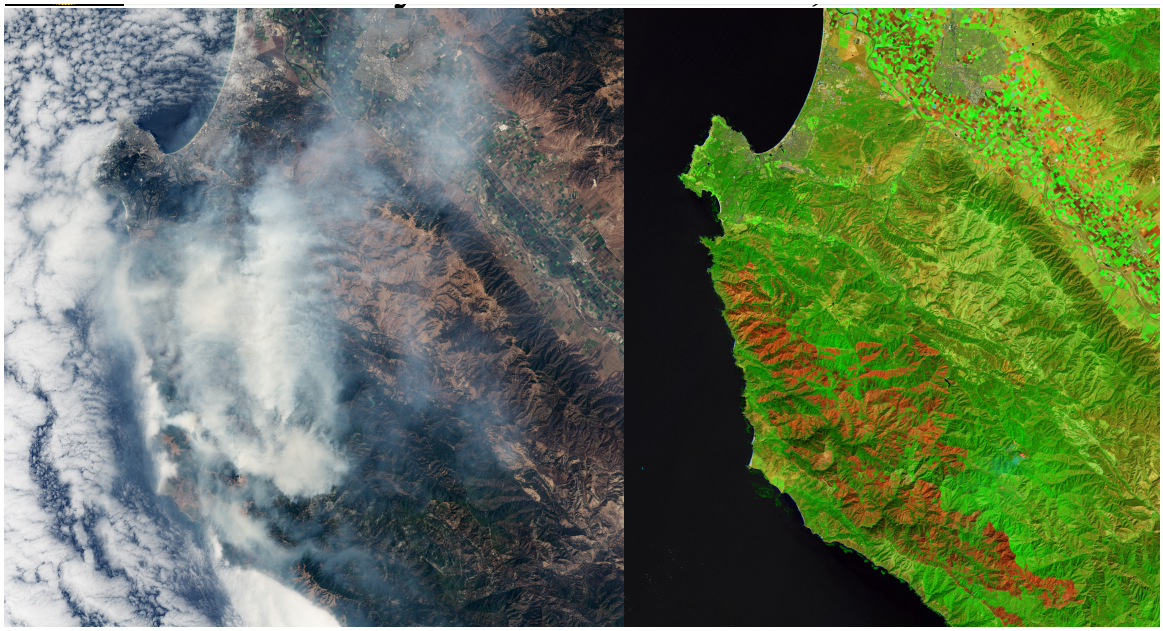

Figure 14. MODIS satellite true color image of the Soberanes Fire smoke from 29-Jul-2016 impacting the region including the SJV to the east during deployment 3. (right) Landsat OLI satellite product of the burn scar from the fire on 16-Sep-2016.

Ancillary EPA/BAAQMD flights upwind of the NOAA TOPAZ Lidar

In mid-July, 2016, we were awarded a grant by the EPA (with funds flowing through the BAAQMD) to participate in CABOTS more directly. Forty-three flight hours were used to fly six days with two sorties each. The morning flights were to fly towards the coast (either near San Jose or Chews Ridge) and back at middle altitudes to connect the sonde and Chews Ridge measurements to the San Juaquin Valley. The afternoon sorties consisted of four hours back and forth between Fresno and Visalia, where the NOAA lidar was stationed to investigate the ozone budget upwind of the lidar. These flights were successfully completed after the fourth deployment (July 27-29), and then again on a separate trip to ensure overlap with the NOAA lidar deployment from August 4-6.

Figure 15. Photograph of smoke cover from the Soberanes Fire taken from the Chews Ridge observing station.

At the request of ARB staff during the fifth deployment, the aircraft made a point to profile up to ~3 km AGL above Lake Kaweah, 40 km to the east-northeast of the Visalia airport, in order to coincide with the surface measurements in the Sierras on the lee side of the valley. These data reveal a very deep (2-2.5 km) region of enhanced ozone, NO_x, and often CH_4 approximately 500–1000 m above the boundary layer, likely indicative of the lofting and recirculation above the boundary layer (into the buffer layer) which is not efficiently ventilated out of the valley, contributing to persistent air quality problems by acting as a reservoir of regional pollution.

Quarter 7

During this period, we completed the post-mission calibrations and interference characterization. Throughout the quarter our team continued active participation in ongoing CABOTS science meetings (July 14 & October 20, 2016) to review preliminary findings and advance discussions. We kept the Chews Ridge O_3 and NO_x measurements running through the end of the year, in spite of running out of support from the SJVAPCD who initiated that project nearly four years prior. That finalized data has been submitted to the CABOTS data archive (https://www.esrl.noaa.gov/csd/projects/cabots/) along with the flight data from the six add-on flights supported by funding from the EPA/BAAQMD to enhance flight data coverage upwind of the NOAA lidar during CABOTS.

Below are plots of the airborne O_3, NO_x, and altitude (above mean sea level, ASL) data collected on a midnight flight of 16 August and the midday flight the following day in 2016. The surface of the SSJV is between ~ 90 m (ASL) at KFAT to ~150 m (ASL) at KBFL. The altitude (black line) dips in Figure 16 represent the low-passes over the three airports (KVIS, KDLO, and KBFL), and the high profiles to ~2km are at the beginning and end of each flight near Fresno and the one in the middle is near Bakersfield. The top plot of Figure 16 shows the strong vertical gradients in NO_x and O_3 near the surface at night (in the NBL), while the bottom plot shows the well-mixed nature of the lower 600-700 m (in the ABL) during the day.

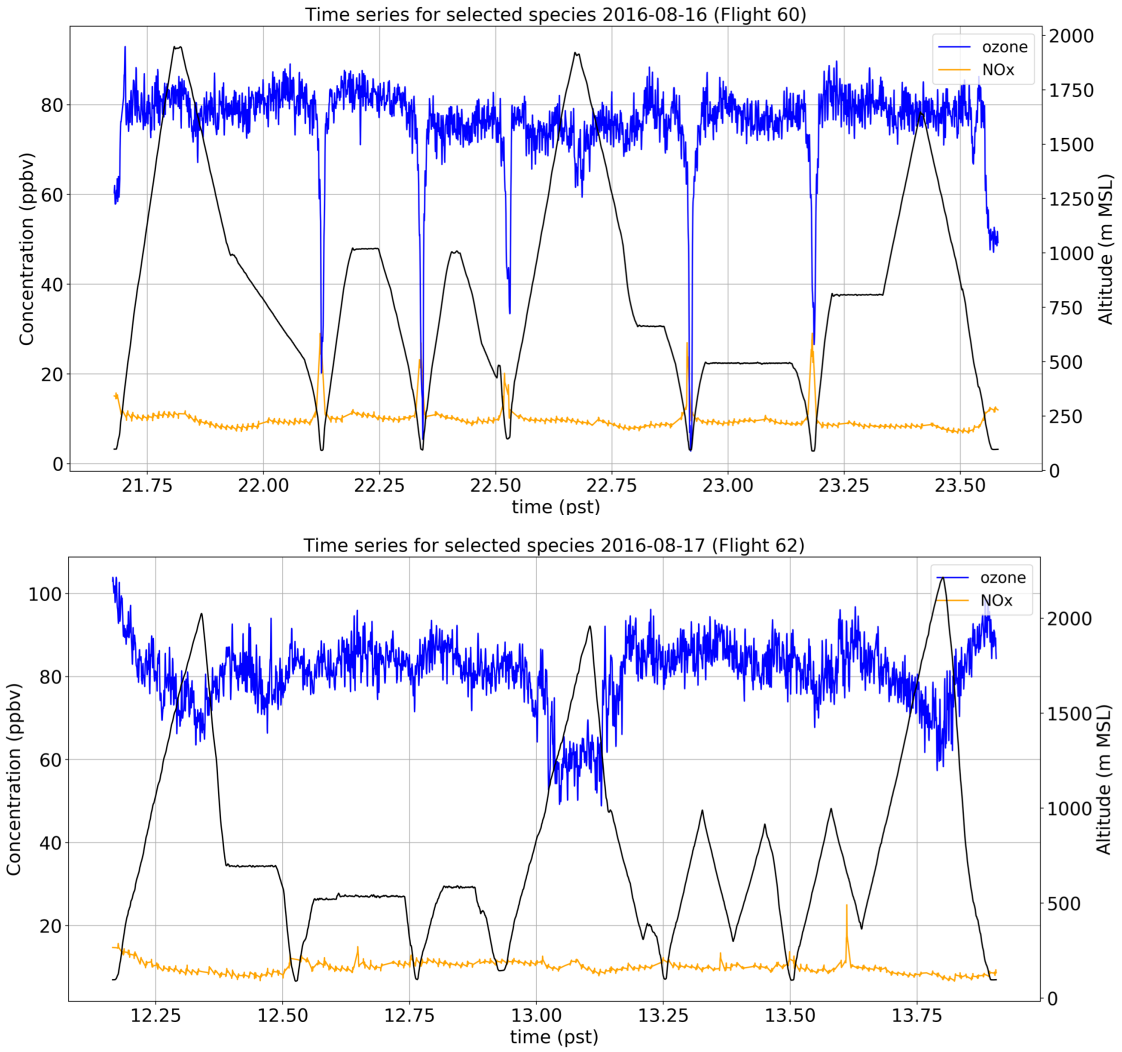

Figure 16. Time series of (top) midnight flight from 16-Aug-2016 and (bottom) midday flight the following day.

Additional estimates of entrainment and local O_3 production

Following procedures outlined in *Trousdell et al.* [2016] to estimate the entrainment velocities and ozone photochemical production rates, we used the afternoon add-on EPA/BAAQMD flights to extend these results. It is interesting to note that entrainment velocities measured by a completely independent method on three flights across the Central Valley and foothills in 2011 by *Karl et al.* [2013] span the range of those reported in this work and in *Trousdell et al.* [2016]. Comparisons within the Central Valley reveal entrainment velocities in the region between Fresno and Visalia that appear to be on average ~30% larger than those over the Bakersfield/Arvin area, but the in-situ O_3 net photochemical production rates are very similar, ~8 ppb/hr during the afternoon hours. The data presented in a later section, and encapsulated in Table 5, is reported as the EPA and RLO flights in Table 2.

Table 2. Summary of ABL growth rates, model subsidence, net ozone production, and entrainment rates from the current study and three other airborne experiments in the SJV. Standard deviations

Project	Date	Location	ABL Growth Rate $\partial z/\partial t$ (cm/s)	Subsidence W (cm/s)	O_3 Photochemical Production (ppb/hr)	Entrainment Velocity w_e (cm/s)
DISCOVER-AQ (Trousdell et al., 2016)	Jan-Feb, 2013	Fresno	1.5 (1.0)	-0.8 (1.1)	2.8 (0.7)	1.5 (0.9)
ArvinO3 (Trousdell et al., 2016)	Jun-Sep, 2013/14	Bakersfield	3.0 (1.2)	1.2 (0.9)	8.2 (3.1)	3.0 (2.1)
EPA Flights (this work)	Jul-Aug, 2016	Fresno/ Visalia	1.3 (1.7)	-1.1 (0.6)	6.3 (3.3)	2.7 (1.2)
RLO Flights (this work)	Jun-Sep, 2015/16	Fresno - Bakersfield	2.7 (1.2)	-2.1 (0.6)	7.3 (3.4)	5.1 (1.7)
CABERNET (Karl et al., 2013)	May, 2011	SJV & Sierra Foothills	NA	NA	NA	1.4, 5.5, 9.6

Quarters 8 and 9

During this period we focused our analyses on the Fresno Eddy and its role in mixing air between the residual layer and the nocturnal boundary layer overnight, and the consequence of this mixing on the afternoon's MDA8 value. Aircraft data from the Residual Layer Ozone project as well as Radio Acoustic Sounding System (RASS) data from Visalia, CA, are utilized heavily. We also made strides at disseminating the preliminary data to the scientific and regulatory community. Beyond the advancement of four separate AGU presentations for the Fall 2016 AGU conference in San Francisco, we presented the nocturnal mixing work at the Berkeley Atmospheric Science Center Symposium in Berkeley February 2-3, 2017. We also presented a talk and two posters at the WESTAR Background Ozone Scientific Assessment Workshop in Denver, CO at the end of March to an audience of leading scientists and air pollution control officers throughout the western US. Additionally, we participated in the CABOTS science team meeting held at ARB in April, including providing airborne and Chews Ridge data to the archive.

Relationship of Onshore O_3 Advection with SJV O_3

Working with the CABOTS science team we were able to synthesize our airborne measurements with data collected by ozonesonde at the Bodega Marine Lab (BML) by the San José State University team led by Professor Sen Chiao. Figure 17 shows that approximately half of the variance of the O_3 observed at 700 m altitude (the mean height of the ABL) over Fresno is explainable by the levels coming onshore at Bodega Bay 6-12 hours before at the same altitude. This is a fairly remarkable finding given that Fresno is 330 km southeast of BML and air in the buffer layer above the ABL is made up of lofted valley air. However, similar correlations are found between the Bodega Bay ozonesonde data and Chews Ridge which is 260 km down the coast. This could be explained by the fact that the frequently observed lamina of ozone and water vapor in the free troposphere tend to be thin and quite horizontally expansive. A study of 13 historical ozonesonde sites in the midlatitudes across Europe and North America found the average *e*-folding distance of decorrelation to be 500-800 km [*Liu et al.*, 2009]. Therefore, in spite of the fact that the flow above the ABL at Bodega Bay usually passes to the northeast into the Sacramento Valley, the onshore advection of these broad lamina leads to significant correlations in the cross-stream direction. The correlation is seen to degrade farther down the valley away from BML as seen in the data from the Visalia profiles. Nevertheless, this gives us a statistical way to connect the importance of the lateral boundary condition to the vertical boundary conditions of the ABL and the levels of ozone in the buffer layer that determine, in part, the dilution rate due to entrainment. From previous work in the Bakersfield area we have estimated that the afternoon entrainment dilution is about one-quarter of the net photochemical ozone production during the summertime [*Trousdell et al.*, 2016].

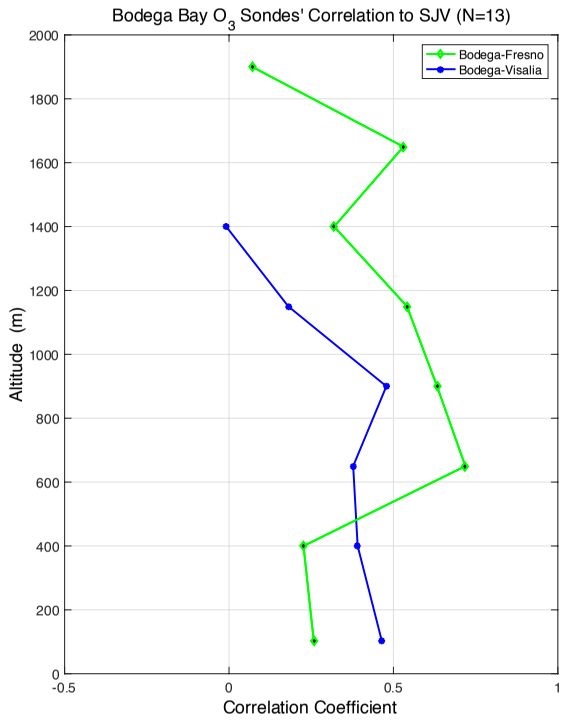

Figure 17. Altitude binned correlation data between flight profiles near Fresno and Visalia and Ozone Sondes launched from Bodega Bay 6-12 hours earlier the same day.

Conceptual framework of the transboundary ozone transport

In order to refine our understanding of transport patterns of flow from coastal sites like Bodega Bay and Chews Ridge to the surface air in the Central Valley, we have developed a conceptual model to describe the lower atmosphere over the San Joaquin Valley. The correlations between the Bodega Bay (BBY) and Half-Moon Bay (HMB) sondes, separated

by a distance of 110 km, indicate that the correspondence occurs in a bimodal fashion with peak correlations of r = 0.5-0.6, at altitudes of 1.5 and 8 km, again speaking to the wide extent of the laminated features. The days in which near simultaneous sondes were launched at both sites number 24 in the interval from 24 July to 17 August, 2016. Peak correlations between BBY sondes and simultaneous O_3 measurements at Chews Ridge (N=86), and between HMB and Chews Ridge were very similar at 1700 m (HMB) and 1900 m, where the Chews Ridge measurements are made at 1550 m. This is consistent with the sloping up with latitude of ozone levels observed during IONS-2010 [*Cooper et al.*, 2011]. Meanwhile, low-level flight data over Fresno and Visalia when combined for periods 6-12 hours after the BBY sonde launch, indicate a correlation peak right near the top of the daytime boundary layer near Fresno (Figure 17) for the sample size of 13 evening flights on days of BBY sonde launches. These correlation strengths are similar to those presented in [*Parrish et al.*, 2010], and are consistent with air masses moving east across the state and bringing ozone layers above in contact with an actively entraining boundary layer. However, the air between ~750 m (approximate top of the SJV boundary layers) and 3,000 m tends to stagnate up against the Sierras, and is also heavily influenced by lofting along the valley sidewalls and therefore this layer acts as a 'leaky' reservoir (buffer layer) of regional ozone. The overall schematic of the transport process is shown in Figure 18 below.

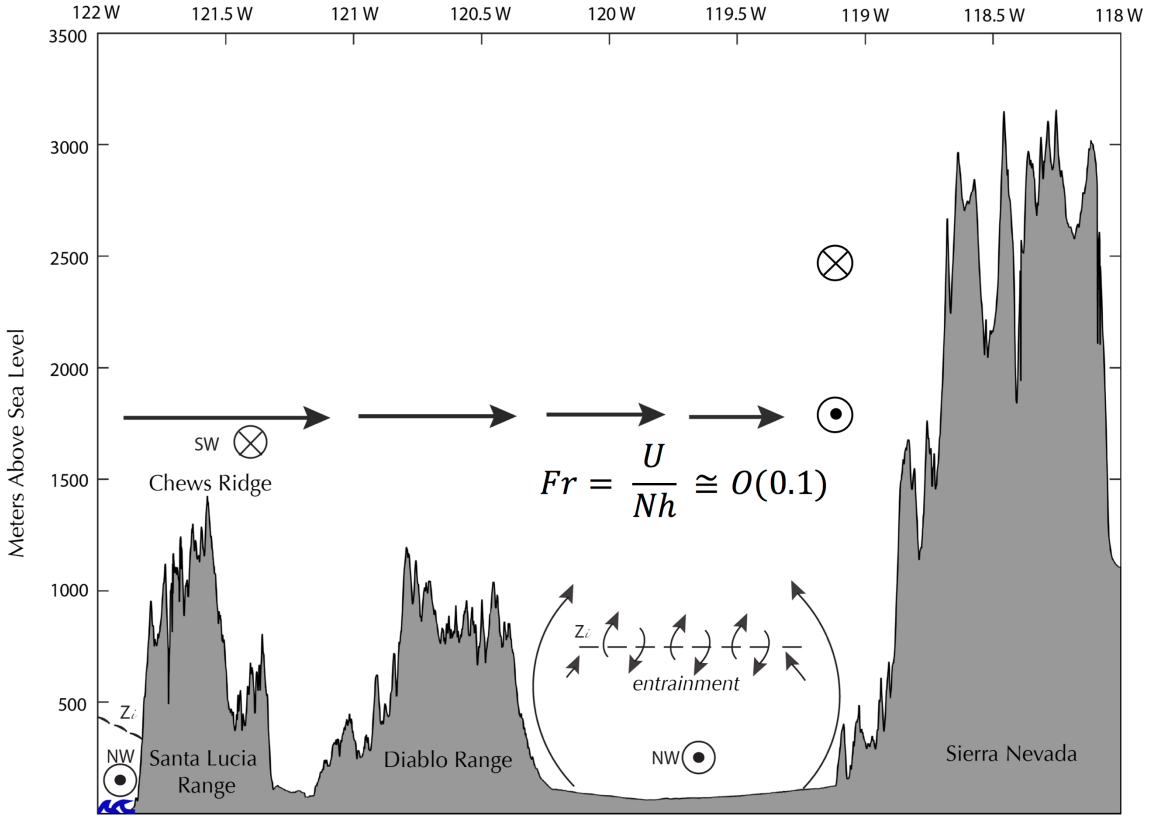

Figure 18. Terrain cross-section running from the coast near Chews Ridge to the Sierra Nevada Mountains to the east. Fr is the Froude Number, U is the horizontal wind speed, N is the Brunt-Vaisala frequency, and h is the height of the barrier of the Sierras.

The Froude Number, *Fr*, is the ratio of horizontal kinetic energy of the flow (*U* is the wind speed) to the potential energy associated with rising over the mountain barrier (of height, *h*) in the static stability (*N* is the Brunt-Vaisala frequency) of the lower troposphere. Typical values for the climatological southwesterly wind that flows over the Central Valley is ~0.1 leading to stagnation. Slowing of the wind weakens the Coriolis force leading to southerly flow down the pressure gradient above about 2.5-3.0 km altitude. Below that the flow is northwesterly following the up-valley circulation. Figure 19 shows the mean (and standard deviation) profiles of potential temperature, ozone, methane, estimated turbulent kinetic energy (TKE), and wind speed for the 15 midday flights. The three layer conceptual model is readily observed in these data. The lowest 600-700 m is the conventional 'well-mixed' convective boundary layer where the local emissions of methane and ozone precursors create the most polluted air, and the most vigorous turbulence exists due to the surface buoyancy fluxes and surface wind shear. Above ~2100 m the free troposphere is seen where concentrations fall to "background" levels. And in between the two, there is a slightly stable "buffer layer" where the characteristics are intermediate, a blend of boundary layer and inflowing free tropospheric air, and turbulent motions are weaker and more intermittent.

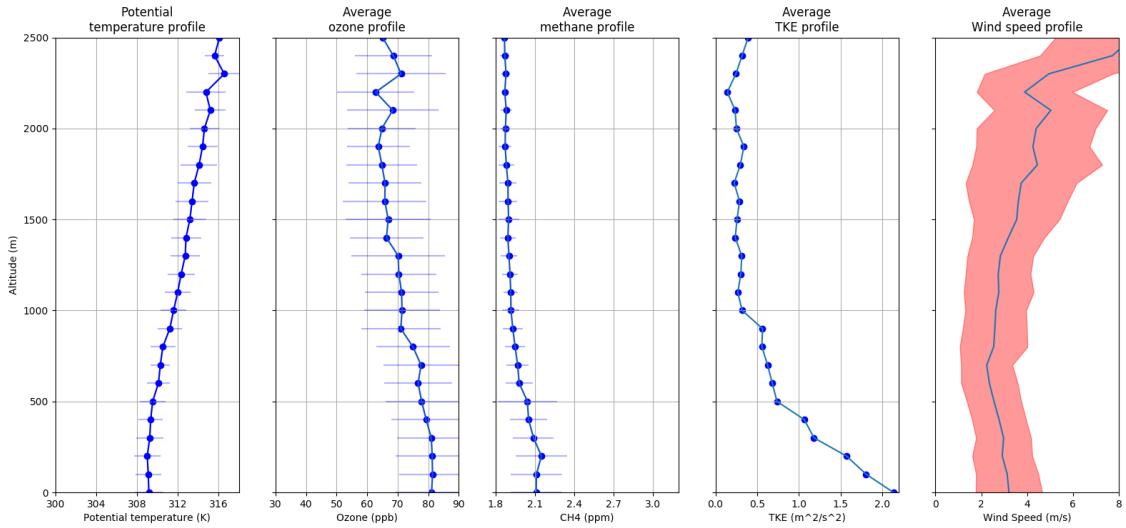

Figure 19. Mean profiles of (left to right) potential temperature, ozone, methane, turbulent kinetic energy, and wind speed for all 15 midday flights.

Preliminary analysis with WRF output from runs during the same days indicates that the effective residence time of air in the "buffer layer" with respect to being flushed out is approximately 6-7 days.

Continued Work on CABOTS Data Set

Two of the deployments for the residual layer project (2-4 June and 24-26 July 2016, numbers 2 and 4) and the 6 flights for the EPA CABOTS project (27-27 July and 4-6 August, 2016) were flown concurrently with the NOAA TOPAZ lidar being operated at the Visalia airport. A comparison of the data collected concurrently on 26 July, 2016 is shown in Figure 20. The independent data sets show remarkable consistency considering that the aircraft data is averaged across the entire domain from Fresno to Bakersfield. Both

profiles exhibit distinct ozone minima (40-50 ppbv) at 1500 and 2200 m altitude. The other variables exhibit the frequently observed layering discussed previously: a well-mixed ABL below about 600 m, an intermediate layer between 600-2000 m, and a 'background' free troposphere above that.

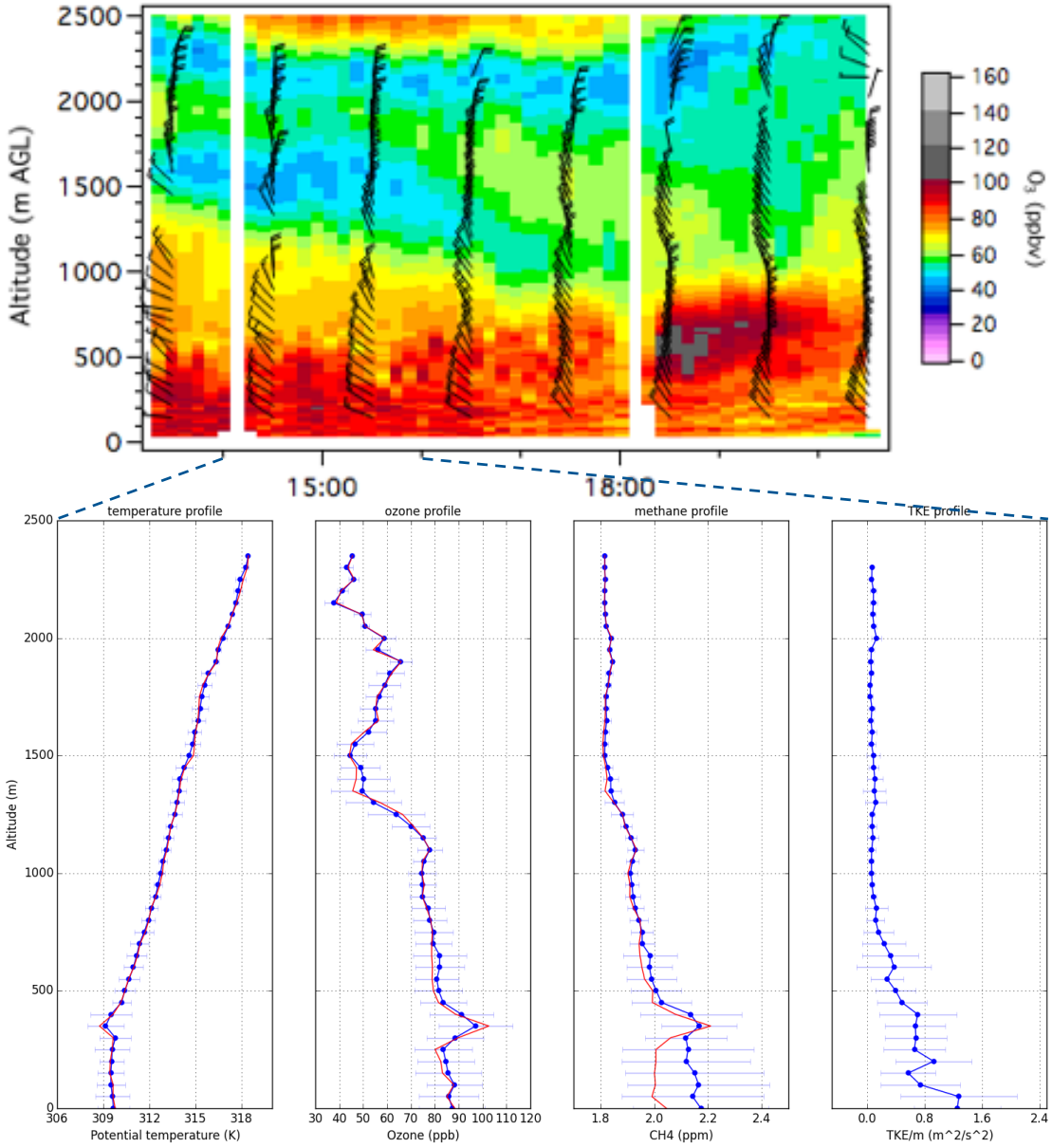

Figure 20. (top) NOAA TOPAZ lidar data with Visalia wind profiler data superimposed on the afternoon of 26-July-2016, and (bottom) the mean/median (blue/red) profiles observed by the aircraft (14:00-16:00 PDT.)

OVERALL PROJECT RESULTS AND DISCUSSIONS

Overnight O_x Budget Analysis and Mixing Rates

One of many central questions that can be explored from the aircraft data is to test the importance of the nocturnal mixing on the ozone budget in this region. This objective aims to use a similar method that has been presented with daytime scalar budgets ([*Trousdell et al.*, 2016]; [*Faloona et al.*, 2009]; [*Conley et al.*, 2011]) to further demonstrate the overall practicality of this paradigm. Analyzing such budgets allows one to answer the critical questions regarding what is ultimately controlling the pollution in a fixed location or area.

The nocturnal budget equation is formulated for the chemical species O_x, defined here as NO_2+O_3, in order to avoid the effects of titration of O_3 by NO. NO_2 will photolyze the following day to reproduce ozone, so it acts as an overnight reservoir of ozone. The chemical loss of O_x then is tracked by the reaction between O_3 and NO_2 to form nitrate, but its ultimate fate will affect the overall O_x loss (to be discussed later.) In the stable nighttime environment we will treat the mixing between the RL and NBL as analogous to molecular diffusion by using an eddy diffusivity. The NBL O_x budget can thus be represented as

$$\frac{\partial[O_x]}{\partial t} = -\alpha k_{O3+NO2}[O_3][NO_2] - \bar{u}\frac{\overline{\Delta[O_x]}}{\Delta x} - \bar{v}\frac{\overline{\Delta[O_x]}}{\Delta y} + \frac{-[O_3]_{SFC^*}|v_d|}{h} + \frac{K_z\frac{\Delta[O_x]}{\Delta z}}{h} \qquad (6)$$

Where the term on the left represents the change in concentration with respect to time within the flight volume. The leftmost term on the right side of the equation represents the net loss of the O_x due to nitrate production and loss (containing an unknown constant of proportionality, α, that can range from 0–3 and depends on the dominant sink of NO_3.) The next two terms represent changes due to advection by the horizontal wind, followed by terms representing the dry deposition of ozone to the surface, and finally the vertical turbulent mixing term that uses the vertical gradient and the eddy diffusivity, K_z – a number that encapsulates the strength of the overnight mixing. By calculating the first five terms in Equation 6 using the aircraft data we can indirectly estimate K_z.

The odd oxygen family (O_x) is usually defined as O_3+NO_2+$2NO_3$+$3N_2O_5$, species that can all regenerate O_3 in the presence of sunlight. However, because we were unable to measure the higher NO_y species, we will define O_x as only =O_3+NO_2. Aside from dry deposition to the Earth's surface, NO_x chemistry is the main loss of ozone at night, counteracting its role in production during the daytime [*Brown et al.*, 2006]. Nocturnal chemical destruction proceeds by the following reactions, beginning with nitrate radical production:

(R1) $NO + O_3 \rightarrow NO_2 + O_2$
(R2) $NO_2 + O_3 \rightarrow NO_3 + O_2$

NO_3 photolyzes readily once the sun comes up, so the ultimate net loss of ozone depends on the loss of nitrate in the dark. The main channels of nitrate loss are:

(R3) $NO_3 + NO_2 + M \leftrightarrow N_2O_5 + M$

(R4) $N_2O_5 + H_2O \rightarrow 2HNO_3$
The net reaction of (R1–R4): $NO + 2O_3 + NO_2 \rightarrow 2NO_z$

where $NO_z = NO_y - NO_x$ to represent the products of NO_x oxidation. Or nitrate is lost by reaction with a wide array of organic compounds

(R5) $NO_3 + (VOC, etc.) \rightarrow$ organic nitrates
Net of (R1, R2, R5): $NO + 2O_3 \rightarrow NO_z$

However, in urban environments with nocturnal sources of NO, nitrate is reduced back to NO_2 by the very rapid reaction:

(R6) $NO + NO_3 \rightarrow 2NO_2$
Net of (R1, R2, R6): $2NO + 2O_3 \rightarrow 2NO_2$

If the hydrolysis of N_2O_5 (R4) is the dominant NO_3 sink, then the net reaction leads to a loss of 3 O_x molecules per nitrate produced (R2). However, if the dominant loss is reaction with VOC's (R5) then the net reaction leads to 2 O_x molecules lost per R2. And if there is ample NO R6 will dominate the nitrate loss leading to no O_x loss.

While in this project we were only able to measure O_3, NO, and NO_2 and thus only directly measure the rates of reactions (R1) and (R2), we propose that each effective collision of NO_2 and O_3 will lead to the net loss of approximately 1 molecule of O_x from the net effects of the entire series of reactions outline above (i.e. $\alpha \sim 1$.) Reaction (R6) has often been ignored at night on the presumption that local sources of NO are sparse and reaction (R1) will outcompete reaction (R6) [*Brown et al.*, 2006; *Stutz et al.*, 2010]; however, at 30 ppb O_3 and 20 ppt NO_3 the lifetimes of NO to both reactions are nearly equivalent (~80s). Our measurements indicate near surface [NO] of about 0.6 ± 1.0 ppbv at midnight, corroborated by the surface air quality network, increasing in the early morning hours to 2-4 ppbv. However, these values may be biased high relative to the regional average due to the low passes occurring near Highway 99 or in urban centers. The rate of reaction (R6) is extremely rapid relative to the others (k_{NO+NO3}=2.6 x 10^{-11} $cm^3/s \cdot molec$), such that even 0.5 ppbv of NO results in an NO_3 lifetime of only 3 seconds. There is some question as to whether any VOCs would be able to compete with this NO_3 consumption rate making reaction (R6) negligible for our study. An investigation into the faster VOC reactions with NO_3 indicates that only valley concentrations of limonene, o-cresol, β-caryophyllene , or possibly α-pinene could produce a lifetime of NO_3 within that order of magnitude [*Atkinson et al.*, 2006]. Using the geometric mean values of 10 of the fastest reacting VOCs reported by [*Gentner et al.*, 2014] yields an overall NO_3 lifetime of at most 23 s. Given all the uncertainty, we assume the nitrate loss is matched on average overnight between these two reaction pathways leading to a net loss of about one O_x per nitrate produced (R2). In any event, the ultimate fate of the nitrate radical can be seen to have a very important role in the net loss of O_3 overnight and without a greater understanding of the nitrate budget predicting this loss rate is highly uncertain.

There are reports of ozone dry deposition fluxes in the area of this field campaign from a 1994 study using the eddy covariance technique [*Padro*, 1996]. The findings of their study suggest nocturnal ozone deposition velocities are a few times smaller than their daytime counterparts, but non-negligible for the budgeting technique presented here. Results from a European field study in a similar environment corroborates this finding [*Pio et al.*, 2000]. We estimate a dry deposition velocity of 0.2 cm/s ± 0.1 cm/s for ozone at night in these agricultural regions based on a survey of values reported in the literature.

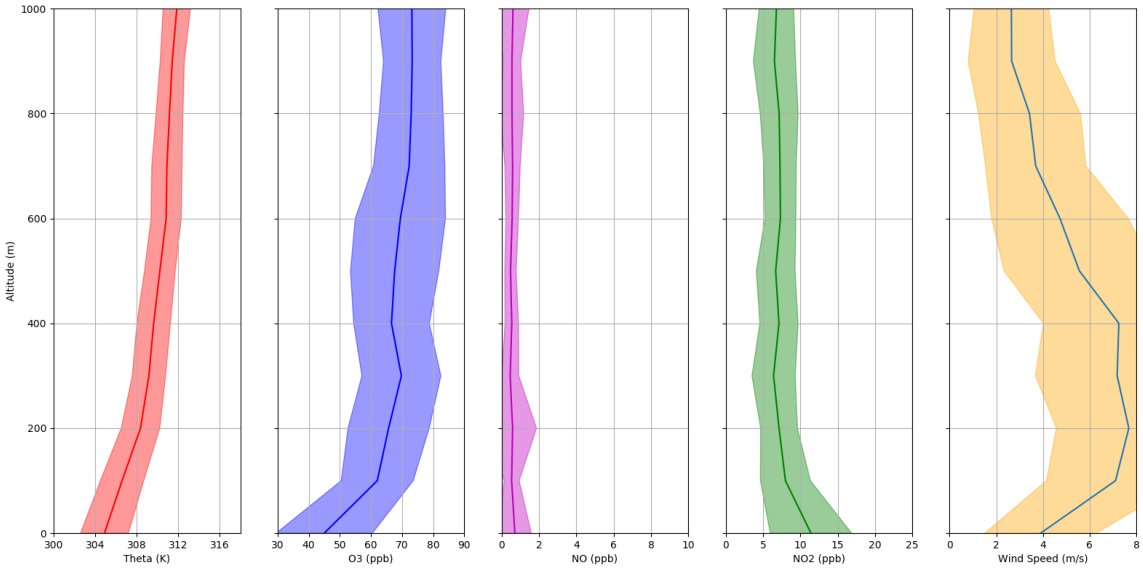

Figure 21. Mean and ±1 standard deviation (swatches) of potential temperature, ozone, NO, NO_2, and wind speed from all midnight flights.

Figure 21 shows the average scalar profiles from all 15 of the midnight flights to give a sense of the gradients in the lower portion of the ABL (sometimes the NBL and the RL together are considered to be the nighttime ABL.) First, values of the stable NBL height (h) are determined for each night. This is crucial to the analysis because it determines the critical layer for which to analyze the chemical loss and advection processes. *Stull* [1988] lists several methods for estimating h. The method used here is to observe the lowest level where the magnitude of $\partial\theta/\partial z$ falls to within some threshold of zero, as this physically represents a layer of air that is in thermodynamic communication with the radiatively cooling surface. While the lapse rates of potential temperature would not always reach zero, it was clear from visual inspection where the transition occurred to the residual layer, which tended to have a stability threshold of around ~2K/km. In addition, averages between the late night and sunrise profiles are taken into consideration. These factors lead to an estimated uncertainty of ± 100 m for all of the NBL heights obtained. The average conditions from the midnight and sunrise flights are presented below in Table 3.

Table 3. Observed NBL heights, ozone, stability, TKE, and LLJ maximum wind speeds observed during the midnight/sunrise flight pairs.

Flight Date	NBL Height h (m)	NBL [O_3] (ppbv)	BV Frequency N (s^{-1})	Mean TKE ($m^2 s^{-2}$)	Jet Max (ms^{-1})
9/11/15	320	21.4	0.024	0.95	8.1
9/12/15	280	24.8	0.021	1.11	4.0
6/3/16	260	36.4	0.021	1.25	12.0
6/4/16	220	38.1	0.026	0.64	5.9
6/29/16	200	33.1	0.023	NaN	10.0
7/25/16	320	31.0	0.022	1.57	6.4
7/26/16	320	31.2	0.023	1.01	8.0
8/13/16	340	38.5	0.020	1.36	9.1
8/15/16	250	30.3	0.023	0.63	10.3
8/16/16	450	29.1	0.022	1.02	9.4
8/17/16	340	28.7	0.024	0.96	6.2
8/18/16	270	31.0	0.025	1.11	5.6
Average	**298**	**31.1**	**0.023**	**1.1**	**7.9**
Standard Dev.	**66**	**5.0**	**0.002**	**0.3**	**2.3**

For the domain of interest, all measured NO_2 and O_3 data was averaged for each 20 m (AGL) altitude bin in order to generate mean vertical profiles of O_x. Separate profiles were created for the late night flight and the subsequent sunrise flight. The height of the stable boundary layer for each night (h) was used as the upper altitude limit when averaging observations to obtain advection, chemical loss, and time rate of change (storage) terms for the budget equation. To estimate the storage term on a given night, first, the average value of O_x from the surface up to the stable NBL height (h) was taken for both the late night and sunrise flights, computed from the 20 m vertical resolution profiles. The late night average was subtracted from the sunrise average and divided by the time difference between the midpoints of each flight.

As previously discussed, the reaction for the nocturnal chemical budget of O_x that we are able to quantify is ozone's destruction with NO_2 (R2). The 2nd order rate equation for the total chemical loss of O_x is calculated by:

$$\left.\frac{dO_x}{dt}\right|_{chem} = -\alpha k_{O3+NO2}[O_3][NO_2] \quad (7)$$

Where α is estimated to be 1 as per the discussion above. To estimate a value for the second order rate constant (k_{O3+NO2}), we start with the temperature dependent function for this reaction:

$$k_{O3+NO2} = 1.2(10^{-13}) * e^{\frac{-2450}{T}} \quad (8)$$

Where T is given in Kelvin. For the domain being analyzed, an instantaneous value of k_{O3+NO2} is determined at each data point. These values of k_{O3+NO2} are then averaged to obtain a constant value for the given night. To estimate the chemical loss of O_x, the initial 20 m altitude bins for NO_2 and O_3 are taken from the late night and sunrise profiles. While no airborne data was collected during the night, the ground network climatology shows a virtually linear change of NO_2 and O_3 during the hours with no flight data. Thus, in each bin, the concentrations are linearly interpolated between the late night and sunrise values, so that there is an estimation of the current average concentration within that bin at every hour during the night.

Advection is calculated by first collecting all 1-second O_3 and NO_2 data points for the late night and sunrise flights separately. A multiple linear regression is fit through the ozone

data for latitude (y), longitude (x), and altitude (z), allowing estimations for $\partial[O_3]/\partial x$ and $\partial[O_3]/\partial y$ in the horizontal advection terms. The total advection term for ozone within the given on a given flight is:

$$A_{O3} = -\left[\left(\frac{\partial[O_3]}{\partial x} * \bar{u}\right) + \left(\frac{\partial[O_3]}{\partial y} * \bar{v}\right)\right] \quad (9)$$

Where u is the mean x-component (zonal) wind within the bin and v is the mean y-component (meridional) wind within the bin. The same procedure is repeated for the NO_2 species for each advection bin for both the late night and sunrise flights. That is, on any given night, one advection term is calculated per flight, per species. The total advection term for O_x is then computed as follows:

$$Advection(O_x) = \frac{A_{NO2\ night} + A_{NO2\ sunrise} + A_{O3\ night} + A_{O3\ sunrise}}{2} \quad (10)$$

Finally, a vertical flux divergence for O_x must be estimated, which is represented by the last two terms in Equation 6. Deposition of ozone is presumed to be the main sink of O_x at the surface, which can be computed as the product of the surface ozone values (measured directly from the aircraft) and the deposition velocity for ozone (estimated from the literature). For the top part of the stable boundary layer, the flux of O_x can be interpreted as an eddy diffusivity (K_z) multiplied by the gradient of O_x between the stable boundary layer and residual layer. A linear regression is used to determine the O_x gradient ($\partial[O_x]/\partial z$) in the layer of air that appeared to have the strongest O_x gradient, which tended to be 200 m thick and span from the middle of the NBL to the bottom of the RL. The eddy diffusivity can now be solved for with all of the other terms estimated.

Results of the overnight mixing budgeting technique demonstrated here are presented in Table 4. An error propagation analysis is presented for each term in the budget, as well as for the ultimately calculated K_z values. Of note is the fact that on average the chemical loss (-1.8 ppb/hr) is about twice as large as the physical/chemical loss from dry deposition (-0.8 ppb/hr). Another way to frame that is as competing timescales of ozone loss in the NBL: for dry deposition the average lifetime of ozone is 42 hr (300 m/0.002 m/s), and for chemical loss it is 19 hr (subject to the considerable uncertainty based on the ultimate fate of the nitrate radical outlined above.) Further, both losses of O_x added together are about double the observed time rate of change. In other words, the physical and chemical losses are partially compensated by vertical mixing. Because the residual layer consistently contains more ozone than the stable NBL, turbulent mixing will result in a transfer of ozone into the NBL. While NO_2 is observed to be higher in the NBL than in the RL (by about 3-5 ppbv), it is a much smaller contribution to the O_x (O_3 is less by anywhere from 10-20 ppbv.) Thus, vertical mixing at the top of the stable boundary layer, enhanced by the low-level jet, is inherently a source term.

Estimates of the measurement error for each of the budget terms and then the consequent error in the diffusivity values are presented in the parentheses of Table 4. The storage term error is computed by first taking the standard deviation of 1-second ozone measurements in each 20-m bin space, divided by the square root of the number of samples, then the

standard error of the means for both the late night and sunrise profiles are combined. The advection term error is computed from the standard error of the slopes of the regression fits, with errors propagating for each of the 4 advection components for both the u and v components of wind. To compute the chemical loss error, the large uncertainty of the α coefficient of Equation 7 must be taken into consideration. Based on our analysis, we assume that α is between 0 and 2 because those relevant channels of nitrate loss at night (R5 & R6) likely outcompete (R4). The uncertainty of the lifetime of NO_3 for each channel is assumed to be on the order of ~4 s, and so despite our assumption that both channels have equivalent rates, a reasonable error in each channel would lead to one channel being about 3 times as fast as the other. This leads to standard error estimate for the α coefficient to be about 0.5. An error propagation is then carried out for each 20 m bin, using the standard deviations of the O_3 and NO_2 measurements divided by the square root of the sample size. As previously stated, the estimated standard errors of the stable boundary layer height and surface deposition of ozone are 100 m and 0.1 cm/s, respectively. The surface ozone standard error is computed as the standard deviation of the aircraft measurements divided by the square root of the sample size, and the vertical O_x gradient uncertainty is computed by the standard error of the regression slope. The uncertainties in the vertical mixing, deposition, and diffusivity values can then be computed by standard error propagation. The relative errors are estimated to be about 50%.

Table 4. Results from the nocturnal scalar budget of odd oxygen (O_3+NO_2) for each of the midnight/sunrise flight pairs. Estimated errors in each are presented in parentheses.

Overnight Flight Date	Storage	Advection	Chemical Loss	Vertical Mixing	Deposition	Eddy Diffusivity
	ppb/hr	ppb/hr	ppb/hr	ppb/hr	ppb/hr	m^2/s
9/11/2015	-2.3 (0.2)	-3.2 (0.2)	-2.4 (1.3)	3.8 (2.1)	0.5 (0.3)	2.6 (1.2)
9/12/2015	-0.3 (0.1)	-0.0 (0.1)	-1.9 (0.9)	2.2 (1.5)	0.6 (0.4)	2.8 (1.5)
6/3/2016	-0.7 (0.1)	0.3 (0.2)	-1.0 (0.4)	1.0 (0.8)	1.0 (0.6)	1.4 (1.0)
6/4/2016	-0.5 (0.2)	-0.6 (0.1)	-1.3(0.6)	2.6 (1.6)	1.2 (0.8)	0.7 (0.3)
6/29/2016	-1.4 (0.2)	-1.0 (0.1)	-1.5 (0.7)	2.2 (1.6)	1.2 (0.8)	1.6 (0.8)
7/25/2016	-0.9 (0.1)	0.6 (0.2)	-1.8 (0.8)	0.9 (0.9)	0.7 (0.4)	0.9 (0.8)
7/26/2016	-1.4 (0.2)	0.2 (0.2)	-1.5 (0.8)	0.6 (1.0)	0.7 (0.4)	0.6 (1.0)
8/13/2016	-1.5 (0.1)	-0.3 (0.2)	-2.3 (1.1)	1.9 (1.4)	0.8 (0.5)	2.1 (1.5)
8/15/2016	-1.1 (0.1)	0.6 (0.2)	-1.7 (0.9)	1.0 (1.1)	0.9 (0.6)	0.7 (0.7)
8/16/2016	-1.8 (0.1)	-0.1 (0.1)	-2.1 (1.1)	0.9 (1.2)	0.5 (0.3)	1.9 (2.5)
8/17/2016	-1.8 (0.1)	0.1 (0.1)	-2.4 (1.4)	1.1 (1.5)	0.6 (0.4)	0.8 (1.0)
8/18/2016	-1.7 (0.2)	0.5 (0.2)	-2.1 (1.2)	0.7 (1.3)	0.8 (0.5)	0.7 (1.3)
Average	**-1.28**	**-0.24**	**-1.83**	**1.59**	**0.80**	**1.41**
Standard Dev.	**0.57**	**1.01**	**0.44**	**0.93**	**0.24**	**0.77**

This method of indirectly estimating turbulence differs from some other attempts that have been made for stably stratified environments. *Clayson and Kantha* [2008] applied a technique used in the oceans to the free troposphere and lower stratosphere, where turbulence is sparse and intermittent, much like the stable NBL. The method involves using high-resolution soundings to estimate a length scales of eddies which can subsequently be used to obtain estimates of eddy diffusivity. This is done by relating the eddy scale to the Ozmidov scale, where if the Brunt-Vaisala frequency (N) is known, TKE dissipation can

be estimated. Eddy diffusivity is then estimated as a ratio of the TKE dissipation and N^2, and were found to range from 1-10 m^2/s in the troposphere falling off to <0.1 m^2/s in the stratosphere where the stability increases significantly. It should be noted that the stabilities observed in the SJV NBL's ($N \sim 0.023\ s^{-1}$) are about twice as large as typical free troposphere values, and are more similar to the stability found in the lower stratosphere. *Wilson* [2004] reviewed other literature on radar-based estimates of eddy diffusivity in the free troposphere and lower stratosphere, and found a general range of estimates from 0.02 – 3.0 m^2/s. *Rao et al.* [2001] report a range of 0.05 to 1.8 m^2/s throughout the troposphere. It is therefore believed that the eddy diffusivities observed in this project are relatively large given the strong stable stratification of the NBL, and are likely enhanced by the low-level jet, particularly around its peak strength near midnight.

With the diffusion of scalars due to eddies being a direct consequence of turbulent kinetic energy, it may be hypothesized that the derived K_z values should have a relationship with estimated TKE. While estimates of σ_w depend on convective similarity, which is not applicable at night, the horizontal wind variance ($=\sigma_u^2+\sigma_v^2$) can be analyzed for the night and sunrise flight data. Of the 12 nights included in this analysis, 11 had enough wind data within the stable boundary layer for a sufficient average horizontal wind variance estimation. The results of this are shown in Figure 22.

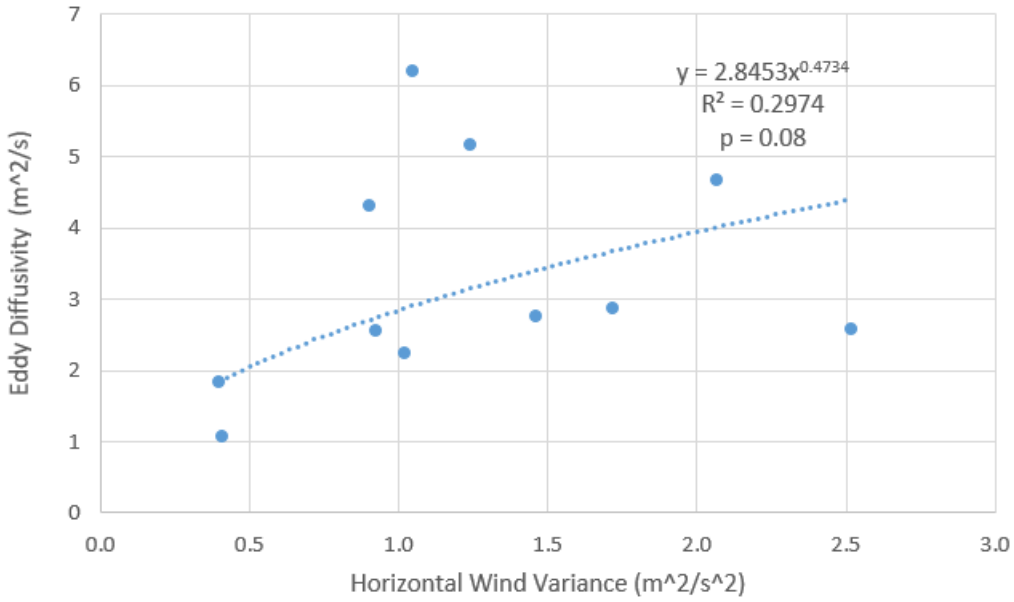

Figure 22. Estimated eddy diffusivity values as a function of the observed horizontal wind variance.

While this result is only marginally statistically significant, it is worth analyzing the fit for any physical meaning. One way of thinking about the turbulent eddies under stable stratification is by the buoyancy length scale, which is an order of magnitude estimate of the largest possible eddy size that can survive in the face of buoyancy destruction [*Stull*, 1988]:

$$\ell_b = \frac{\sigma_w}{\sqrt{\frac{g}{\theta}\frac{d\theta}{dz}}} \tag{11}$$

Where the denominator of Equation 11 is the Brunt-Vaisala frequency, *N*. Here, we speculate that eddy diffusivity can be estimated as the product of a length scale and a velocity scale:

$$K_z \sim \ell_b * TKE^{1/2} \tag{12}$$

It is first worth noting that the power of the fit in Figure 22 is very close to 0.5, which would be predicted by this relationship. A quantitative analysis carried out of the vertical temperature gradients in the stable boundary layers reveals an average Brunt-Vaisala frequency of 0.023 s^{-1} (Table 3). This would imply an average σ_w of 0.07 m/s. While there are no measurements of vertical velocity variance during our overnight and sunrise flights, *Mahrt* [2010] analyzed several cases of stable boundary layer turbulence in diverse environments, and found values of σ_w ranged from 0.05 to 0.09 m/s.

The physical significance of mixing overnight in relation to the air pollution problem remains somewhat of an open question. However, we hypothesize that when more ozone from the residual layer is mixed downward into the NBL, more of the ozone reservoir is subject to depletion due to dry deposition (chemical loss in the RL and NBL should proceed at similar rates unless greater NO near the surface returns nitrate to NO_2 via (R6) shutting off the O_x loss entirely as discussed previously.) Greater coupling between the two layers then could reduce the amount stored in the RL reservoir rendering cleaner air the following day. The relationship between the eddy diffusivity values found in this study and sunrise surface ozone is analyzed, and serves as both an additional check on the validity of the calculated K_z values as well as a test of this proposed hypothesis. Figure 23 shows the results, which are significant and in the predicted direction, with lower ozone at sunrise being observed in the presence of stronger mixing.

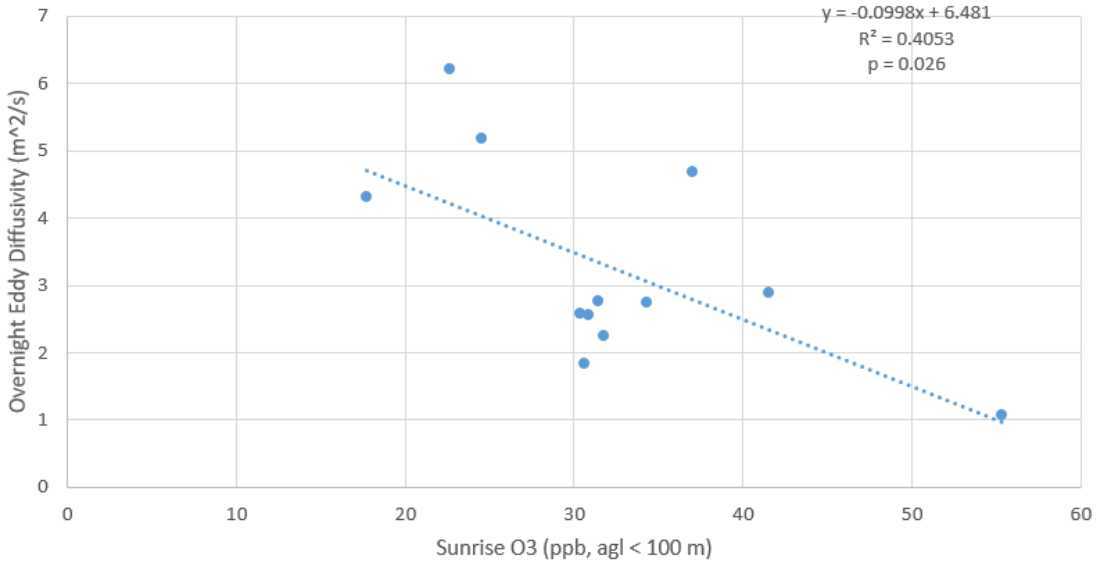

Figure 23. Correlation between derived overnight eddy diffusivity and the sunrise ozone concentration near the surface.

The Fresno Eddy

One complicating factor that remains for this particular analysis is the presence of the aforementioned Fresno Eddy (Figure 24) and its influence on our measurements of advection. The recirculation effects from the presence of an eddy may effectively "wash out" any advection measured on an individual flight, with the flight path restricted to either side of the eddy. An analysis from 915 MHz sounder data presented in [*Zhong et al.*, 2004] reveals a pattern regarding the evolution of the eddy. At night, the northerly low level jet is formed in the SJV (Figure 25), and a weak southerly return flow is observed in the foothills to the east. The eddy drifts to the west overnight, and as it does so, the northerly branch weakens and the southerly branch strengthens. By daybreak, the eddy appears to deform and disintegrate with much of the SSJV experiencing a strong southerly wind. In our flight data we observe a consistent and strong southerly flow near sunrise, especially away from the Tehachapi pass (Figure 26), though we remind the reader that these flights specifically targeted high ozone events so they may be subject to a meteorological bias. In fact, the southerly winds aloft on the sunrise flights had comparable magnitudes to that of the nocturnal jet. It is thus likely that our dataset captures the bulk of the dominant flow (and thus advection) on both the late night and sunrise flights, which are averaged and interpolated. It is noted that the average advection term for the 12 nights presented is -0.24 ppb/h, which is an order of magnitude smaller than the chemical loss and storage terms. The small average contribution from advection is consistent with previous findings from daytime scalar budgets performed over the oceans [*Conley et al.*, 2011; *Faloona et al.*, 2009], and is what would be expected in the presence of a recirculating eddy. Lastly, it is noted that individually adjusting each flight to have an advection term of zero (to assume full recirculation effects) results in little change to the calculated diffusivity values (7% change, r^2=0.75, p=0.0003).

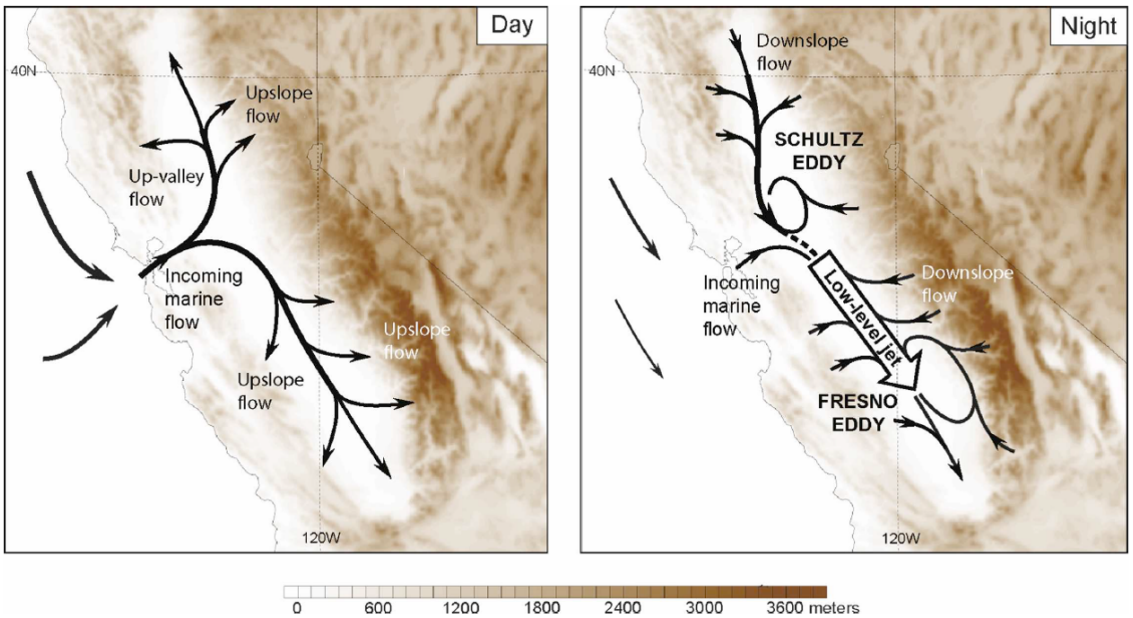

Figure 24. Cartoon schematic of California's Central Valley fair-weather wind patterns including the LLJ associated with the Fresno Eddy. Figure from Bao et al. (2008).

To show the portions of the Fresno eddy being captured by our flight data, Figure 25 & Figure 26 present an analysis of the wind consistency, defined as the ratio of the vector-averaged wind speed to the magnitude-averaged wind speed. Values close to 1 indicate a consistent wind direction as seen in the nocturnal jet.

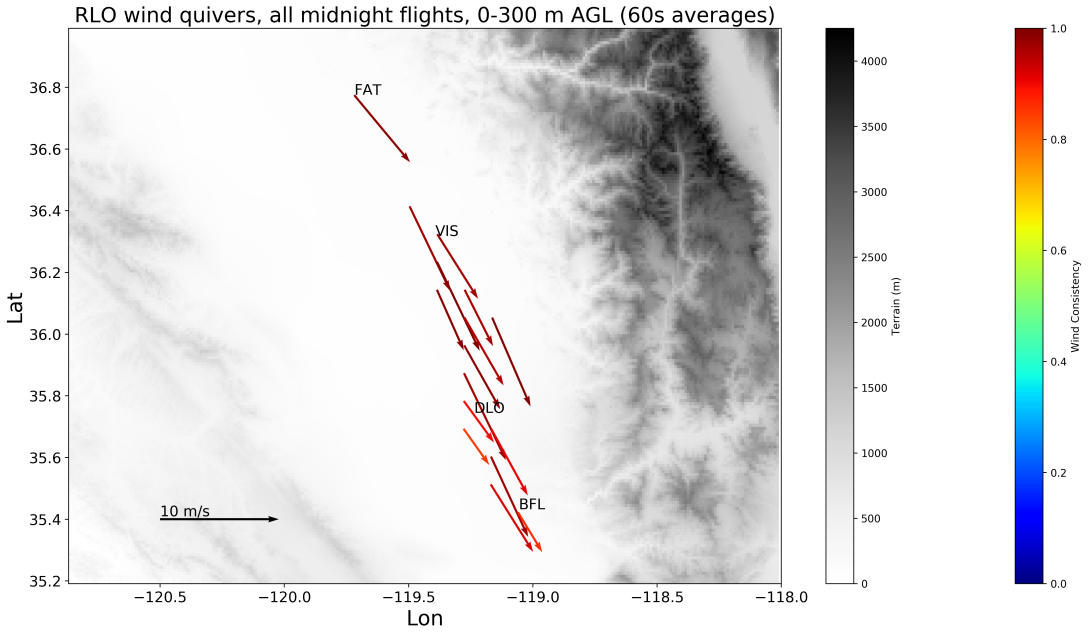

Figure 25. Wind consistency and direction in the lowest 300 m for all the midnight flights.

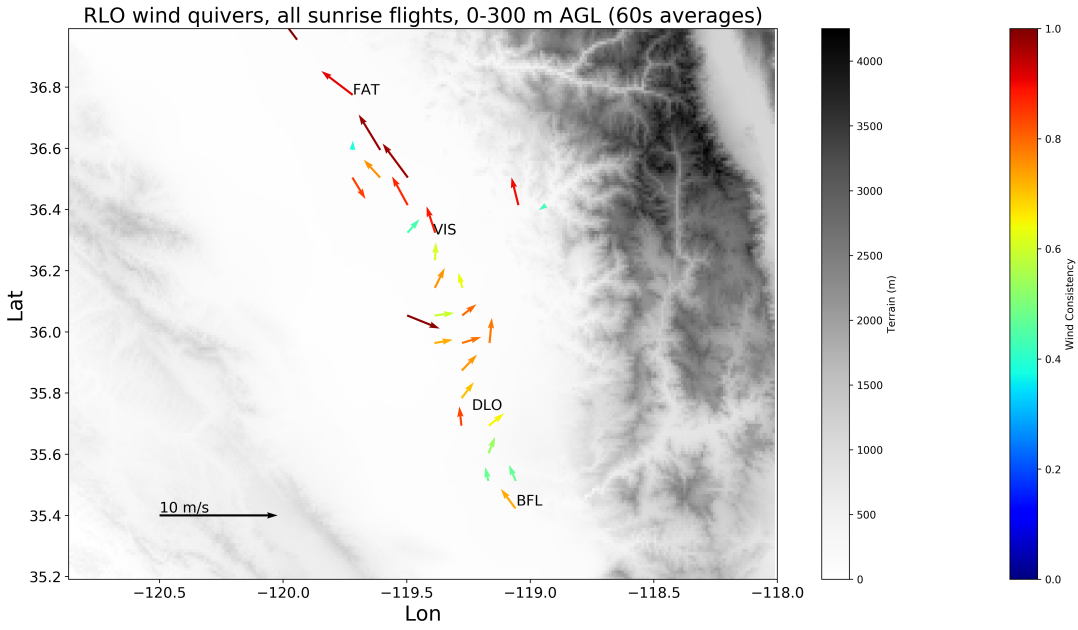

Figure 26. Wind consistency and direction in lowest 300 m during sunrise flights.

The Low-Level Jet

Six years of data was analyzed for Visalia, CA, utilizing the 915 MHz sounder to obtain low level jet speed, along with the surface air quality network, was used to obtain the maximum 1-hour ozone observed the following day. The results are shown in Figure 28. It can be seen that a stronger nocturnal low-level jet is correlated, albeit weakly, with cleaner air the following day (r^2=0.14, p<0.00001). This is in line with our hypothesis that the low level jet will lead to stronger mixing, which leads to more residual layer ozone

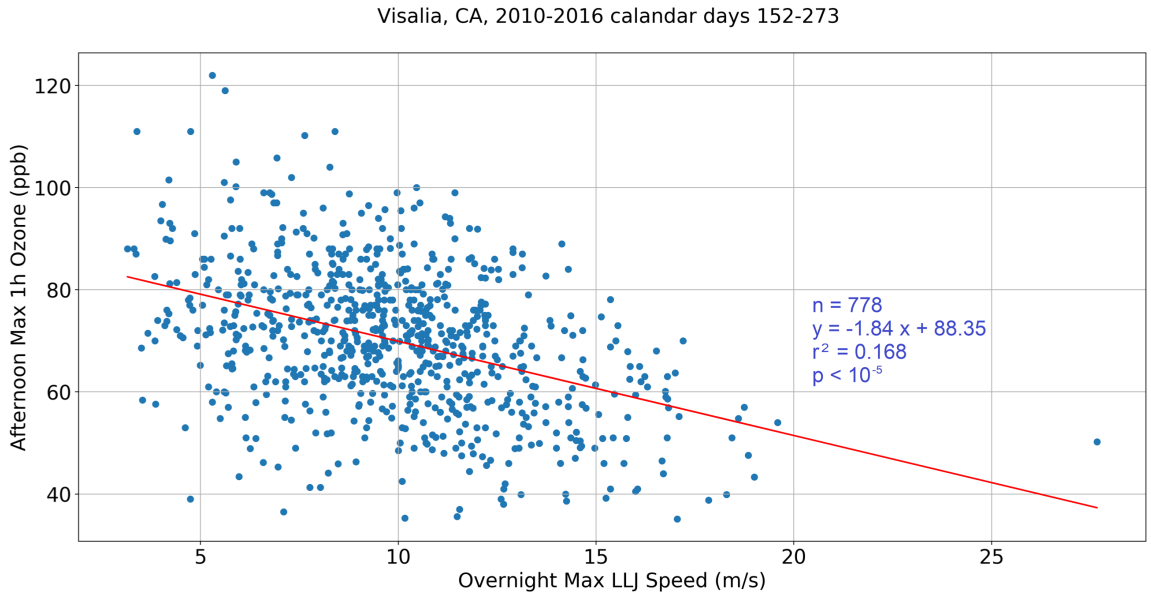

Figure 28. Correlation between nocturnal low level jet wind speed and the following day's maximum 1hr ozone concentration in Visalia, CA during 7 summers.

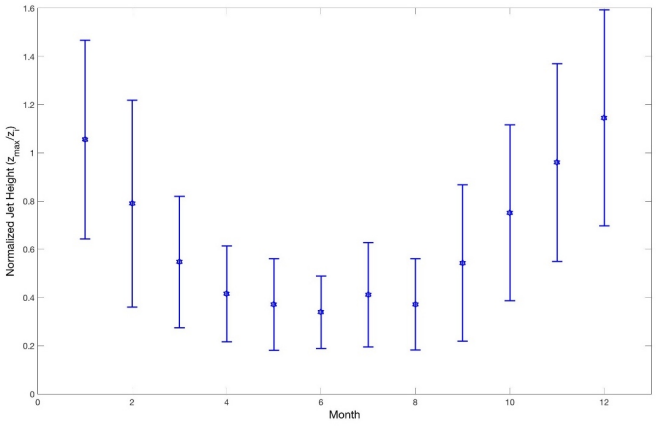

Figure 27. Climatology of the low-level jet height in the San Joaquin Valley normalized by the daytime ABL height.

depletion. Lastly, we present an analysis of the non-dimensional jet height climatology. It is seen that the jet is significantly lower during the summer. The cause of this is an active area of investigation, but it is speculated that this is due to stronger subsidence in the summer due to the prominent influence of the Pacific High and the stronger thermal forcing of the valley-mountain circulation. Another look at the overnight layering, including the low level jet, is presented in the average scalar profiles for all midnight flights of Figure 29. An average low-level jet height of between 200-400 m is seen, which corresponds approximately with the average observed stable NBL depth. Likely due to the shear

induced by the LLJ, turbulence is seen to be very vigorous at night with similar values of TKE as observed during the daytime (Figure 3) during convective conditions although estimates of TKE may be influenced by buoyancy wave activity in the NBL.

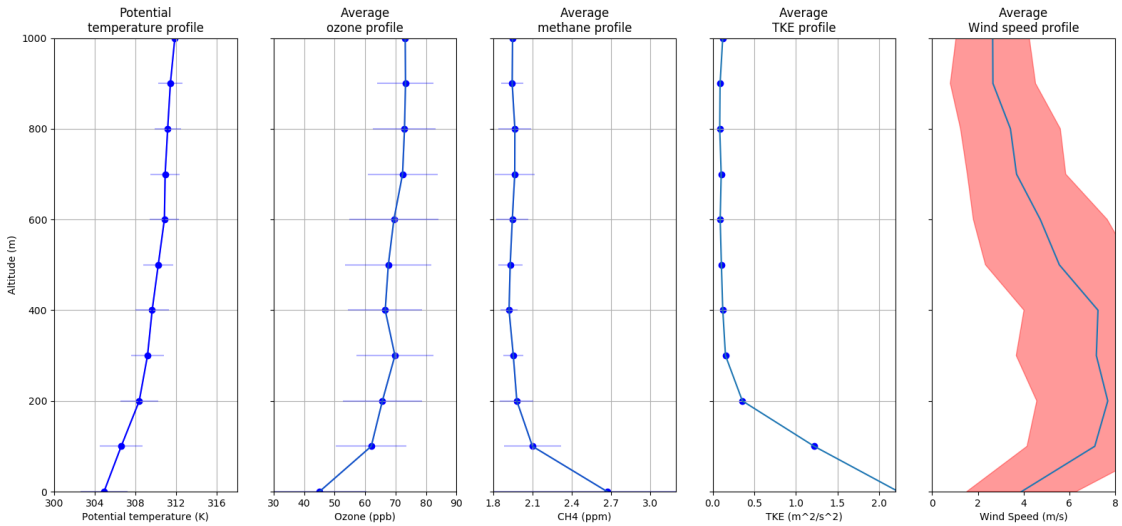

Figure 29. Averaged profiles of potential temperature, ozone, methane, TKE, and wind speed from all of the midnight flights.

Daytime ABL, Turbulence, and Entrainment

Generally speaking, entrainment is the mixing between a turbulent fluid and a non-turbulent one. Entrainment mixing occurs during the daytime in the lowest portion of the troposphere at the top of the ABL. Understanding the ABL and its dynamics are of paramount importance to: air quality studies, ABL parameterizations for numerical modeling, and satellite retrievals of atmospheric data. The entrainment rate, which is used to parameterize the entrainment process, cannot be directly measured [*Lenschow et al.*, 1999]. In some applications the entrainment velocity is often taken to be equivalent to the ABL growth rate [*Tennekes*, 1973] in the absence of a mean vertical wind, often called subsidence denoting descending air parcels. Several processes resist entrainment as it works to grow the ABL raising its height. One is low-level divergence accompanied by subsidence at the level of the temperature inversion, and any slope in that inversion level coupled with a mean horizontal wind leading to advection at any particular point. Subsidence is also the result of larger scale synoptic features, like ridges and troughs, not just mesoscale flows and return circulations. Studies of entrainment, the entrainment rate, and the structure of the entrainment zone have been conducted utilizing: laboratory convection tank experiments, aircraft in-situ data, numerical modelling, and remote sensing techniques (using sodar, radar, and lidar). This is often used in practice when high frequency data is taken enabling turbulent fluxes to be measured. In the absence of high frequency data, entrainment can be taken simply as the difference between the ABL growth rate and the local subsidence rate. Entrainment is almost always parameterized in chemical transport models, most finer resolution regional models, and climate models because the process is sub-grid and restricted in the vertical dimension to the region near the capping inversion at the top of the ABL.

The dry or clear air ABL (often referred to as a convective boundary layer) is primarily driven by buoyancy fluxes emitted from the surface but vertical wind shear can also play a role in enhancements to the ABL structure and growth to a varying degree [*Fedorovich and Conzemius*, 2008]. Far fewer studies have been done on the ABL accounting for the effects from shear than considering only the shear-free convective ABL. Therefore, more studies need to be completed spanning a variety of atmospheric conditions. Shear can alter the structure of turbulence and the mean flow within the ABL, but it also may crucially influence the entrainment zone dynamics and enhance ABL growth and entrainment fluxes. The shear generated TKE in the lower layers of the ABL can indirectly make similar impacts by slowing the mean flow of the ABL thereby enhancing the shear at the top of the ABL.

In the atmosphere above the SJV we envision a three-layer system: the ABL, the FT and a transition zone we are referring to as the "buffer layer" between the two ranging somewhere between ~700 m and 2000 m (AGL). This conception of an intermediate region in mountainous terrain was also conceived of by *Henne et al.* [2004], there called an "injection layer." For that study, the injection layer is the zone which is the depository of pollutants from the ABL being vented along the sidewalls of deep Alpine valleys. For their model though the sidewalls are both approximately equal in height, while in the Central Valley the Sierras are approximately three times taller than the Coast Ranges (see Figure 18). This process of venting has been simulated and observed to elevate pollution above the ABL along the slopes of the Sierra Nevada in the Central Valley of California during the day with the possibility of being mixed down into the growing ABL on the next day [*Fast et al.*, 2012]. The predominant synoptic flow at the 700mb pressure level above the Central Valley out of the southwest impinges against the Sierra Nevada and stagnates, because the horizontal momentum is not great enough to overcome the vertical stability there and continue its path over the mountains. This happens when the Froude number is much less than unity, and the flow will begin to turn towards the north due to a weakened Coriolis force (and a prevailing pressure gradient force). An additional source of pollution to the buffer layer may come from long range transport over the pacific and end up in the buffer layer as well (the main subject of the CABOTS project.)

A compilation of the midday airborne observations of the ABL dynamics are presented in Table 5. The EPA flights, which were four hours in duration and limited to the region between Fresno and Visalia, are included for comparison. In general, the EPA flights should yield better results because they were longer and more targeted for achieving a complete midday budget of the scalars. Nevertheless, we performed the same analysis on the midday RLO flights and there do appear to be significant differences between the two domains in an average sense. For example, the entrainment rates for the entire region down to the end of the SJV at Bakersfield are nearly twice as large as those around Fresno. This is an interesting finding and one that is consistent with generally deeper boundary layers found in the southern end of the SJV as pointed out in previous studies [*Bianco et al.*, 2011; *Trousdell et al.*, 2016].

Table 5. WRF model subsidence, ABL growth, advection, and entrainment rates along with meteorological flight data.

Flight Date	WRF W(z_i) (cm/s)	ABL Growth dzi/dt (cm/s)	z_i Advection (cm/s)	Entrainment w_e (cm/s)	ABL Depth z_i (m)	Potential Temperature (K)	ABL Wind Speed (m/s)
EPA Flights							
7/27/16	-0.31	2.81	0.59	3.72	613	310.9	2.9
7/28/16	-0.37	3.62	0.11	4.10	622	310.6	3.5
7/29/16	-1.23	0.81	-0.12	1.91	602	311.4	3.1
8/4/16	-1.57	1.13	0.89	3.59	740	306.9	2.4
8/5/16	-1.50	0.51	-0.14	1.86	606	302.8	2.9
8/6/16	-1.65	-1.01	0.44	1.08	660	304.7	1.9
EPA Averages	**-1.1**	**1.3**	**0.3**	**2.7**	**640**	**307.9**	**2.8**
RLO Flights							
Deployment 1							
9/10/15	-1.62	1.60	2.70	5.92	833	310.2	NA
9/11/15	-1.17	3.90	-1.16	3.91	570	309.2	2.3
9/12/15	-1.58	1.07	0.61	3.26	608	308.6	NA
Deployment 2							
6/2/16	-1.36	4.42	-0.12	5.66	700	309.0	3.3
6/3/16	-1.95	3.92	1.37	7.24	820	308.5	3.4
6/4/16	-1.36	3.82	0.54	5.71	700	310.7	2.5
Deployment 3							
7/24/16	-2.54	0.46	0.14	3.14	642	310.3	1.9
7/25/16	-3.22	2.35	-0.08	5.49	681	309.8	2.9
7/26/16	-2.48	3.51	2.01	8.00	730	309.8	2.6
Deployment 4/5							
8/12/16	-2.11	2.44	0.60	5.15	750	307.1	2.7
8/13/16	-1.88	2.58	-2.84	1.62	942	308.9	NA
8/14/16	-2.04	1.93	0.25	4.22	625	310.4	2.9
8/15/16	-2.61	1.76	0.13	4.50	733	308.7	3.3
8/16/16	-2.44	2.87	0.12	5.43	760	308.5	2.8
8/17/16	-2.90	3.37	0.52	6.79	767	309.8	2.4
RLO Averages	**-2.1**	**2.7**	**0.3**	**5.1**	**724**	**309.3**	**2.8**

Turbulence Measurements

The low-cost wind system on the aircraft [*Conley et al.*, 2014] measures horizontal winds at a frequency of 1 Hz. While this frequency is not high enough to capture the full spectrum of turbulence, we can check its ability to detect an inertial subrange and estimate the amount of horizontal wind variance not being resolved by extrapolating Kolmogorov's 5/3 slope. After accounting for this underestimate of wind variance, we can apply convective similarity theory to estimate the convective velocity (w_*), the surface heat flux (Q_0), and the total turbulent kinetic energy (TKE) for all the daytime flight data. To our knowledge, this is the first such attempt to estimate turbulence parameters from this low-cost wind measurement system.

Within the boundary layer, large swirls of air known as turbulent eddies are generated by either convective buoyancy forces and/or wind shear. These large eddies then act to

produce more localized wind shearing, which creates smaller eddies. This so-called energy cascade of eddy size continues to smaller and smaller scales until the eddies are small enough to be lost to molecular viscosity. In any given scalar signal that is being advected by a turbulent fluid, it is possible to map out the energy contained in any given eddy size by taking a Fourier transform of the signal. In doing so, the largest eddies will have the most (kinetic) energy, and the smallest eddies will have the least. The eddy size range where the turbulent motion is too small to be influenced by the effects of the initial energy generating mechanism, but too large to be influenced by the effects of molecular viscosity, is known as the inertial subrange. A well-established theory, known as the Kolmogorov Scaling Law, states that the inertial subrange of turbulence plotted on a log(S)-log(f) plot should contain a slope of -5/3. This is a common check to determine whether a wind instrument is capturing the effects of turbulence. In mathematical form, the scaling law is as follows:

$$S = \alpha_k \varepsilon^{2/3} f^{-5/3} \tag{13}$$

Where S is the power spectral density (the energy contained at each given eddy size), ε is the dissipation rate of turbulence, and α_k is the Kolmogorov constant.

In order to check that our wind data fits this law, 300-second periods are taken from the data set where the flight path was entirely inside the boundary layer. The power spectra of 77 300-second samples were taken individually, then averaged together. The result is shown in Figure 30, which is consistent with the known Kolmogorov Scaling Law. Furthermore, seeing that the energy at any given frequency is proportional to the variance

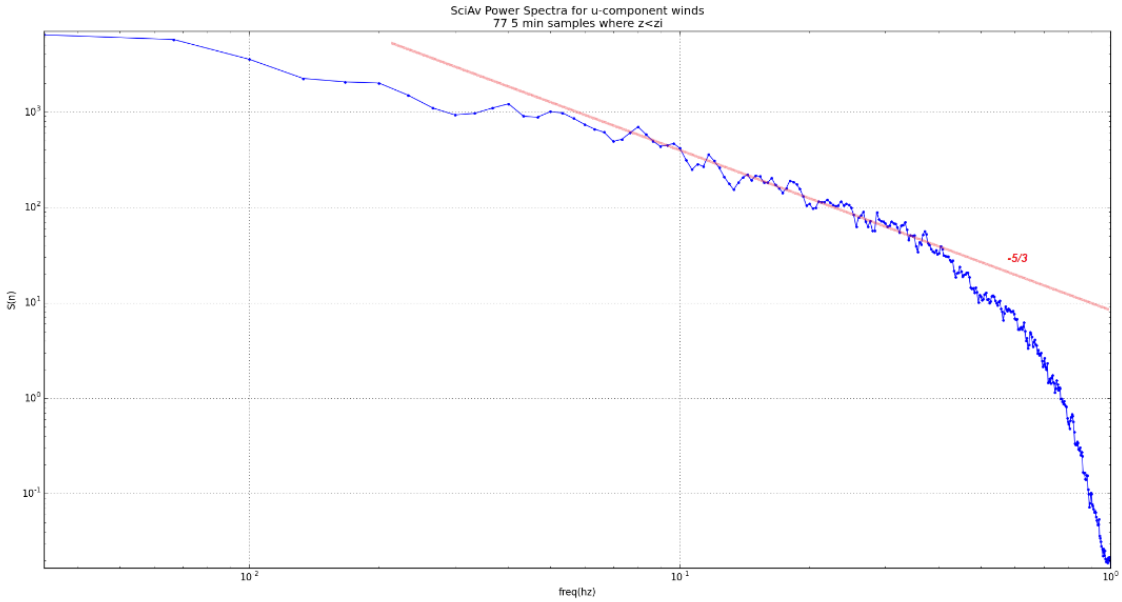

Figure 30. Power spectrum of the horizontal ABL winds observed during midday flights.

that frequency contributes to the signal, the total variance of the signal can be obtained by integrating the power spectral function. To obtain a curve whose area visually represents the its integral, we plot $S{\cdot}f$ on the y-axis and ln(f) on the x-axis. This is shown in Figure 31, which allows us to estimate that the total amount of variance missing from what we are

able to capture is approximately 19%. This is used to correct subsequently presented estimates of turbulence.

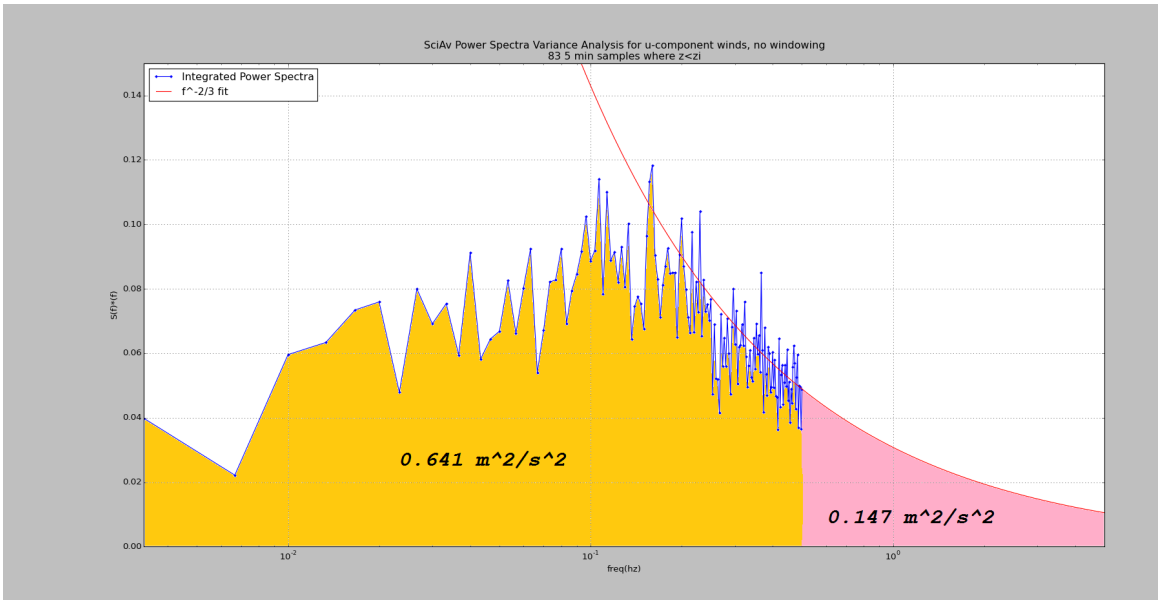

Figure 31. Visual representation of the estimated wind variance not resolved by the airborne wind measurement.

As previously mentioned, the aircraft can only measure horizontal winds, making further assumptions necessary to obtain full 3D turbulence estimates. Fortunately, there are a few relationships for the convective mixed layer that have been derived using similarity theory, later to be empirically formulated using aircraft observations. In the daytime under fair weather conditions, convective thermals traverse the depth of the ABL, z_i. Seeing that these thermals are generated by heating at the surface, it is logical to assume that their forcing will be proportional to the surface heat flux, Q_0. Thus, it is possible to define a convective velocity scale, w_*, which is a common scaling variable and can be considered a typical thermal updraft or downdraft speed [*Stull*, 1988]:

$$w_* = (Q_0 z_i \frac{g}{\theta_v})^{1/3} \tag{14}$$

Aircraft observations show that this convective velocity scale can be decently related to horizontal wind variance [*Caughey and Palmer*, 1979; *Panofsky et al.*, 1977]:

$$\sigma_u^2 \sim \sigma_v^2 \sim 0.35 w_*^2 \tag{15}$$

Treating this approximation as an equation, adding them, and solving for w_* results in:

$$w_* = \sqrt{\frac{\sigma_u^2 + \sigma_v^2}{0.7}} \tag{16}$$

σ_u and σ_v are known from our aircraft data, which allows us to make estimates of the convective velocity scale. A more direct measure of turbulence is the turbulent kinetic energy (TKE) formally defined as:

$$TKE = \frac{1}{2}(\sigma_u^2 + \sigma_v^2 + \sigma_w^2) \tag{17}$$

Since σ_w cannot be directly measured from the aircraft wind system, another convective similarity relation is employed [*Lenschow et al.*, 1980] and rearranged to solve for σ_w^2:

$$\sigma_w^2 = w_*^2 * 1.8\left(\frac{z}{z_i}\right)^{\frac{2}{3}} * (1 - 0.8\left(\frac{z}{z_i}\right))^2 \tag{18}$$

Combining equations (16) through (18) allows us to estimate the total TKE in the convective ABL:

$$TKE = \frac{1}{2}\left[\sigma_u^2 + \sigma_v^2 + \left(1.8\left(\frac{z}{z_i}\right)^{\frac{2}{3}} * \left(1 - 0.8\left(\frac{z}{z_i}\right)\right)^2 * \frac{\sigma_u^2+\sigma_v^2}{0.7}\right)\right] \tag{19}$$

This method requires estimates of the boundary layer height, z_i, and of course our flight strategy includes repetitive penetrations of the interface between the ABL and buffer layer on each flight. Measurements of boundary layer heights were inspected from profiles of potential temperature, water vapor, and methane during these penetrations. Every identifiable boundary layer top was marked along with an associated time of day and latitude. Then, a multiple linear regression was used for every flight to fit z_i as a function of time and latitude. The latitude dependence was generally observed with a deeper boundary layer tilted toward the southern end of the San Joaquin Valley. 21 mid-afternoon flights from this field campaign with a fully developed fair weather boundary layer were included in this analysis (Table 5). Now armed with observations of z_i, it is possible to estimate the surface heat flux, Q_0, by rearranging equation (14):

$$Q_0 = \frac{w_*^3 \theta_v}{z_i g} \tag{20}$$

When determining values for σ_u and σ_v, it is important to use long enough data samples such that all of the wind variance measured by the aircraft system, represented by the orange area in Figure 31, is captured. In order to test this, calculations for flight-average w_* and Q_0 are made with varying sampling times for σ_u and σ_v. It is expected that the calculated values of Q_0 and w_* will be smallest when using low sampling times, as the σ inputs can only capture the wind variance of the smallest eddies. As the sampling time increases, we would like to see a 'leveling off' of the calculated average turbulence parameters, corresponding to a "mesoscale gap" where all boundary layer eddy sizes being included in the sample with minimal inputs from larger scale circulation patterns.

Figure 32 shows the results for w_* as a function of sampling interval length. These results are corrected for the 19% of variance missing from the high frequency end of the power

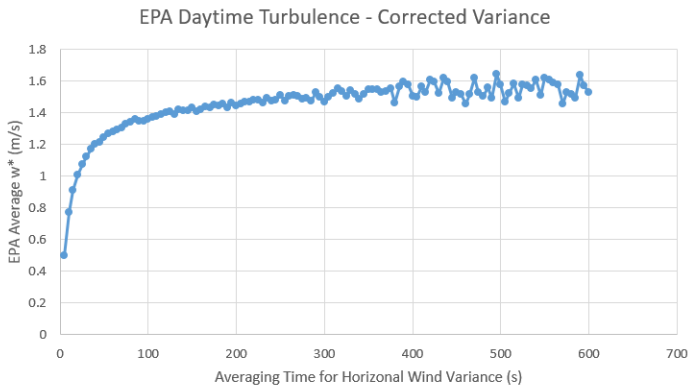

Figure 32. Convective velocity scale estimates as a function of the averaging time interval.

spectra. It appears that the values approach a reasonable limit by a sampling time of 300 seconds. A budget analysis for enthalpy (heat) from the EPA flights estimates an average convective velocity of 1.48 m/s, and an average heat flux of 0.17 K m/s (200 Wm^{-2}). The estimates from this independent method agrees fairly well with the convective velocity of asymptote of Figure 32.

Table 6. Results of the daytime turbulence analysis for the EPA flights.

Date	TKE (m^2/s^2)	w* (m/s)	Q0 (k m/s)
7/27/2017	1.02	1.39	0.21
7/28/2017	1.08	1.46	0.21
7/29/2017	0.92	1.31	0.14
8/4/2017	1.30	1.57	0.24
8/5/2017	1.16	1.47	0.16
8/6/2017	1.42	1.62	0.24
Average	**1.15**	**1.47**	**0.20**
Standard Dev.	**0.17**	**0.10**	**0.04**

Table 6 & Table 7 present additional results for the daytime turbulence parameters for each of the EPA flights. While no formal error propagation analysis has been carried out to date, the estimated parameters are overall very consistent between flights, which is to be expected given the similar environments they were conducted in. Comparisons with WRF surface heat fluxes also shows that the variability observed does correlate well with the model's variability. This is an encouraging result, as confidence in this low-cost paradigm to estimate turbulence is increased with these preliminary findings. Other analyses from this field campaign have shown that entrainment between the polluted boundary layer and the less polluted buffer layer plays a significant role in the local daytime pollutant concentration build-up.

Table 7. Results of the turbulence analysis from the midday RLO flights.

Fight #	TKE (m^2/s^2)	w* (m/s)	Q0 (k m/s)
7	1.67	1.70	0.31
15	0.85	1.25	0.13
19	1.62	1.73	0.24
23	2.00	1.88	0.29
31	1.32	1.58	0.20
35	1.70	1.80	0.31
39	1.04	1.44	0.17
44	0.84	1.19	0.11
48	1.17	1.42	0.15
50	1.31	1.52	0.15
54	0.84	1.29	0.11
58	1.07	1.43	0.14
62	1.12	1.40	0.16
66	2.04	1.91	0.34
Average	**1.33**	**1.54**	**0.20**
Standard Dev.	**0.40**	**0.23**	**0.08**

A Composite of all the heat flux estimates from all afternoon flights are presented in to see if spatial patterns emerge Figure 33. As a general trend, greater heat fluxes are observed over the areas of Fresno and Bakersfield, which is aligned with expectations of urban heating effects. Moreover, there seem to be high spatial variability out over the agricultural regions of the domain which could result from the mottled land surface properties of albedo and soil moisture which will strongly affect the surface heat fluxes.

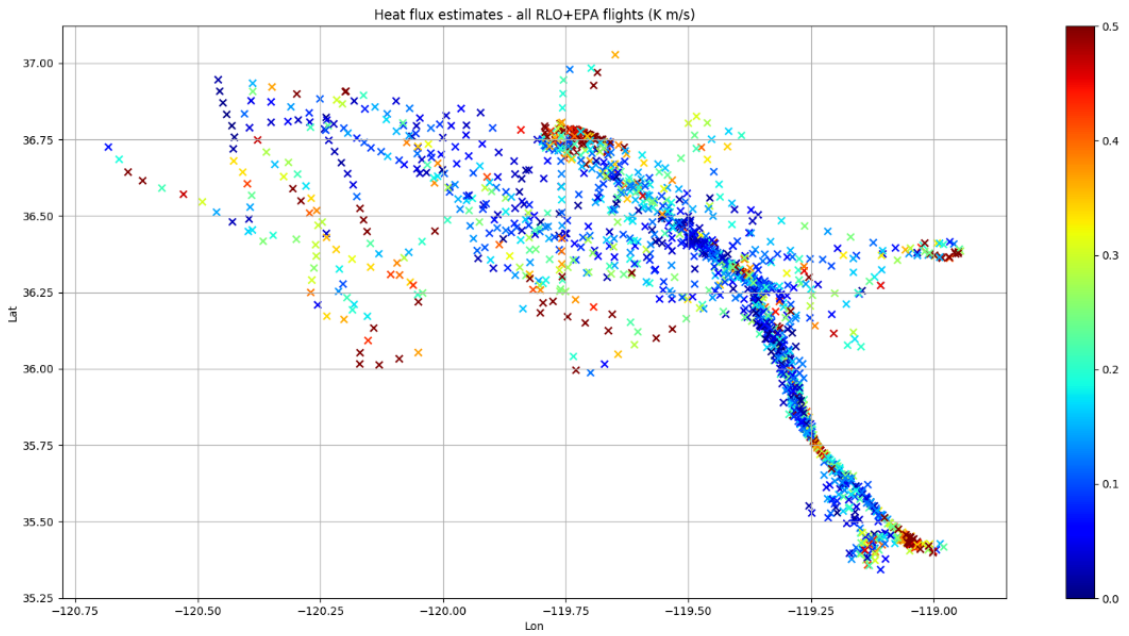

Figure 33. All estimates of surface kinematic heat fluxes (K m/s) from all afternoon flights.

Entrainment, its Efficiency, and its Dependence on Wind Speed

Researchers have often suggested an inverse relationship in the literature between the entrainment rate (w_e), often non-dimensionalized by the convective velocity scale (w_*), and a convective Richardson number, a non-dimensional ratio of the potential energy of the capping inversion to the kinetic energy of convective eddies, using a two layer slab model [*Sullivan et al.*, 1998; *Sun and Wang*, 2008]. For our purposes we constructed a bulk Richardson number (Ri) using the potential temperature gradient above the entrainment zone (γ_θ, in the buffer layer) instead of the potential temperature jump across it. We further use the average wind speed within 100 m of the inversion height (U_{zi}), and thus a total 200 m assumed entrainment zone thickness (Δh). The convective velocity scale used here was obtained from the EPA flight data set using predicted surface sensible heat fluxes from the enthalpy budgeting technique (not the turbulence of the previous section.)

$$Ri = \frac{g\gamma_\theta \Delta h^2}{\theta_{zi} U_{z_i}^2} \tag{21}$$

where θ_{zi} is the potential temperature at the inversion base and g is the acceleration of gravity. Here we use the lapse rate in the lower buffer layer instead of a single step jump because the capping inversion is not that strong so that a single temperature jump is not always clearly demarcated. We also use the mean wind speed at the top of the ABL because measurements of wind shear from the airplane and the Visalia sounder are too noisy to be a reliable gauge of the shearing rate of the winds aloft.

Because the convective velocity scale (Equation 14) represents the forcing from the surface heat flux, the non-dimensional entrainment velocity (w_e/w_*) should depend on other factors that influence entrainment. The results of a comparison between the six EPA flight determinations of scaled entrainment velocity and the inverse of the bulk Richardson number (Figure 34) shows this to be a remarkable confirmation of theory with a resultant correlation coefficient, r^2, of about 0.75. This finding supports our physical understanding of the controls on ABL entrainment to be the surface heat flux, stability of the overlying (buffer) layer, and the wind shear at the ABL top as quantified here by measurements of the mean wind in the vicinity of z_i. The strong correlation also bolsters confidence in our estimates of SJV entrainment rates.

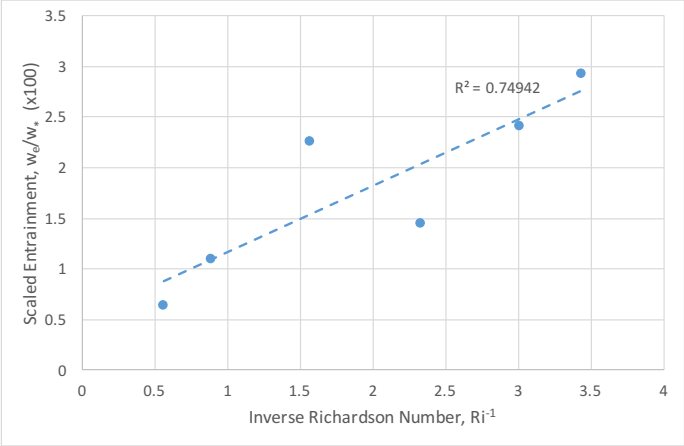

Figure 34. Non-dimensional entrainment velocity as a function of inverse bulk Richardson number for the six EPA flights.

Noting that the scaled entrainment during the July EPA flights were, on average, larger than those in the August flights (three leftmost points in Figure 34), and this appears to be most influenced by the stronger (more northerly, data not shown) winds in the 800-1500 m layer, we look to the synoptic patterns for both 3-day periods. Looking at the North American Regional Reanalysis (NARR) data set for the different flight intervals, a difference is observed. Namely, at the end of July the 850 mb geopotential heights have a stronger zonal gradient (driving a more northerly geostrophic flow) which is associated with higher surface temperatures (~7-8 K, not shown) in the Southern Sierras and Nevada. The warmer surface near the southern CA/NV border creates a thermal low pressure region that drives northerly winds on its western flank, and this can, in principle, accentuate entrainment in the SSJV.

Daytime and Diurnal Ozone Budget

From the careful budgeting of Equation (1) using the EPA flight data (Table 8), we found the average ozone photochemical production rate to be 6.3 ppb/hr (± 3.3), which can be compared to rates found in the far SSJV between Bakersfield and Arvin between 4.1 and 14.2 ppb/hr (average of 8.3 ppb/hr) during the summers of 2013/2014 [*Trousdell et al.*, 2016]. *L I Kleinman et al.* [2002] estimated ozone production rates using an observationally constrained chemical mechanism for five major U.S. metropolitan areas between 1995-2000 and found median values that ranged from 3.5, 4.3, 6.2 ppb/h (Phoenix, NYC, Nashville) to 11.3 ppb/h for Philadelphia & Houston. It is important to keep in mind when making any comparisons that the flights of this study specifically targeted periods of anticipated high ozone events, so the data is not necessarily representative of summer mean conditions. Nevertheless, the data from the SJV (Table 2 & [*Trousdell et al.*, 2016])

indicate that O_3 production generally increases as you progress southward in the SSJV. The VOC chemistry in the SJV is dependent on temperature: at moderate temperatures it is VOC-limited while at higher temperatures it is less so based on work by *Pusede et al.* [2014]. They also estimate ozone production rates based on a photochemical steady-state model constrained by observations from May/June of 2010 and found median values on

Table 8. Ozone budget terms for EPA and RLO midday flights.

Flight Date	dO_3/dt (ppb/hr)	Advection (ppb/hr)	Entrainment (ppb/hr)	Dry Dep. (ppb/hr)	O_3 Production (ppb/hr)	ABL [O_3] (ppb)	ABL [NO_x] (ppb)
EPA Flights							
7/27/16	1.2	-0.8	-1.2	-2.9	6.2	89.6	9.0
7/28/16	6.1	-2.3	0.8	-2.2	9.8	70.2	8.5
7/29/16	-0.8	0.2	-0.6	-2.3	1.9	76.9	9.6
8/4/16	0.9	-0.5	-0.9	-1.8	4.2	75.7	5.5
8/5/16	6.4	-1.6	-0.6	-1.8	10.4	59.9	7.8
8/6/16	3.0	0.0	-0.3	-1.9	5.2	70.9	7.8
EPA Averages	**2.8**	**-0.8**	**-0.5**	**-2.2**	**6.3**	**73.9**	**8.0**
RLO Flights							
Deployment 1							
9/10/15	11.8	1.4	-1.3	-2.0	13.6	90.7	15.3
9/11/15	6.9	0.5	-1.3	-2.6	10.2	79.7	10.5
9/12/15	3.2	0.1	-1.0	-2.1	6.1	69.8	9.6
Deployment 2							
6/2/16	0.8	-0.1	-2.6	-1.7	5.2	73.5	4.8
6/3/16	-4.4	-0.9	-3.1	-1.8	1.4	82.6	4.1
6/4/16	-2.7	0.7	-6.1	-2.3	5.1	85.1	6.2
Deployment 3							
7/24/16	-0.1	-0.1	-1.7	-2.1	3.9	76.9	7.3
7/25/16	1.4	1.7	-5.8	-2.2	7.7	82.5	9.0
7/26/16	-1.4	1.7	-8.0	-2.2	7.1	88.0	5.8
Deployment 4/5							
8/12/16	5.6	4.8	-5.0	-2.0	7.7	82.4	9.2
8/13/16	9.6	2.8	-1.2	-1.7	9.7	87.6	11.7
8/14/16	4.4	1.6	-4.7	-2.2	9.7	78.1	11.4
8/15/16	5.1	-1.2	-4.5	-1.7	12.4	68.6	8.2
8/16/16	-0.3	1.1	-2.6	-1.7	2.9	74.2	9.5
8/17/16	1.5	0.6	-3.2	-2.0	6.2	83.9	9.9
RLO Averages	**2.8**	**1.0**	**-3.5**	**-2.0**	**7.3**	**80.2**	**8.8**

the hottest days (average surface temperature of 309.5K) ranging from 15-26 ppb/hr. Their observations were made at the CalNex SJV Supersite about 30 min downwind of central Bakersfield and are therefore justifiably on the high side of the measurements presented here which are necessarily applicable to the broader regional average.

Another study which arose out of CalNex-SJV [*Brune et al.*, 2016] suggests that ozone production continues to increase with the NO concentration beyond about 1 ppb in contrast to the theoretical rollover expected as HNO_3 formation draws down the radical pool. Nonetheless, for their study high values of NO were mostly observed in the early morning

before the time frame of the *Pusede et al.* [2014] and this study (10-14 and 11-15 PST, respectively). *Trousdell et al.* [2016] argued that the ozone production in their study from 11 flights south of Bakersfield in 2013/2014 was NO_x-limited based on their estimates of the VOC:NO_x ratio derived from their airborne measurements of CH_4 as a VOC proxy, and the surface network observation of NO_x. We have included the ozone budget results from all 15 of the RLO midday flights (Table 8), although they are believed to be less precise than the EPA flights as discussed before, in order to see whether the O_3 production from this larger data set could be seen to vary with NO_x observed by the aircraft. Indeed, the observed ozone production rates are dependent on the NO_x levels (Figure 36), although the r^2 value declines to 0.25 when the high point from 10-Sep-2015 is eliminated. By contrast, when comparing the ozone production rates to ABL methane levels (above the tropospheric background) the positive linear correlation coefficient is 0.1.

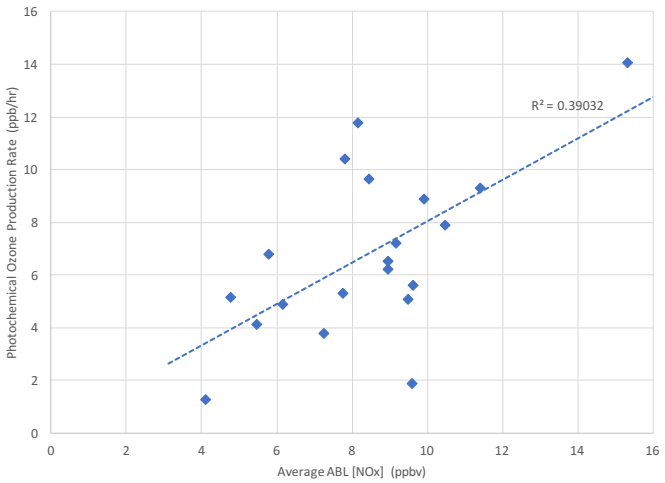

Figure 36. Ozone production rates as a function of observed NO_x levels for all EPA and RLO flights.

One of the most basic objectives of extensive air quality observations should be to track and map how it is changing over time. Given that prognostic equations for both SIP modeling and the scalar budgeting technique presented herein directly employ the different rate terms that sum to the total time derivative of a trace gas or aerosol species, we present the diurnal profiles of ozone time derivatives from Figure 2 along with the individual average terms from the EPA flights (Figure 35). The average photochemical production rate is extrapolated across the daylight hours by scaling the average observed value during the flight interval throughout the rest of the day based on the time series of $J(O^1D)$ from the NCAR Quick-TUV calculator (http://cprm.acom.ucar.edu/Models/TUV/Interactive_TUV/). Because the areas under the curves represent the total $[O_3]$ it can be seen that the contributions from photochemistry and mixing down from the RL (fumigation) are approximately comparable. Very similar 50-50 split contributions from these two terms have been presented by past studies [*L Kleinman et al.*, 1994; *C-H Lin*, 2008; *Neu et al.*, 1994]. However, it should be noted that the fumigation in this case is coming

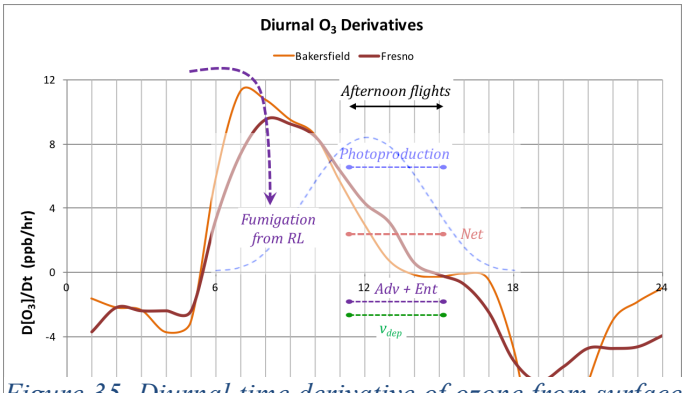

Figure 35. Diurnal time derivative of ozone from surface sites in Fresno & Bakersfield, and the average rates observed by the aircraft budgets from the EPA flights.

from the buffer layer which is the result of accumulated photochemical production from the region for the past few days.

Finally, we present an analysis of the average diurnal cycle of d[O_3]/dt (Figure 37) and d[O_x]/dt (Figure 38) for the SSJV based on our aircraft observations. Here we derive average trends across each ~2 hr RLO flight as well as the estimated trend *in between* flights, for a total of eight estimates each day. Data is binned into 3 altitude layers: the lower boundary layer 0-200 m (within the NBL when it is present), the upper boundary layer 200-600 m (mainly the RL when it is present), and the buffer layer 600-2000 m. It should be noted that there is significantly greater uncertainty in the estimates within flights than between flights. The near surface diurnal profile of the airborne ozone derivative appears very similar to that of Figure 2 & Figure 37 with a peak gain near 08:00-09:00 (during the fumigation from the RL), a zero-crossing (daily maximum in [O_3]) around 15:00, and a peak loss near 20:00. It is interesting to note that the near-surface loss of O_x

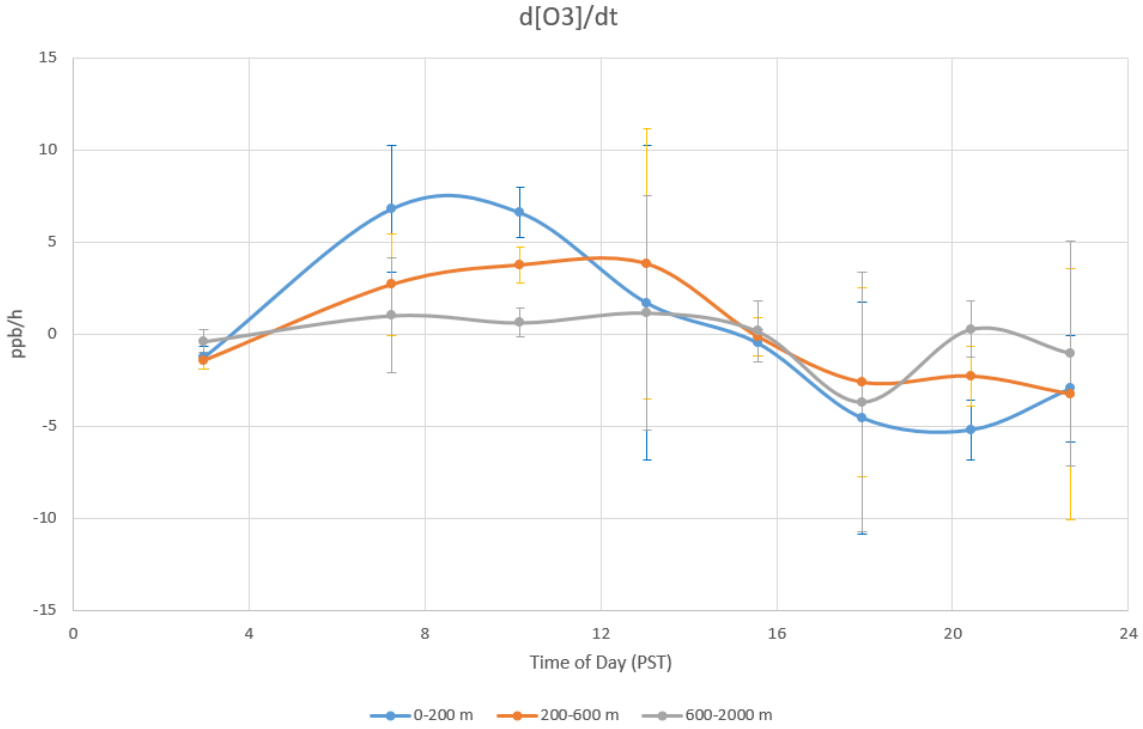

Figure 37. The average diurnal cycle of ozone derivative from all the RLO flight data.

throughout the evening is comparable to that of O_3 so the majority of the evening ozone loss is likely due to nitrate production and dry deposition and not simply titration with fresh emissions of NO. Moreover, there appears to be very little diurnal change in the buffer layer O_x meaning that its budget is dominated by small injections from the valley surface in the day and gradual advection of the stagnating flow. Of course, it is small imbalances in the cumulative daily value near the surface that lead to the rise and fall of synoptic ozone episodes, which could result from changes in the fumigation from the RL or changes in the loss from nitrate chemistry overnight.

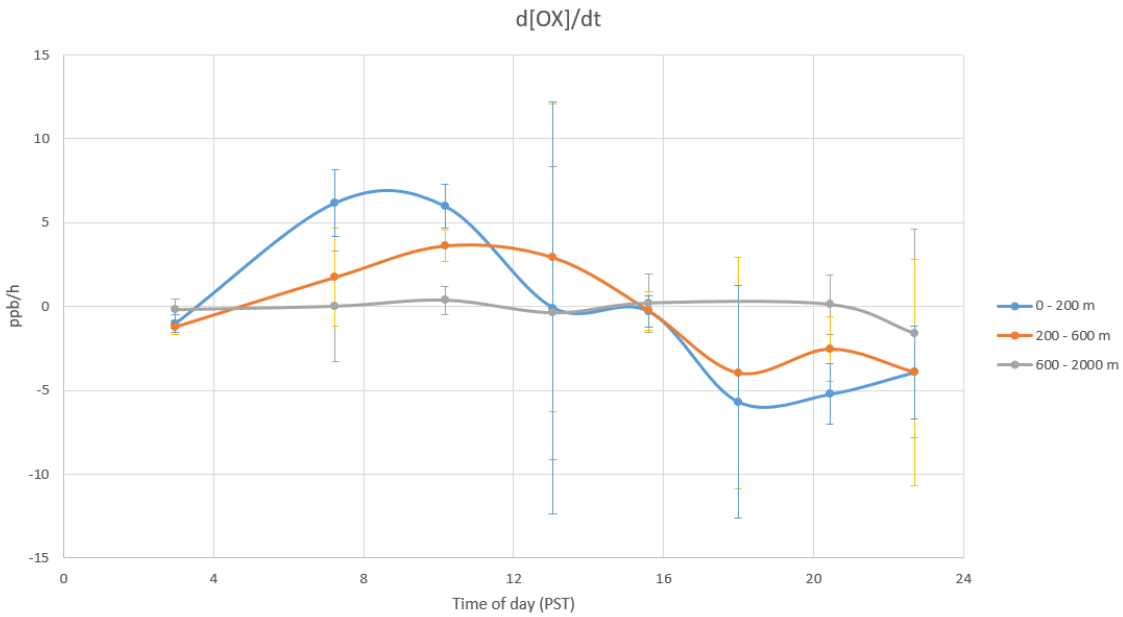

Figure 38. The average diurnal derivative of [O_x] from all RLO flight data.

CH_4 and NO_x Regional Emission Estimates

For a scalar such as methane undergoing extremely slow chemistry (with a photochemical lifetime of about a decade), the budget equation can be easily solved for the surface emission rate:

$$F_s = \left(U\frac{\partial CH_4}{\partial x} + \frac{\partial CH_4}{\partial t}\right) z_i + F_{ent} \qquad (22)$$

where the advection and temporal trend terms are observed directly by the aircraft, and F_{ent}, the entrainment flux, is estimated using the usual entrainment velocity parameterization based on the observed jump in CH_4 across the ABL top and the entrainment velocity derived from the ABL height budget. Regional methane emissions from the six EPA flights between Fresno and Visalia were estimated to range from 50 – 800 Gg yr^{-1} (360 ± 315 Gg yr^{-1}). The standard deviation of the mean reported here represents the spread in the measurements across the six different days of each campaign, not the estimated error in the measurements themselves. To obtain our in-situ emission estimate we multiplied our regionally averaged surface methane emissions by the approximate horizontal area encompassed by the average path within the ABL of all the flights. We estimate the horizontal area to be 5.2×10^9 m^2, however this too changes some from flight to flight as the flight path is not exactly the same in each case, and thus contributes to the spread in the total emission estimates. Table 9 summarizes the methane budget terms across each of the six EPA flights along with the average observed concentration and error estimate for the resultant emission rate. The error estimates come from a formal evaluation of possible uncertainty in the evaluation of each of the budget terms and added in quadrature to estimate the overall uncertainty of each emission estimate.

However, it should be noted that this estimated average error of 375 Gg yr^{-1} is believed to be a very conservative estimate and may not represent the true uncertainty in the measurement. Nevertheless, when averaging over the six flights this uncertainty may be considered to be reduced by a factor of 2.45 (=√6) to a value more like 150 Gg yr^{-1}, and consequently we are that much more confident in the six day average of this quantity.

In a recent work the Scanning Imaging Absorption Spectrometer for Atmospheric Chartography (SCIAMACHY) instrument from 2003–2009 the column-averaged CH_4 mole fractions over the U.S. are used to estimate surface emissions [*Kort et al.*, 2014]. Although the thrust of that study was the 'hot spot' observed over the four corners region of New Mexico, it is interesting to note that the second largest spot (their Fig. 1) that emerges in the satellite climatology is located in the southern San Joaquin Valley of California. Using the California Greenhouse Gas Emission Measurement (CALGEM; http://calgem.lbl.gov/prior_emission.html) inventory we estimated the emissions from each sector for the EPA flight region. The emission estimates have been scaled to the 2013 total CH_4 emission estimate for California of 41.1 Tg CO_2 equivalent provided by CARB. Inventory emissions from the equivalent flight region was found to total of 165 Gg yr^{-1}. Comparing these to the in-situ estimates of this study we find our estimates to be 2.2 times greater than the scaled CALGEM inventory. This top-down overestimate of the inventory is consistent with the ratio found by *Cui et al.* [2017] of 1.7, and by *Trousdell et al.* [2016] of 2.4–3.6, and the generalized result of *Miller et al.* [2013] who claim that emissions from ruminant sources are up twice as large as existing inventories. According to the breakdown in sources found in the CALGEM database we estimated the fractional coverage of each source type for the experimental domain. The sampling was found to bear over 85% livestock-dairies, another 5% non-dairy livestock facilities, and the balance coming from landfills, natural gas, and wastewater treatment.

Table 9. Summary of ABL methane budget terms and overall regional emission estimates from the EPA flights

Flight Date	$\partial[CH_4]/\partial t$ Storage	$-U(\partial[CH_4]/\partial x)$ Advection	$w_e\Delta[CH_4]/z_i$ Entrainment	F_0/z_i Emission	Regional Emissions	estimated error	Avg. ABL $[CH_4]$
	(ppbv/hr)	(ppbv/hr)	(ppbv/hr)	(ppbv/hr)	(tons/day)	(tons/day)	(ppbv)
7/27/16	-40.5	-3.4	-48.4	11.2	173	470	2170
7/28/16	-8.0	-6.9	-51.7	50.7	809	568	2027
7/29/16	-10.5	9.3	-22.7	2.9	49	269	2021
8/4/16	-5.7	-3.4	-35.0	32.7	687	466	2022
8/5/16	-5.3	0.0	-22.0	16.7	293	267	1993
8/6/16	-3.1	1.6	-11.8	7.1	133	209	1996
Averages	**-12.2**	**-0.5**	**-31.9**	**20.2**	**357**	**375**	**2038**
1σ	**14.1**	**5.6**	**15.9**	**18.2**	**315**	**145**	**66**

We can perform a similar analysis with NO_x, but because the photochemical oxidation is rapid in the afternoon (we estimate a lifetime of 4.6 hr during midday) the loss term needs to be estimated in the budget equation. The budget equation for ABL-averaged nitrogen oxides concentration, $[NO_x]$, can be written as

$$\frac{\partial[NO_x]}{\partial t} = \frac{F_0 + w_e\Delta[NO_x]}{z_i} - \frac{[NO_2]}{\tau_{NOx}} - U\frac{\partial[NO_x]}{\partial x} \qquad (23)$$

where the terms are (left to right): the observed time rate of change (sometimes referred to as 'storage'), net vertical mixing across the ABL boundaries (the difference between the surface flux, F_0, and the entrainment flux at z_i, the top of the ABL, which is parameterized as $-w_e\Delta[NO_x]$), photochemical loss (due to oxidation of NO_2 to nitric acid by OH, represented here as a chemical loss time scale, τ_{NOx}, based on an estimate of the average

midday [OH] ~ $6x10^6$ molec cm^{-3} from *Brune et al.* [2016]), and advection by the horizontal wind (the influence of the mean wind on the large scale horizontal gradient, here the *x* direction is rotated such that there is no mean crosswind component). Table 10 presents the individual budget terms of each of the EPA flights along with the resultant regional emission (in metric tons of NO_2 equivalent mass per day), estimated error, and the average [NO_x] observed in the ABL.

Table 10. Summary of ABL NO_x budget terms and overall regional emission estimates from the EPA flights

Flight Date	$\partial[NO_x]/\partial t$ Storage	$-U(\partial[NO_x]/\partial x)$ Advection	$w_e\Delta[NO_x]/z_i$ Entrainment	$-k[OH]\,[NO_2]$ Chem Loss	F_0/z_i Emission	τ_{NO2} lifetime	Regional Emissions	estimated error	Avg. ABL $[NO_x]$	1 σ
	(ppbv/hr)	(ppbv/hr)	(ppbv/hr)	(ppbv/hr)	(ppbv/hr)	(hr)	(tons/day)	(tons/day)	(ppbv)	(ppbv)
7/27/16	-0.29	0.01	-0.4	-1.5	1.6	4.7	249	181	9.0	3.5
7/28/16	-0.09	-0.09	-0.4	-1.4	1.8	4.7	280	160	8.5	2.6
7/29/16	-0.44	0.30	-0.2	-1.8	1.2	4.7	183	324	9.6	8.8
8/4/16	-0.73	0.04	-0.3	-1.1	0.6	4.6	108	130	5.5	1.6
8/5/16	-0.83	-0.01	-0.2	-1.5	0.9	4.4	139	161	7.8	2.9
8/6/16	-0.35	-0.02	-0.1	-1.3	1.1	4.5	181	148	7.8	2.4
Averages	**-0.46**	**0.04**	**-0.24**	**-1.43**	**1.18**	**4.60**	**190**	**184**	**8.0**	**3.6**
1σ	**0.28**	**0.13**	**0.12**	**0.23**	**0.44**	**0.13**	**65**	**71**	**1.4**	**2.6**

During the EPA flights larges spikes in the NO_x signal were encountered that are believed to be associated with interferences from the Soberanes fire plume effluent. The spikes did not substantially influence the average [NO_x] in the afternoon flights, but because they were only encountered in the late afternoon when the boundary layer grew deep enough to entrain the plume from aloft, their influence was particularly troublesome in estimates of the time trend in NO_x (the storage term). In four cases, simply removing the spikes from the ABL data set permitted a reasonable estimate, but on two flights we needed to resort to using data from the CARB monitoring network (https://www.arb.ca.gov/adam/hourly/hourly1.php). The trend established was the average of three station trends (from 11:00-16:00 PST) throughout the region (Fresno-Garland, Visalia-N. Church St., and Hanford-S. Irwin St.). The estimates from the surface network and aircraft were very comparable for the other four flights where both were measured (averages of -0.38 vs. -0.34 ppb/hr, respectively.) The photochemical lifetime of NO_x during midday (~4.6 hr) is much shorter than the advection time (~10 hr) of the fire plume even if the winds were blowing directly toward the study domain. Nevertheless, even though there was likely some influence of the fire on the regional NO_x levels, the contribution entered the ABL through entrainment, which in principle is accounted for in the budgeting method by changes in the average jump across the ABL top ($\Delta[NO_x]$).

Measured emissions for the flight region were 190 metric tons/day (± 65) averaged over the flights. Based on CARB's 2016 SIP - Standard Emission Tool (CEPAM: https://www.arb.ca.gov/app/emsinv/fcemssumcat/fcemssumcat2016.php) the total estimated emissions of NO_x, representative of the summer, is 101.3 metric tons/day for the three surrounding counties: Tulare, Fresno, and Kings in the SSJV. Although a direct comparison is difficult, the main challenges would only serve to make the discrepancy between these estimates even larger. First, the three counties total area (~31,000 km^2) is approximately six times as large as the flight area. Second, because over 85% of the NO_x sources in the CARB inventory are assumed to be mobile sources, the diurnal profile is

likely peaked around traffic rush hours which the flight hours (11:30-15:30 PDT) principally missed. This substantial discrepancy, backed by independent soil biogeochemical modeling, is hypothesized to stem from NO_x emissions from agricultural soils [*Almaraz et al.*, 2018].

The errors for each derivative term ($\partial/\partial t$, $\partial/\partial x$, and $\partial/\partial y$) are calculated from the multilinear regression algorithm and are presented as standard errors, which are residuals taken as the difference between the predicted values and the actual values normalized by the square root of the number of data points. The entrainment fluxes are comprised of the entrainment velocity and a scalar delta term (jump in the scalar between the ABL and FT.) The delta term error was assigned to be 1 ppb for NO_x and 50 ppb for methane estimated by eye from inspection of many vertical profiles. The entrainment velocity contains derivatives of ABL height, whose errors were previously mentioned, and a term from the WRF model (subsidence/ vertical velocity), which we have estimated as a conservative 0.5 cm s^{-1} as the model does not report error estimates, and the horizontal wind at ABL height assigned an error of 0.25 ms^{-1} based on the measurement capabilities of the aircraft instrument [*Conley et al.*, 2014]. The same error for horizontal winds near ABL height applies to the ABL horizontal winds used in calculating the advection terms. The NO_x equation has in it a chemical loss term with an error estimated from the reported uncertainty for termolecular reactions given by the JPL chemical kinetics compendium [*Burkholder*, 2015], and the error in averaged ABL [NO_2], employed in the chemical loss term, was taken as one standard deviation of all the ABL observations. Estimated emission terms are residual terms within the respective budget equations. Their errors are calculated by adding the error of all the other terms in the budget in quadrature. Finally, the regional area used to scale up the emission flux, which varied from flight to flight, was arbitrarily assigned an error of 20 percent.

SUMMARY & CONCLUSIONS

Overall, we believe this project has met its principal objective of providing detailed three-dimensional observations of trace gas concentrations during high ozone episodes in the southern San Joaquin Valley. This data set is unprecedented in repeatedly capturing the full diurnal cycle of these events in a specific region as they unfold, progress, and diminish. The airborne data has been provided to ARB in timely fashion and will hopefully be used by researchers to help validate air quality models. This effort was accomplished by systematically probing the lower atmosphere in the SSJV during the ozone season and making detailed measurements of the O_3, NO_x, CH_4, water vapor, winds, and temperature in the region between Fresno and Bakersfield, California.

There are a number of outcomes from the analysis of this data set that have been obtained, and there are likely many more possible, however it will require continued work. From the careful application of scalar budgeting to a wide variety of the airborne measurements we have been able to infer:

- The regional net photochemical production rates of ozone during the early afternoon when the diurnal pattern is near its peak, making the most significant contribution to the MDA8. These rates ranged from 1.3 – 13.6 ppb/hr, with an average of 7.0 ppb/hr. These observations are likely biased high because we purposely targeted periods of high ozone in the SSJV.
- The afternoon entrainment velocities that critically control the dilution rate (and thus, in part, air pollutant levels) in the ABL. The observed values ranged from 1.6 – 7.9 cm/s and appeared to be dependent on the surface heat (buoyancy) flux, and more surprisingly on the mean ABL wind speed.
- Overnight mixing rates in the form of eddy diffusivities that control the dynamical coupling of the residual layer to the surface and influence the amount of residual layer ozone that remains overnight. These diffusivities ranged from 0.6 – 2.8 m^2/s, and exhibited a square-root dependence on the in-situ observed turbulence intensity. These values are large relative to other estimates in the literature and probably reflect the stirring vigor of the nocturnal LLJ in the SJV.
- Provide preliminary estimates of area-wide emissions of CH_4 and NO_x (averages of 360 ± 130 Gg yr^{-1} and 190 ± 30 tons/day, respectively.)
- Daytime surface latent and sensible heat fluxes, the critical boundary conditions of any transport model, that power the mixing in the ABL.

Other observational products of the data set generated during this project include:

- The correlation between observed NO_x and photochemical O_3 production rates indicates that the SSJV is mostly NO_x–limited currently during episodes of near-threshold ozone.
- The spatial decorrelation scales (the mean characteristic distance of the 'patchiness') of the scalars were very different. The decorrelation lengths ranged from 90 km for temperature, 30 km for O_3, 18-20 km for CH_4 and H_2O, and 5.5 km for NO_x.

- The mean profiles generated from the repeated sampling of the confined region (Figure 19) demonstrate the vertical layering of air above the SSJV, and provides the foundation for a conceptual model to emerge about the time scales, mixing and stagnation of the lower atmosphere (Figure 24).

We feel that we have presented analyses of the data which better capture the sources and underlying causes of the ozone problem in this region which will aid modeling efforts, forecasting, attainment planning, and contribute to the overall knowledge and understanding of boundary layer meteorology.

RECOMMENDATIONS

Finally, we believe this project has demonstrated the capability of relatively low-cost airborne measurements for powerful atmospheric budgeting techniques and turbulence estimates, which will pave the way for future work to refine these methods and increase their practicality. The airborne budgeting techniques outlined in this project can provide a wide variety of scientific payoffs including regional emission rates, photochemical production rates, and turbulent mixing rates, all of which are critical foundations to accurate SIP modeling. Observations of these rates can provide unique insights into model fidelity (or infidelity) by opening up new dimensions in model validation: namely, comparing observed budget terms instead of just mean quantities. Air quality modelers often speak about being able to get the right answer for the wrong reasons, and probing the verity of the individual budget terms in any given scalar quantity can identify specific erroneous elements in the numerical model, and, most importantly, point to means of improving those elements.

Further, these airborne techniques can be used to make surveys of statewide emissions to help improve ARB's inventories. We feel that ARB should consider this relatively low-cost aircraft deployment strategy to map and improve the accuracy of their state emissions inventories. The UC Davis and Scientific Aviation, Inc. team has recently installed a fast wind probe on one of the aircraft permitting the direct measurements of fluxes via eddy covariance. Therefore, in addition to the budgeting technique outlined in this report, future airborne projects could include more accurate and spatially limited emissions estimates, providing a 'variable resolution' emission inventory mapper with built-in checks for consistency. We currently have the capability to do this with CO_2, CH_4, C_2H_6, and NO_x, but with appropriate instrument procurements it could also be done for N_2O, CO, and NH_3.

The work on oxidant lost during the night, made possible by this unique diurnal flight sequence deployed in this project, illustrates the critical importance of the chemical fate of the nitrate radical in the NBL. Because the stoichiometric loss of O_x per nitrate radical formed (R2) ranges from 0 (when sufficient NO is present to nullify the reaction back to $2NO_2$ (R6), which can happen with just a few hundred ppt of NO) to 3 (when hydrolysis of N_2O_5 on aerosols or fog droplets (R4) is fast), the propensity for it to build up overnight, and thus over a several day air pollution episode, is highly sensitive to the branching ratio of the nitrate loss. Moreover, because the nitrate production rate is likely similar throughout the NBL and RL, and we have shown here that variability in the strength of the nocturnal jet affects the delivery of RL reactants into the NBL where the sources of NO are, then this

dynamical feature can modulate the photochemical oxidant amounts that survive the night due to dry deposition and chemical losses. An extension of this project could be executed with separate measurements of NO (chemiluminescence) and NO_2 (spectroscopic) and the inclusion of whole air samplers for a full suite of VOCs could make important headway into understanding all of the principal elements controlling ozone (net production during the day and net loss overnight) in the SJV.

Finally, the resultant conceptual picture that has emerged from this project of the 3-layer atmospheric system above the Central Valley seems to implicate strong and variable effects of the mean vertical wind on the near surface air composition. Because of the presence of the mountains, the large and broad valley, and its proximity to the ocean, the atmospheric subsidence rates can be much larger (or order -10 cm/s) than synoptic norms considered by most meteorologists. We recommend probing this with our novel technique for measuring mean vertical winds by aircraft, a feat we believe we will be able to accomplish with our newly installed gust probe (and a higher tier of GPS accuracy.) The mean vertical wind is key to understanding the recirculation rates of the intermediate ("buffer") layer that lies above the daytime ABL in the valley in which air pollutants stagnate thereby weakening ABL dilution rates and aggravating air quality. Although such a project might be aimed at measuring an important meteorological parameter, judicious flight strategies could be developed to obtain emissions, chemical, and mixing rates as well.

LIST OF ABBREVIATIONS

ABL – Atmospheric Boundary Layer

AGL – Above Ground Level

BAAQMD – Bay Area Air Quality Management District

BBY – Bodega Bay call letters

BFL – Bakersfield airport call letters

BML – Bodega Marine Lab (operated by UC Davis)

CABOTS – The CAlifornia Baseline Ozone Transport Study

DLO – Delano airport call letters

FAT – Fresno airport call letters

FT – Free Troposphere

LLJ – Low level jet (a nocturnal phenomenon in the southern San Joaquin Valley that is a branch of the Fresno Eddy.)

MDA8 – Maximum Daily 8-Hour Average

MSL – Mean Sea Level

NAAQS – National Ambient Air Quality Standards

NBL – Nocturnal Boundary Layer

NOAA – National Oceanic and Atmospheric Administration

OLI – Operational Land Imager (satellite instrument onboard LandSat)

PDT – Pacific Daylight Time

PMT – Photomultiplier Tube

PST – Pacific Standard Time

RASS – Radio-Acoustic Sounding System

RL – Residual Layer

RLO – Residual Layer Ozone (shorthand for identifying this project)

SIP – State Implementation Plan

SJV – San Joaquin Valley

SSJV – Southern San Joaquin Valley

TKE – Turbulent Kinetic Energy

TLR – Tulare airport call letters

TOPAZ – Tunable Optical Profiler for Aerosols and Ozone (lidar)

VIS – Visalia airport call letters

VOC – Volatile Organic Compound

WRF – Weather Research and Forecasting model

w_e – Entrainment velocity

z_i – Height of the ABL (base of the capping inversion)

REFERENCES

Almaraz, M., E. Bai, C. Wang, J. Trousdell, S. Conley, I. Faloona, and B. Z. Houlton (2018), Agriculture is a major source of NOx pollution in California, *Sci. Adv.*, *4*(1), 8, doi:10.1126/sciadv.aao3477.

Aneja, V. P., R. Mathur, S. P. Arya, Y. X. Li, G. C. Murray, and T. L. Manuszak (2000), Coupling the vertical distribution of ozone in the atmospheric boundary layer, *Environ. Sci. Technol.*, *34*(11), 2324-2329, doi:10.1021/es990997+.

Angevine, W. M. (1997), Errors in mean vertical velocities measured by boundary layer wind profilers, *J. Atmos. Ocean. Technol.*, *14*(3), 565-569, doi:10.1175/1520-0426(1997)014<0565:EIMVVM>2.0.CO;2.

Atkinson, R., D. L. Baulch, R. A. Cox, J. N. Crowley, R. F. Hampson, R. G. Hynes, M. E. Jenkin, M. J. Rossi, J. Troe, and I. Subcommittee (2006), Evaluated kinetic and photochemical data for atmospheric chemistry: Volume II – gas phase reactions of organic species, *Atmos. Chem. Phys.*, *6*(11), 3625-4055, doi:10.5194/acp-6-3625-2006.

Augstein, E., H. Schmidt, and F. Ostapoff (1974), The vertical structure of the atmospheric planetary boundary layer in undisturbed trade winds over the Atlantic Ocean, *Bound.-Layer Meteor.*, *6*(1-2), 129-150.

Bao, J. W., S. A. Michelson, P. O. G. Persson, I. V. Djalalova, and J. M. Wilczak (2008), Observed and WRF-simulated low-level winds in a high-ozone episode during the Central California Ozone Study, *J. Appl. Meteorol. Climatol.*, *47*(9), 2372-2394, doi:10.1175/2008JAMC1822.1.

Bianco, L., I. V. Djalalova, C. W. King, and J. M. Wilczak (2011), Diurnal Evolution and Annual Variability of Boundary-Layer Height and Its Correlation to Other Meteorological Variables in California's Central Valley, *Bound.-Layer Meteor.*, *140*(3), 491-511, doi:10.1007/s10546-011-9622-4.

Blackadar, A. K. (1957), - Boundary Layer Wind Maxima and Their Significance for the Growth of Nocturnal Inversions, - *38*(- 5), - 290.

Brown, S. S., et al. (2006), Nocturnal odd-oxygen budget and its implications for ozone loss in the lower troposphere, *Geophys. Res. Lett.*, *33*(8), 5, doi:10.1029/2006gl025900.

Brown, S. S., H. Stark, T. B. Ryerson, E. J. Williams, D. K. Nicks, M. Trainer, F. C. Fehsenfeld, and A. R. Ravishankara (2003), Nitrogen oxides in the nocturnal boundary layer: Simultaneous in situ measurements of NO3, N2O5, NO2, NO, and O-3, *J. Geophys. Res.-Atmos.*, *108*(D9), 11, doi:10.1029/2002jd002917.

Brune, W. H., et al. (2016), Ozone production chemistry in the presence of urban plumes, *Faraday Discuss.*, *189*, 169-189, doi:10.1039/c5fd00204d.

Burkholder, J. B., S. P. Sander, J. Abbatt, J. R. Barker, R. E. Huie, C. E. Kolb, M. J. Kurylo, V. L. Orkin, D. M. Wilmouth, and P. H. Wine (2015), Chemical Kinetics and Photochemical Data for Use in Atmospheric Studies, Evaluation No. 18*Rep.*, Jet Propulsion Laboratory, Pasadena, CA.

Caughey, S. J., and S. G. Palmer (1979), SOME ASPECTS OF TURBULENCE STRUCTURE THROUGH THE DEPTH OF THE CONVECTIVE BOUNDARY-LAYER, *Q. J. R. Meteorol. Soc.*, *105*(446), 811-827, doi:10.1002/qj.49710544606.

Clayson, C. A., and L. Kantha (2008), On turbulence and mixing in the free atmosphere inferred from high-resolution soundings, *J. Atmos. Ocean. Technol.*, *25*(6), 833-852, doi:10.1175/2007jtecha992.1.

Conley, S. A., et al. (2011), A complete dynamical ozone budget measured in the tropical marine boundary layer during PASE, *J. Atmos. Chem.*, *68*(1), 55-70, doi:10.1007/s10874-011-9195-0.

Conley, S. A., I. C. Faloona, D. H. Lenschow, A. Karion, and C. Sweeney (2014), A Low-Cost System for Measuring Horizontal Winds from Single-Engine Aircraft, *J. Atmos. Ocean. Technol.*, *31*(6), 1312-1320, doi:10.1175/jtech-d-13-00143.1.

Cooper, O. R., et al. (2011), Measurement of western US baseline ozone from the surface to the tropopause and assessment of downwind impact regions, *J. Geophys. Res.-Atmos.*, *116*, doi:10.1029/2011JD016095.

Cox, P., Delao, A., and A. Kormaniczak (2013), The California Almanac of Emissions and Air Quality*Rep.*, 246 pp, California Air Resources Board.

Cui, Y. Y., et al. (2017), Top-down estimate of methane emissions in California using a mesoscale inverse modeling technique: The San Joaquin Valley, *J. Geophys. Res.-Atmos.*, *122*(6), 3686-3699, doi:10.1002/2016jd026398.

Faloona, I., S. A. Conley, B. Blomquist, A. D. Clarke, V. Kapustin, S. Howell, D. H. Lenschow, and A. R. Bandy (2009), Sulfur dioxide in the tropical marine boundary layer: dry deposition and heterogeneous oxidation observed during the Pacific Atmospheric Sulfur Experiment, *J. Atmos. Chem.*, *63*(1), 13-32, doi:10.1007/s10874-010-9155-0.

Fast, J. D., et al. (2012), Transport and mixing patterns over Central California during the carbonaceous aerosol and radiative effects study (CARES), *Atmos. Chem. Phys.*, *12*(4), 1759-1783, doi:10.5194/acp-12-1759-2012.

Fedorovich, E., and R. Conzemius (2008), Effects of wind shear on the atmospheric convective boundary layer structure and evolution, *Acta Geophysica*, *56*(1), 114-141, doi:10.2478/s11600-007-0040-4.

Gentner, D. R., et al. (2014), Emissions of organic carbon and methane from petroleum and dairy operations in California's San Joaquin Valley, *Atmos. Chem. Phys.*, *14*(10), 4955-4978, doi:10.5194/acp-14-4955-2014.

Henne, S., M. Furger, S. Nyeki, M. Steinbacher, B. Neininger, S. F. J. de Wekker, J. Dommen, N. Spichtinger, A. Stohl, and A. S. H. Prévôt (2004), Quantification of topographic venting of boundary layer air to the free troposphere, *Atmos. Chem. Phys.*, *4*(2), 497-509, doi:10.5194/acp-4-497-2004.

Hu, X. M., D. C. Doughty, K. J. Sanchez, E. Joseph, and J. D. Fuentes (2012), Ozone variability in the atmospheric boundary layer in Maryland and its implications for vertical transport model, *Atmos. Environ.*, *46*, 354-364, doi:10.1016/j.atmosenv.2011.09.054.

Hu, X. M., P. M. Klein, M. Xue, F. Q. Zhang, D. C. Doughty, R. Forkel, E. Joseph, and J. D. Fuentes (2013), Impact of the vertical mixing induced by low-level jets on boundary layer ozone concentration, *Atmos. Environ.*, *70*, 123-130, doi:10.1016/j.atmosenv.2012.12.046.

Jin, L., R. A. Harley, and N. J. Brown (2011), Ozone pollution regimes modeled for a summer season in California's San Joaquin Valley: A cluster analysis, *Atmos. Environ.*, *45*(27), 4707-4718, doi:10.1016/j.atmosenv.2011.04.064.

Karl, T., P. K. Misztal, H. H. Jonsson, S. Shertz, A. H. Goldstein, and A. B. Guenther (2013), Airborne Flux Measurements of BVOCs above Californian Oak Forests: Experimental Investigation of Surface and Entrainment Fluxes, OH Densities, and Damköhler Numbers, *J. Atmos. Sci.*, *70*(10), 3277-3287, doi:10.1175/jas-d-13-054.1.

Kleinman, L., et al. (1994), OZONE FORMATION AT A RURAL SITE IN THE SOUTHEASTERN UNITED-STATES, *J. Geophys. Res.-Atmos.*, *99*(D2), 3469-3482, doi:10.1029/93jd02991.

Kleinman, L. I., P. H. Daum, D. Imre, Y. N. Lee, L. J. Nunnermacker, S. R. Springston, J. Weinstein-Lloyd, and J. Rudolph (2002), Ozone production rate and hydrocarbon reactivity in 5 urban areas: A cause of high ozone concentration in Houston, *Geophys. Res. Lett.*, *29*(10), doi:10.1029/2001gl014569.

Kort, E. A., C. Frankenberg, K. R. Costigan, R. Lindenmaier, M. K. Dubey, and D. Wunch (2014), Four corners: The largest US methane anomaly viewed from space, *Geophys. Res. Lett.*, *41*(19), 6898-6903, doi:10.1002/2014gl061503.

Kuang, S., M. J. Newchurch, J. Burris, L. H. Wang, P. I. Buckley, S. Johnson, K. Knupp, G. Y. Huang, D. Phillips, and W. Cantrell (2011), Nocturnal ozone enhancement in the lower troposphere observed by lidar, *Atmos. Environ.*, *45*(33), 6078-6084, doi:10.1016/j.atmosenv.2011.07.038.

Langford, A. O., J. Brioude, O. R. Cooper, C. J. Senff, R. J. Alvarez, R. M. Hardesty, B. J. Johnson, and S. J. Oltmans (2012), Stratospheric influence on surface ozone in the Los Angeles area during late spring and early summer of 2010, *J. Geophys. Res.-Atmos.*, *117*, 17, doi:10.1029/2011jd016766.

Lenschow, D. H., P. B. Krummel, and S. T. Siems (1999), Measuring entrainment, divergence, and vorticity on the mesoscale from aircraft, *J. Atmos. Ocean. Technol.*, *16*(10), 1384-1400, doi:10.1175/1520-0426(1999)016<1384:MEDAVO>2.0.CO;2.

Lenschow, D. H., V. Savic-Jovcic, and B. Stevens (2007), Divergence and vorticity from aircraft air motion measurements, *J. Atmos. Ocean. Technol.*, *24*(12), 2062-2072, doi:10.1175/2007JTECHA940.1.

Lenschow, D. H., J. C. Wyngaard, and W. T. Pennell (1980), MEAN-FIELD AND 2ND-MOMENT BUDGETS IN A BAROCLINIC, CONVECTIVE BOUNDARY-LAYER, *J. Atmos. Sci.*, *37*(6), 1313-1326, doi:10.1175/1520-0469(1980)037<1313:Mfasmb>2.0.Co;2.

Leukauf, D., A. Gohm, and M. W. Rotach (2016), Quantifying horizontal and vertical tracer mass fluxes in an idealized valley during daytime, *Atmos. Chem. Phys.*, *16*(20), 13049-13066, doi:10.5194/acp-16-13049-2016.

Lin, C.-H. (2008), Impact of Downward-Mixing Ozone on Surface Ozone Accumulation in Southern Taiwan, *Journal of the Air & Waste Management Association*, *58*(4), 562-579, doi:10.3155/1047-3289.58.4.562.

Lin, Y. L., and I. C. Jao (1995), A NUMERICAL STUDY OF FLOW CIRCULATIONS IN THE CENTRAL VALLEY OF CALIFORNIA AND FORMATION MECHANISMS OF THE FRESNO EDDY, *Mon. Weather Rev.*, *123*(11), 3227-3239, doi:10.1175/1520-0493(1995)123<3227:Ansofc>2.0.Co;2.

Liu, G. P., D. W. Tarasick, V. E. Fioletov, C. E. Sioris, and Y. J. Rochon (2009), Ozone correlation lengths and measurement uncertainties from analysis of historical ozonesonde data in North America and Europe, *J. Geophys. Res.-Atmos.*, *114*, 12, doi:10.1029/2008jd010576.

Mahrt, L. (2010), Variability and Maintenance of Turbulence in the Very Stable Boundary Layer, *Bound.-Layer Meteor.*, *135*(1), 1-18, doi:10.1007/s10546-009-9463-6.

McKendry, I. G., D. G. Steyn, J. Lundgren, R. M. Hoff, W. Strapp, K. Anlauf, F. Froude, J. B. Martin, R. M. Banta, and L. D. Olivier (1997), Elevated ozone layers and vertical down-mixing over the Lower Fraser Valley, BC, *Atmos. Environ.*, *31*(14), 2135-2146, doi:10.1016/s1352-2310(96)00127-6.

Miller, S. M., et al. (2013), Anthropogenic emissions of methane in the United States, *Proceedings of the National Academy of Sciences*, *110*, 20018-20022.

Morris, G. A., B. Ford, B. Rappengluck, A. M. Thompson, A. Mefferd, F. Ngan, and B. Lefer (2010), An evaluation of the interaction of morning residual layer and afternoon mixed layer ozone in Houston using ozonesonde data, *Atmos. Environ.*, *44*(33), 4024-4034, doi:10.1016/j.atmosenv.2009.06.057.

Neu, U., T. Kunzle, and H. Wanner (1994), ON THE RELATION BETWEEN OZONE STORAGE IN THE RESIDUAL LAYER AND DAILY VARIATION IN NEAR-SURFACE OZONE CONCENTRATION - A CASE-STUDY, *Bound.-Layer Meteor.*, *69*(3), 221-247, doi:10.1007/bf00708857.

Padro, J. (1996), Summary of ozone dry deposition velocity measurements and model estimates over vineyard, cotton, grass and deciduous forest in summer, *Atmos. Environ.*, *30*(13), 2363-2369, doi:10.1016/1352-2310(95)00352-5.

Panofsky, H. A., H. Tennekes, D. H. Lenschow, and J. C. Wyngaard (1977), The characteristics of turbulent velocity components in the surface layer under convective conditions, *Bound.-Layer Meteor.*, *11*(3), 355-361.

Parrish, D. D., K. C. Aikin, S. J. Oltmans, B. J. Johnson, M. Ives, and C. Sweeny (2010), Impact of transported background ozone inflow on summertime air quality in a California ozone exceedance area, *Atmos. Chem. Phys.*, *10*(20), 10093-10109, doi:10.5194/acp-10-10093-2010.

Pio, C. A., M. S. Feliciano, A. T. Vermeulen, and E. C. Sousa (2000), Seasonal variability of ozone dry deposition under southern European climate conditions, in Portugal, *Atmos. Environ.*, *34*(2), 195-205, doi:10.1016/s1352-2310(99)00276-9.

Pusede, S. E., and R. C. Cohen (2012), On the observed response of ozone to NOx and VOC reactivity reductions in San Joaquin Valley California 1995-present, *Atmos. Chem. Phys.*, *12*(18), 8323-8339, doi:10.5194/acp-12-8323-2012.

Pusede, S. E., et al. (2014), On the temperature dependence of organic reactivity, nitrogen oxides, ozone production, and the impact of emission controls in San Joaquin Valley, California, *Atmos. Chem. Phys.*, *14*(7), 3373-3395, doi:10.5194/acp-14-3373-2014.

Rao, D. N., M. V. Ratnam, T. N. Rao, and S. V. B. Rao (2001), Seasonal variation of vertical eddy diffusivity in the troposphere, lower stratosphere and mesosphere over a tropical station, *Annales Geophysicae*, *19*(8), 975-984, doi:10.5194/angeo-19-975-2001.

Reuten, C., D. G. Steyn, and S. E. Allen (2007), Water tank studies of atmospheric boundary layer structure and air pollution transport in upslope flow systems, *J. Geophys. Res.-Atmos.*, *112*(D11), 17, doi:10.1029/2006jd008045.

Russell, L. M., D. H. Lenschow, K. K. Laursen, P. B. Krummel, S. T. Siems, A. R. Bandy, D. C. Thornton, and T. S. Bates (1998), Bidirectional mixing in an ACE 1 marine boundary layer overlain by a second turbulent layer, *J. Geophys. Res.-Atmos.*, *103*(D13), 16411-16432.

Salmond, J. A., and I. G. McKendry (2002), Secondary ozone maxima in a very stable nocturnal boundary layer: observations from the Lower Fraser Valley, BC, *Atmos. Environ.*, *36*(38), 5771-5782, doi:10.1016/s1352-2310(02)00698-2.

Stull, R. B. (1988), *An Introduction to Boundary Layer Meteorology*, Kluwer Academic Publishers.

Stutz, J., K. W. Wong, L. Lawrence, L. Ziemba, J. H. Flynn, B. Rappenglück, and B. Lefer (2010), Nocturnal NO3 radical chemistry in Houston, TX, *Atmos. Environ.*, *44*(33), 4099-4106, doi:https://doi.org/10.1016/j.atmosenv.2009.03.004.

Sullivan, P. P., C.-H. Moeng, B. Stevens, D. H. Lenschow, and S. D. Mayor (1998), Structure of the Entrainment Zone Capping the Convective Atmospheric Boundary Layer, *J. Atmos. Sci.*, *55*(19), 3042-3064, doi:10.1175/1520-0469(1998)055<3042:Sotezc>2.0.Co;2.

Sun, J., and Y. Wang (2008), Effect of the Entrainment Flux Ratio on the Relationship between Entrainment Rate and Convective Richardson Number, *Bound.-Layer Meteor.*, *126*(2), 237-247, doi:10.1007/s10546-007-9231-4.

Tennekes, H. (1973), MODEL FOR DYNAMICS OF INVERSION ABOVE A CONVECTIVE BOUNDARY-LAYER, *J. Atmos. Sci.*, *30*(4), 558-567, doi:10.1175/1520-0469(1973)030<0558:Amftdo>2.0.Co;2.

Trousdell, J. F., S. A. Conley, A. Post, and I. C. Faloona (2016), Observing entrainment mixing, photochemical ozone production, and regional methane emissions by aircraft using a simple mixed-layer framework, *Atmos. Chem. Phys.*, *16*(24), 15433-15450, doi:10.5194/acp-16-15433-2016.

Wilson, R. (2004), Turbulent diffusivity in the free atmosphere inferred from MST radar measurements: a review, *Annales Geophysicae*, *22*(11), 3869-3887, doi:10.5194/angeo-22-3869-2004.

Zaveri, R. A., et al. (2010), Overnight atmospheric transport and chemical processing of photochemically aged Houston urban and petrochemical industrial plume, *J. Geophys. Res.-Atmos.*, *115*, 19, doi:10.1029/2009jd013495.

Zhong, S. Y., C. D. Whiteman, and X. D. Bian (2004), Diurnal evolution of three-dimensional wind and temperature structure in California's Central Valley, *J. Appl. Meteorol.*, *43*(11), 1679-1699, doi:10.1175/JAM2154.1.

APPENDIX: CALIBRATIONS AND DATA CORRECTIONS

The airborne NO_x measurements were made with an EcoPhysics (model CLD-88) chemiluminescence instrument with stabilized PMT and reaction chamber temperatures and other operating parameters to ensure a steady calibration point and high reproducibility. A blue light LED photolytic converter (model 42i BLC2-395 manufactured by Air Quality Design, Inc.) was used to selectively convert NO_2 to NO for alternating measurements of NO_x (=NO+NO_2). Further, a 50 ml Teflon pre-reaction chamber was installed to run the chemiluminescence reaction to completion before the detection cell in order to keep track of any interferences or changes in the background signal, thereby increasing the confidence in the measurements and lowering the detection limit generally to less than 0.05 ppbv. The instrument was cycled through the three states of NO, NO_x, and background measurements every 20 seconds. Calibrations were performed by O_3 titration with a NIST traceable NO standard (Scott-Marrin, Inc.) certified to within 5%. Full calibrations were performed before and after the entire flight series, with zero and span checks run routinely before and after each flight. The aircraft used to conduct the experiment is operated by Scientific Aviation, Inc. (http://scientificaviation.com/overview/). The ozone instrument is a dual-beam absorption instrument made by 2B Technologies, Inc. (Model 205) and is calibrated quarterly using an ozone calibration source (Model 306). All calibrations of the ozone instrument over the course of this project exhibited offsets and slopes that are less than 1.5 ppb and within 4%, respectively.

The EcoPhysics chemiluminescence instrument was delivered after a Swiss factory calibration/certification on 5/28/2015. Later that summer, after integration onto the aircraft, CARB's Mobile Quality Assurance Lab conducted an audit on 7/21/2015 of the aircraft measurements of O_3, NO, NO_2, and temperature. Because we did not set up the lamp cycling software, lamp efficiency correction, and because there was an unexpected offset coming from the lamp, the NO2 measurement failed the audit. After several more days of "burn-off" and testing the NOx measurements were improved and a return audit of by CARB's Mobile Lab on 8/6/2015 was successful (ARB Audit #: 57997). In between deployments we performed our own calibrations of the NO_x system via ozone titration of a NIST-certified NO cylinder (typically ~ 100 ppbv) and zero-air dilution. A typical NO_x calibration from the lab in between deployments is shown in Figure 9, and another is shown below. The average slope of all the calibrations was found to be 1.005 (±0.026) and the average offset was 1.1 ppb (±0.4 ppb). Each deployment data set was corrected for the average coefficients of the calibrations performed before and after the deployment.

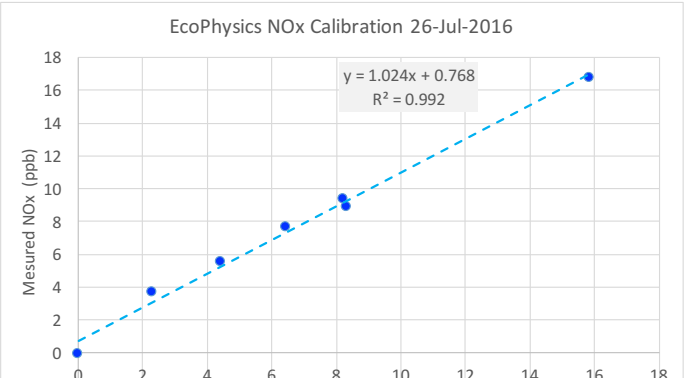

Figure 39. EcoPhysics NOx calibration from July 26, 2016.

Analysis of NO_x data from this field campaign revealed a disturbing trend of systematic

decay in the NO_2 signal for most flights. This trend was corrected in the final dataset submitted to the ARB. The following describes the laboratory testing that was done to characterize the decay and remove it.

On Friday 7 October 2016, the EcoPhysics instrument needed to be run for a few hours in order to establish a method for the instrument to communicate with the computer. This was successfully completed, and the instrument was shut off until the following Tuesday. Data was then logged for several hours with the lamp on, occasionally switching the lamp off for approximately 1 minute at a time to check the NO signal (experiment 1). This experiment was repeated Wednesday afternoon (experiment 2), with the final experiment running overnight Wednesday into Thursday with the lamp remaining on for the entire duration (experiment 3).

Results: The decay signal observed in the airplane was replicated in the lab for all experiments. With ambient air being measured, it is assumed that laboratory values of NO and NO_2 will remain fairly constant throughout the duration of each experiment, so the goal is to determine if the decay signal can be removed by the methods used to correct the airplane data. The exponential correction was applied with the following procedure:

1) With the beginning of the measurement mode (not initial power up) set as t=0, a time series is created for the species (c).
2) With t on the x-axis and log(c) on the y-axis, the linear regression (a*x+b) of the scatter plot is taken
3) A function of time is generated: $f(t) = e^{bat}$
4) (4) The corrected species time-series is generated as follows:

   $c'(t) = c(t) - f(t) + f(t_{max})$

   Where t_{max} is the endpoint of the experiment.

Additionally, for exploratory purposes, a 3rd order and 5th order polynomial are created. The following procedure is used:

1) With the beginning of the measurement mode (not initial power up) set as t=0, a time series is created for the species (c).
2) With t on the x-axis and c on the y-axis, both a 3rd (ax^3+bx^2+cx+d) and 5th (ax^5+bx^4+cx^3+dx^2+ex+f) order polynomial are generated.
3) A function of time is generated: $f(t) = at^3 + bt^2 + ct + d$ and $f(t) = at^5 + bt^4 + ct^3 + dt^2 + et + f$
4) The corrected species time-series is generated as follows:

   $c'(t) = c(t) - f(t) + f(t_{max})$

   Where t_{max} is the endpoint of the experiment.

The graphed results from each experiment are shown below:

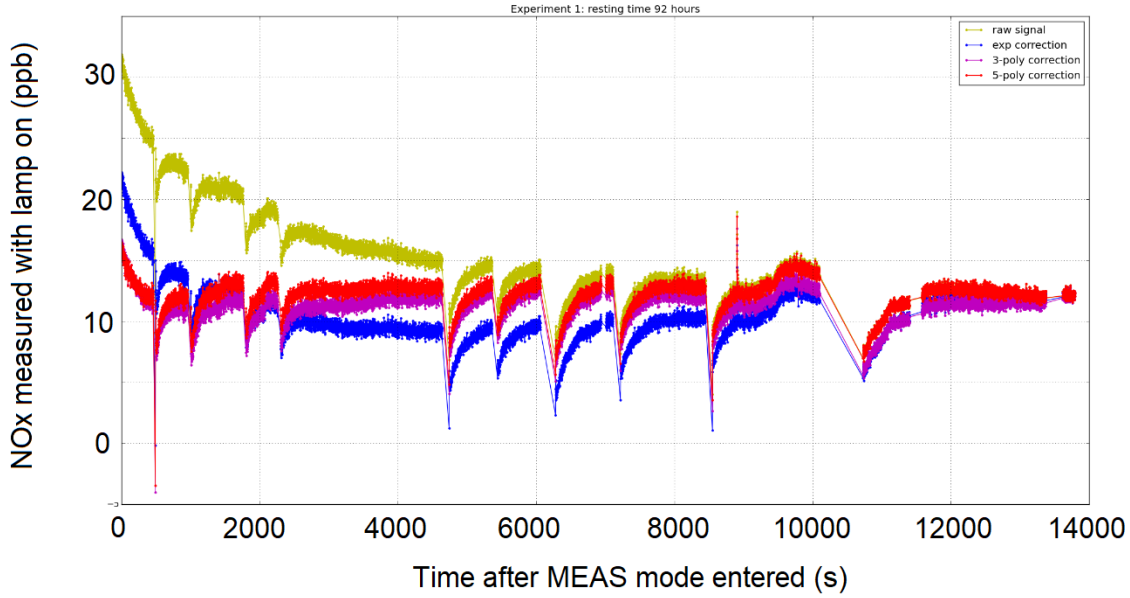

Figure 40. Results from NOx signal decay testing (Experiment 1)

First, it need be noted that in experiments 1 and 2, the dips in the signal are a result of the lamp switching from off to on (the NO signal is discussed separately below). It is clear that the exponential correction does not fully remove the decay signal and may also result in an underestimation of the true concentration for the bulk of the experiments. Using polynomials may allow the fitted curve to adjust for the shape of the decay, but using too high of an order may overcompensate and incorrectly smooth out a signal that is truly changing with differing NO_2 concentrations. While the signal is not fully removed in experiment 3, it should be noted that the duration of that experiment is far longer than any flight performed.

It is observed that the decay in NO signal is far more prominent for experiment 1 than experiment 2. It is hypothesized that after a longer instrument resting period, the adjustment period to display the true NO signal (after the lamp switching off) may be considerably longer. This is consistent with the observation that the NO signal decay was mainly observed on the first flights of some field campaigns. It is noted however, and possibly worrisome, that in experiment 1, one lamp-off period lasted about 10 minutes and it took about that long for the value to stabilize. This raises questions about the quality of NO measurements where a decaying NO signal is observed, and these concerns are reflected in the final dataset with appropriate quality flags.

On 20 October 2016, the instrument was turned on again. The lamp was kept on until 15 minutes after the start of measurement mode, then shut off. Data was collected over the next several hours, then the instrument was turned off. This experiment was done to look for a decaying NO signal (experiment 4).

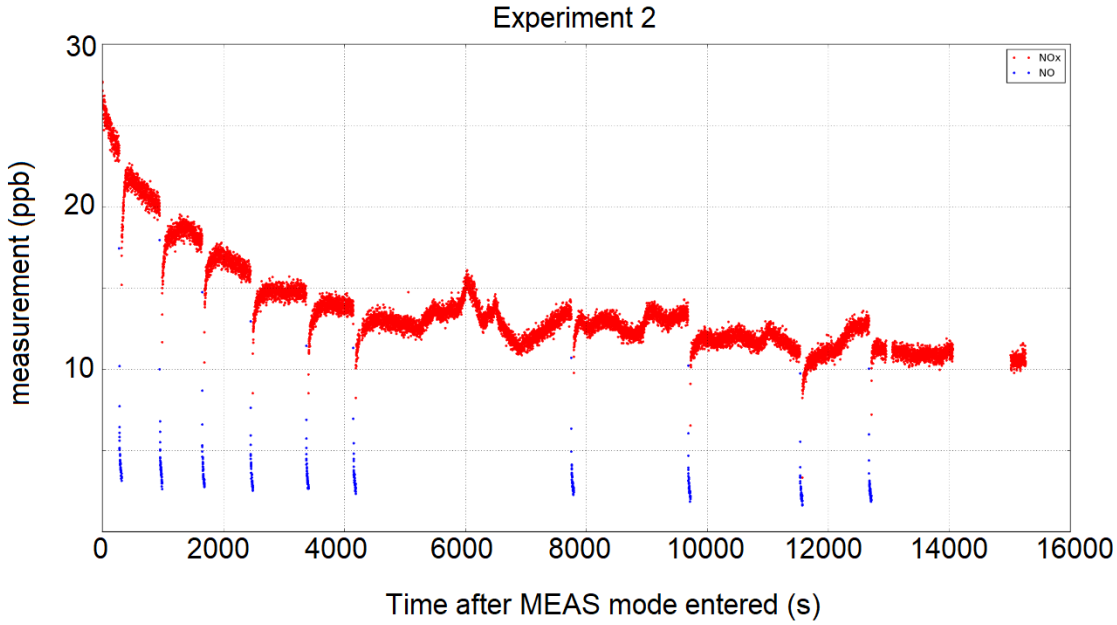

Figure 41. NO & NO_2 signals during experiment 2.

On 21 October, the instrument was turned on, and the lamp was switched on and off every 20 seconds for a 2 hour period to simulate the manner in which the converter is heated during flights (experiment 5). Afterwards, the lamp was kept on for 48 hours with data recording to monitor background NO_x levels in the lab. At this point, the lamp was turned off to collect long-term background NO levels, with data recording for another 40 hours.

Starting with the NO_x results, the method tested that appears to have the best results for the lab data is as follows:

1) With the beginning of the measurement mode (not initial power up) set as t=0, a time series is created for the species (c). The time axis is cut at t=13500 seconds for each experiment for purpose of consistency.
2) A median value, X, is obtained for c(t>3600).
3) With t on the x-axis and log(c-X) on the y-axis, the linear regression (m*x+b) of the scatter plot is taken (for all points of which c-X>0)
4) A function of time is generated: $f(t) = e^{bat}$
5) The corrected species time-series is generated as follows: $c'(t) = c(t) - f(t)$

Results:

Table 11. Results from experiments 1-3 and 5 of EcoPhysics exponential signal decay test.

Instrument Off	**X**	**m**	**b**
3.5 (experiment 3)	12.95	-0.000356	2.249700
19.5 (experiment 2)	12.58	-0.000341	1.906279
24 (experiment 5)	16.94	-0.000652	1.607392

It is first worth noting that the m and b values, unfortunately, do not appear to change predictably as a function of instrument-off time under a consistent method. However, while not explicitly shown, different values of X were explored for each experiment, and small changes to its value can have large effects on the quality of the correction (and thus corresponding m and b values). In some cases, the manual adjustment of X can result in a correction that appears (somewhat subjectively) better (such as a better removal of the initial high readings). The challenge was to find a consistent method for the generation of the X value such that the best overall correction is seen for the lab data (which should show only small fluctuations in time) that also appears to work well for the flight data. In flight data, recording is often started after the initial 500 seconds after measurement mode is entered. The method of setting to X be the median for all points with t>3600 appeared to work best overall for flight and lab data. This is shown for sample flight data below:

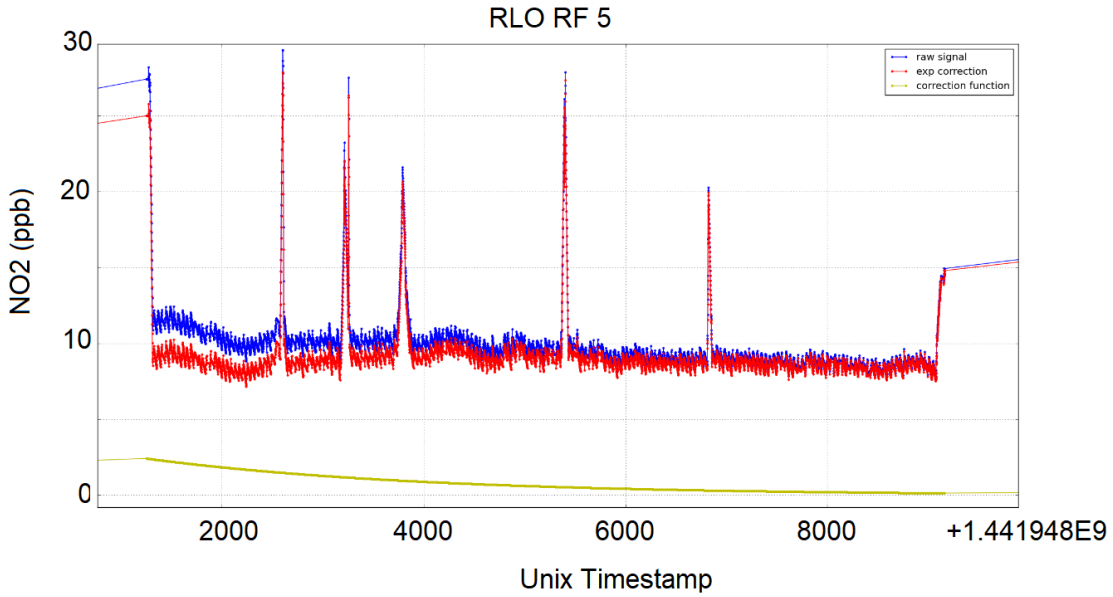

Figure 42. Sample correction to NOx signal for flight data.

For most flights, a correction series similar to what is seen in flight number 5 is obtained. However, occasionally when the decay factor is small, a small (near-zero) m value is obtained. To address this issue, we will add one additional step to the methodology, which will be to adjust each correction function such that the end of the curve reaches y=0. This is justifiable because the correction by the end of any flight should be near zero, assuming the instrument has been steadily running. In mathematical terms, the adjusted final step is:

$$c'(t) = c(t) - [f(t) - w]$$

Where w = f(t_{max})

NO correction:
A decay signal for NO similar to that of NO_X is seen for the lab experiments, reproduced below:

Table 12.Results from experiments 4-5 of EcoPhysics exponential signal decay test.

Instrument Off	**X**	**m**	**b**
24 Hours (experiment 5)	1.732	-0.000332	0.191581
168 Hours (experiment 4)	-0.25	-0.000452	-0.067438

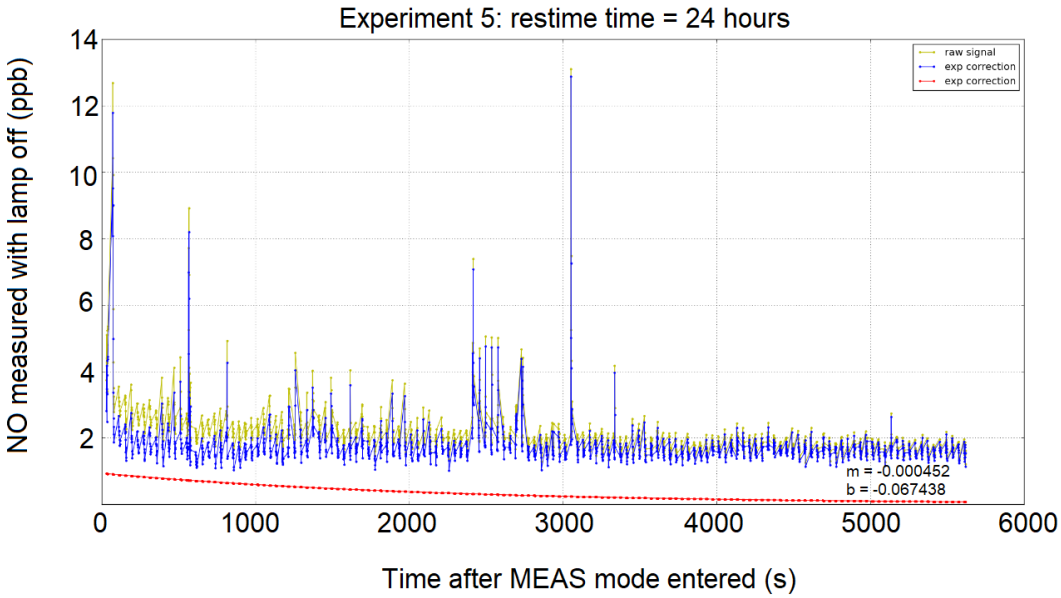

Figure 43. NO signal decay test.

Given that the decay signal is observed for the NO signal in this reproducible manner, even without any intermittent lamp-on time (as in experiment 4), it is justifiable to apply this correction where apparent in the flight data.

Conclusions: we have presented our methods for correcting NO and NO_2 flight data for this anomalous exponential decay of the signal. For data where the quality of the correction is questionable, it is appropriately reflected as such in the quality flag column.